The analysis of fluorescence fluctuations by means of the mean single-molecule rate (mSMR)

Von der Faktultät für Mathematik, Informatik und Naturwissenschaften der RWTH Aachen University zur Erlangung des akademischen Grades eines Doktors der Naturwissenschaften genehmigte Dissertation

vorgelegt von

Lorenz Tim Sparrenberg (M. Sc.)
aus
Aachen

Berichter: Univ.-Prof. Dr. rer. nat. Ulrich Schwaneberg
Univ.-Prof. Dr. rer. nat. Thomas Berlage

Tag der mündlichen Prüfung: 13.03.2023

Eidesstattliche Erkärung

Lorenz Tim Sparrenberg

erklärt hiermit, dass diese Dissertation und die darin dargelegten Inhalte die eigenen sind und selbstständig, als Ergebnis der eigenen originären Forschung, generiert wurden.

Hiermit erkläre ich an Eides statt

1. Diese Arbeit wurde vollständig oder größtenteils in der Phase als Doktorand dieser Fakultät und Universität angefertig;
2. Sofern irgendein Bestandteil dieser Dissertation zuvor für einen akademischen Ausschuss oder eine andere Qualifikation an dieser oder einer anderen Institution verwendet wurde, wurde dies klar angezeigt;
3. Wenn immer andere eigene- oder Veröffentlichungen Dritter herangezogen wurden, wurden diese klar benannt;
4. Wenn aus anderen eigenen- oder Veröffentlichungen Dritter zitiert wurde, wurde stets die Quelle hierfür angegeben. Diese Dissertation ist vollständig meine eigene Arbeit, mit der Ausnahme solcher Zitate;
5. Alle wesentlichen Quellen von Unterstützung wurden benannt;
6. Wenn immer ein Teil dieser Dissertation auf der Zusammenarbeit mit anderen basiert, wurde von mir klar gekennzeichnet, was von anderen und was von mir selbst erarbeitet wurde;
7. Ein Teil oder Teile dieser Arbeit wurden zuvor veröffentlich und zwar in:
    - Greiner, B; Sparrenberg, LT; Berwanger, K. Verfahren zur Bestimmung der Konzentration eines fluoreszierenden und/oder fluoreszenzmarkierten Analyten und Kalibrierverfahren zur Vorbereitung dieser Bestimmung. Patent EP 3 644 047 A1, 2018.
    - Sparrenberg, LT; Greiner, B; Mathis, HP. Bleaching correction for DNA measurements in highly diluted solutions using confocal microscopy, *PLoS ONE* 15(7):1-17, 2020. `https://doi.org/10.1371/journal.pone.0231918`
    - Sparrenberg, LT; Greiner, B; Mathis, HP. The Mean Single Molecule Rate (mSMR) in the Analysis of Fluorescence Fluctuations: Measurements on DNA Mixtures of Defined Composition. *Journal of Fluorescence* 31(6): 1883-1894, 2021. `https://doi.org/10.1007/s10895-021-02803-3`

Bonn, den 13.06.2022

Lorenz Tim Sparrenberg

"The deepest solace lies in understanding,
This ancient unseen stream,
A shudder before the beautiful"

Tuomas Holopainen

Zusammenfassung

Die Fluoreszenzfluktuationsspektroskopie (FFS) ist ein wichtiges Werkzeug für die Analyse biologischer Systeme auf Einzelmolekülebene. Über die Jahre wurden verschiedene Methoden entwickelt, die auf dem Prinzip der FFS beruhen. Sie lassen sich grob in zwei Kategorien einteilen. Methoden der ersten Kategorie untersuchen Fluktuationen in der Zeitdomäne und umfassen u.a. die bekannte Fluoreszenzkorrelationsspektroskopie (FCS) und ihre Varianten. Methoden der zweiten Kategorie analysieren Fluktuationen in der Amplitudendomäne, wozu z.B. das *photon counting histogram* (PCH) gehört. In dieser Arbeit wird eine neue Methode entwickelt, die Informationen aus beiden Domänen vereint, die *mean single-molecule rate* (mSMR). Sie basiert auf *Mandels Q-Parameter*, der aus den ersten beiden Kumulanten einer Fluoreszenzspur berechnet wird. Die Kumulanten können für beliebige Aggregationszeiten einer Fluoreszenzspur ausgedrückt werden, wodurch sich der Q-Parameter als zeitabhängige Größe ergibt. Durch eine Normierung zeigen die Q-Parameter für verschiedene Aggregationszeiten eine große Ähnlichkeit mit den Autokorrelationskurven der FCS-Analyse, was eine vergleichbare Interpretation der Daten ermöglicht. Durch die Definition der mSMR über Kumulanten, können aber auftretende Detektorartefakte korrigiert werden, was eine bessere Modellanpassung für die betroffenen Zeitskalen ermöglicht.
Um die mSMR als neue Methode für die FFS-Analyse zu etablieren, wird sie in dieser Arbeit systematisch untersucht. Zunächst werden simulierte Fluoreszenzspuren analysiert. Es zeigt sich, dass die mSMR die Simulationsparameter auch bei Vorliegen von Rauschen und Detektorartefakten exakt reproduzieren kann. Für die anschließende Analyse von Fluoreszenzspuren des Farbstoffs Alexa Fluor 488 kommt ein selbstgebauter konfokaler Plate Reader zum Einsatz. Dieser führt automatisch FFS-Messungen in einer 384-Well Mikrotiterplatte durch und erlaubt dadurch schnelle und wiederholbare Messungen. Bei der Analyse der Fluktuationen liefern die mSMR und die etablierte FCS vergleichbare Ergebnisse. Auf kurzen Zeitskalen erbringt die mSMR aber bei Messungen mit wenigen Photonenereignissen plausiblere Ergebnisse. Zum Schluss wird die mSMR für die Analyse von DNA-Mischungen mit definierter Fragmentlängenzusammensetzung verwendet und Kalibrierkurven erhoben. Basierend auf diesen Ergebnissen werden DNA-Sequenzierbibliotheken charakterisiert und die Massenkonzentration, die mittlere Fragmentlänge sowie die Molarität der Proben bestimmt. Dabei liefert die mSMR vergleichbare Ergebnisse wie das übliche mehrstufige Verfahren aus Fluoreszenzspektroskopie und Kapillargelelektrophorese.
Die vorliegende Arbeit zeigt, dass die mSMR eine sinnvolle Erweiterung der bisherigen FFS-Methoden darstellt. Insbesondere für Messungen mit wenigen Photonenereignissen stellt die mSMR eine robuste und zuverlässige Methode dar. Durch die Korrektur von Detektorartefakte kann die mSMR auch Fluktuationsereignisse auf sehr kurzen Zeitskalen auflösen und so genauere Analysen von photokinetischen Effekten ermöglichen.

Abstract

Fluorescence fluctuation spectroscopy (FFS) is an important tool for the analysis of biological systems at the single-molecule level. FFS methods can be roughly divided into two categories. Methods of the first category examine fluctuations in the time domain and include the well-known fluorescence correlation spectroscopy (FCS) and its variations. Methods of the other category analyze fluctuations in the amplitude domain and include the photon counting histogram and related methods. In this thesis, the *mean single-molecule rate* (mSMR) is introduced as a new method, which uses information from both the time and amplitude domain. The mSMR is based on *Mandel's Q parameter*, which can be calculated from the first two cumulants of a fluorescence trace. The cumulants can be expressed for arbitrary sampling times of a fluorescence trace, which yields the Q parameter as a sampling time-dependent quantity. By normalizing the Q parameter to its corresponding sampling time, data curves are obtained which show great similarities to the autocorrelation curves in FCS analysis and enable a comparable interpretation of the data. The model definition based on cumulants allows direct correction of common detector artefacts such as afterpulsing or dead time.
For evaluation, the mSMR is subjected to a series of systematic analyses. Firstly, it was applied to simulated fluorescence traces since the simulation enables precisely adjustable parameters. It was shown that the mSMR model accurately reproduces the input parameters of the simulation both in the absence and presence of noise and detector artefacts. Secondly, the mSMR was used to analyze fluorescence traces of the dye Alexa Fluor 488 recorded with a home-built confocal plate reader. Our reader automatically conducts FFS measurements in a microtiter plate, thus enabling easy and repeatable measurements with low hands-on time. A visual and statistical comparison between the mSMR and the established FCS showed that the mSMR provides generally comparable results to the FCS method. At low excitation powers and low concentrations, however, the mSMR provides more plausible results on short time scales. This is of particular importance for the analysis of photokinetic effects. Thirdly, to show the relevance of the mSMR for biological systems, measurements were performed on DNA mixtures of defined fragment length composition. Here, too, the mSMR retrieved precise results that are in line with theoretical expectations. Based on these findings, libraries for DNA sequencing were characterized and mass concentration, mean fragment length and molarity of the libraries were determined. In just one measurement, the mSMR could provide the same results as a commonly used multistep procedure consisting of fluorescence spectroscopy and capillary gel electrophoresis.
The mSMR represents a meaningful extension of previous FFS methods. The findings of this work suggest that especially for measurements with few photon events, e.g., at low excitation powers and concentrations, the mSMR is a robust and reliable method. In combination with the correction of detector artefacts, the mSMR can resolve fluctuation events on very short time scales and permits high-precision analyses of fluorescence fluctuations. This provides new insights into the analysis of photokinetic effects.

Data access

The data collected for this thesis are provided on the Fraunhofer publication server Fordatis (`https://fordatis.fraunhofer.de/`) under a Creative Commons license (CC BY 4.0). In addition to the measurement data, the Python scripts for data analysis and visualization as well as the compiled code of the Monte Carlo simulation engine are also stored there.

Access is via the following digital object identifier:
`http://dx.doi.org/10.24406/fordatis/187`

Contents

Zusammenfassung **VII**

Abstract **VIII**

Data access **IX**

List of Figures **XII**

List of Tables **XIV**

1 Introduction **1**
1.1 Subject of the thesis . . . 3

2 Theory **4**
2.1 Fluorescence . . . 4
2.2 Fluorescence fluctuation spectroscopy . . . 8
2.2.1 Concentration fluctuations in tiny volumes . . . 9
2.2.2 Confocal optics . . . 10
2.2.3 Non-gaussian observation volume . . . 12
2.2.4 Fluorescence saturation in FFS experiments . . . 13
2.2.5 Modelling diffusion . . . 14
2.2.6 Diffusion of nucleic acids . . . 16
2.3 Fluorescence correlation spectroscopy . . . 19
2.3.1 Diffusion model of FCS . . . 20
2.3.2 Photokinetic effects in FCS . . . 22
2.3.3 Error estimation in FCS experiments . . . 24
2.4 The mean single-molecule rate (mSMR) . . . 25
2.4.1 Derivation of the mSMR . . . 25
2.4.2 Photokinetic effects in the mSMR . . . 28
2.5 Noise sources in FFS experiments . . . 29
2.5.1 Detector artefacts . . . 29
2.5.2 Other noise sources in FFS experiments . . . 31

3 Methods and instrumentation **33**
3.1 Monte Carlo simulation . . . 33
3.2 The confocal plate reader . . . 35
3.2.1 Instrumentation . . . 35
3.2.2 Autofocus and well offset . . . 37
3.2.3 Influence of temperature . . . 38
3.3 Data processing . . . 39
3.3.1 Calculating the autocorrelation for FCS . . . 39
3.3.2 Calculating the mSMR . . . 40
3.3.3 Correction of detector artefacts and background noise . . . 41

3.3.4 Correction of uncorrelated background noise in FFS experiments . . 43
3.4 Data fitting 45

4 The mSMR on simulated fluorescence fluctuations 49
4.1 Experimental procedure 49
4.2 Evaluation of the simulation engine using FCS 51
4.3 mSMR on simulated fluorescence traces 54
4.4 Consideration of measurement artefacts 56
4.4.1 Afterpulsing 56
4.4.2 Detector dead time 57
4.4.3 Background noise 58
4.5 Discussion 60

5 The mSMR in real measurements 63
5.1 Experimental procedure 63
5.2 Evaluation and calibration of the confocal plate reader 64
5.3 The mSMR under real measurement conditions 67
5.3.1 Detector artefacts 67
5.3.2 Visual comparison of FCS and mSMR 69
5.3.3 Statistical comparison of FCS and mSMR 73
5.4 Discussion 75

6 The characterization of nucleic acid mixtures using the mSMR 78
6.1 Experimental procedure 79
6.2 mSMR in the analysis of nucleic acid mixtures 80
6.2.1 Characterization of defined DNA mixtures 80
6.2.2 Photokinetic effects in the analysis of DNA mixtures 83
6.2.3 Photobleaching in the analysis of DNA mixtures 85
6.2.4 Characterization of natural DNA mixtures 87
6.3 Discussion 91

7 Conclusion 94
7.1 Outlook 95

8 Abbreviations 96

9 Bibliography 97

10 Appendix 108
10.1 Generalization of the FCS calculation to higher orders 108
10.2 Additional information to the mSMR model 110
10.3 Supplementary information on afterpulsing in Monte Carlo simulations . . 111
10.4 Statistical measures from the comparison of FCS and mSMR 112

List of Figures

2.1 Simplified Jabłoński diagram showing fluorescence and phosphorescence of a fluorophore . . . 4
2.2 Alexa Fluor 488 spectrum . . . 5
2.3 Fluorescence rates of Alexa Fluor 488 and Fluorescein for increasing excitation intensities . . . 8
2.4 Visualization of concentration fluctuations in femtoliter volumes. . . . 9
2.5 Schematic of the fluorescence fluctuation measurement principle . . . 10
2.6 Excitation profile of a laser in a confocal setup . . . 11
2.7 Normalized molecular detection efficiency (MDE) . . . 13
2.8 Influence of fluorescence saturation on the molecular detection efficiency . . 14
2.9 Random walk of diffusing particles along an axis starting at the origin . . . 16
2.10 Comparison of three models to describe the diffusion of DNA . . . 18
2.11 The autocorrelation reveals hidden information in fluorecence fluctuations . 20
2.12 The FCS model for varying parameters . . . 22
2.13 Visualization of the triplet model in FCS analysis . . . 23
2.14 The mSMR model for varying parameters . . . 28
2.15 Fluorescence emission spectrum of Alexa Fluor 488 and Raman scattering of water . . . 31

3.1 The working principle of the Monte Carlo simulation . . . 34
3.2 Schematic of the confocal plate reader for the automated measurement in a microtiter plate . . . 35
3.3 Rear and front view of the home-built confocal plate reader . . . 36
3.4 The influence of the offset on the measurement results . . . 38
3.5 The influence of background noise on the mean particle number and the single-molecule brightness rate . . . 44
3.6 The fitting of FCS and mSMR curves via non-linear regression . . . 47

4.1 FCS results from simulated fluorescence traces . . . 52
4.2 mSMR results from simulated fluorescence traces . . . 54
4.3 The influence of afterpulsing on mSMR and FCS curves . . . 57
4.4 The influence of detector dead time on mSMR and FCS curves . . . 58
4.5 The influence of background noise on mSMR and FCS curves . . . 59

5.1 Evaluation and calibration of the confocal plate reader using measurements on Alexa Fluor 488 dilution series . . . 65
5.2 Stepwise correction of the mSMR data . . . 68
5.3 The mSMR on real measurement data . . . 69
5.4 The triplet effect in real measurements . . . 72
5.5 Statistical comparison of the FCS and mSMR models . . . 74

6.1 mSMR analyses on DNA solutions of defined fragment length . . . 81

6.2 The relation of measured particle number to theoretical particle number in DNA solutions 82
6.3 The isomerization effect in the mSMR analysis of DNA measurements . . . 84
6.4 Triplet and isomerisation effects in the mSMR analysis of DNA measurements 85
6.5 Photobleaching in DNA dilution series 86
6.6 Characterization of four sequencing libraries using the mSMR method . . . 90

10.1 Visual comparison of equation 10.13, 10.14 and 10.15 in the mSMR model 110
10.2 The influence of afterpulsing on mSMR and FCS curves with a temporal resolution of 1×10^{-7} s 111

List of Tables

2.1 Photokinetic parameters of Fluorescein (FITC) and Alexa Fluor 488 7

4.1 General simulation parameters for the Monte Carlo experiments 50
4.2 Results of the fit of the FCS model to the FCS curves of the simulated fluorescence traces 53
4.3 Results of the fit of the mSMR model to the mSMR curves of the simulated fluorescence traces 55

5.1 Measurement parameters of Alexa Fluor 488 studies 64
5.2 Calibration results 67
5.3 Computation times of the FCS and mSMR analyses 75

6.1 Measurement parameters of DNA mixure studies 79
6.2 Input parameters for the semiflexible diffusion model of dsDNA 82

10.1 Measures of the statistical comparison of FCS and mSMR, part 1 112
10.2 Measures of the statistical comparison of FCS and mSMR, part 2 113

1 Introduction

Studying molecules at the single-molecule level is essential for understanding biological systems and emanates a great fascination. Natural systems are generally heterogeneous. However, since conventional evaluation methods do not work at the single-molecule level, ensemble averaging occurs. Hidden heterogeneities can thus not be detected. The heterogeneity can be spatial resulting from the interaction of the molecule with its environment. Or it can be temporal originating from internal states and the transitions among them [1, p. 8077]. Single-molecule detection (SMD) allows the elucidation of these processes and leads to a deeper insight into natural systems.
Because of its high sensitivity and excellent signal-to-noise ratio, fluorescence is a good candidate for single-molecule detection [2, p. 757]. Although single-molecule detection in condensed matter has been demonstrated with other systems such as in helium-cooled solids [3] or using trapped atoms [4, 5], these methods have no relevance for the analysis of biological systems [2, p. 757] and are therefore not discussed here. The beginning of single-molecule detection in solution was marked by the work of Rotman in 1961. He indirectly detected single-molecule events by measuring the fluorescent reaction product of single enzymes in tiny droplets [6]. Over a decade later, Hirschfeld succeeded in detecting single molecules of labeled poly(ethyleneimine) bound to γ-globulin. The poly(ethyleneimine) was labeled with 80-100 fluorescein molecules [7, 8]. The possibility to measure not only large aggregates but single molecules in solution came within reach in the early 1980s [9, 10] and was achieved in 1990 by detecting single rhodamine 6G molecules in a flow [11].
Today, there is a variety of fluorescence-based methods for single-molecule detection, which aim to reveal spatial structures and temporal dynamics of biological systems. However, the acquisition of structures and dynamics requires opposing, often mutually exclusive optimization strategies [12, p. 2]. Super-resolution microscopy belongs to the first group and seeks spatial structure information beyond the diffraction limit. In classical light microscopy, the diffraction limit prevents the resolution of two points closer than about 200 nm to each other. The so-called *Abbe's diffraction limit*, i.e., the ability to separate two neighboring points, is given by the wavelength λ of the incident light and the numerical aperture NA of the used objective lens:

$$R = \frac{\lambda}{2\,NA}. \tag{1.1}$$

Selected methods for bypassing the diffraction limit are briefly outlined below. For their principal ideas and experiments to achieve super-resolution microscopy, the Nobel Prize was awarded in 2014 to Betzig, Hell and Moerner [13]. In stimulated emission depletion (STED), a laser beam is focused into the specimen for excitation. With a short delay, a second ring-shaped excitation pulse suppresses fluorescence in the outer regions of the focus so that spontaneous fluorescence light is emitted only from a central region smaller than the diffraction-limited excitation focus. Two- or three-dimensional images are generated by applying this process stepwise to cover the whole sample [14, 15].

Other methods to enable spatial resolutions below the diffraction limit use stochastic approaches. The methods are based on the temporal separation of the emitted photons from the excited fluorophores by repeatedly stochastically switching the fluorophores between an activated and deactivated state during image acquisition. The stochastic blinking of non-overlapping point spread functions (PSF) formed by the diffraction limit allows the localization of individual fluorophores via a Gaussian fitting of the PSF. By repeating this process thousands of times, the fluorophore localizations can be deduced from the acquired frames and a high-resolution image is obtained [16, p. 4]. Methods using this approach are among others photoactivated localization microscopy (PALM) [17, 18], ground state depletion (GSD) [19], stochastic optical reconstruction microscopy (STORM) [20], direct STORM (dSTORM) [21], MINFLUX [22] or DNA-based point accumulation for imaging in nanoscale topography (DNA-PAINT) [23].
In contrast to the previous imaging techniques, methods based on the principle of fluorescence fluctuation spectroscopy (FFS) (see section 2.2) have proven useful for resolving temporal dynamics and photokinetic properties. The general strategy for FFS is to focus a laser on a tiny volume, select appropriate filters to block scattered light, and work with highly diluted fluorophores. Because stochastic concentration fluctuations occur in such a setup due to fluorescence molecules entering and leaving the tiny detection volume, there are also fluctuations in the detected fluorescence intensity, hence the name FFS. The fluctuation-based methods can be divided into two categories [24, p. 1883]. The first category includes methods that analyze fluctuations in the time domain and includes the widespread fluorescence correlation spectroscopy (FCS) (see section 2.3) first described by Magde, Elson and Webb [25, 26]. By introducing confocal optics (see section 2.2.2), the the signal-to-noise ratio has been substantially enhanced, pushing the detection limit to the single-molecule level [27, 28]. Important variants of the FCS are, among others, higher order FCS (HOFCS) [29, 30, 31], fluorescence cross-correlation spectroscopy (FCCS) [32, 33] or fluorescence lifetime spectroscopy (FLCS) [34, 35]. In the second category are methods that analyze fluctuations in the amplitude domain. These comprise, besides others, the photon-counting histogram (PCH) [36], the fluorescence-intensity distribution analysis (FIDA) [37] or the fluorescence cumulant analysis (FCA) [38]. The extension of the latter two methods to arbitrary sampling times has yielded the fluorescence intensity multi distribution analysis (FIMDA) [39] and time integrated fluorescence cumulant analysis (TIFCA) [40]. All these methods except FCCS can be deployed using a single excitation source and a single detection channel. The recently published correlated photon-counting histogram (cPCH) tries to generalize the FFS methods in one unified theory [41]. It can be shown that some of the previously described methods such as FCS, PCH, FCA, FIMDA and TIFCA can be derived from the cPCH theory [41, p. 9-11]. However, the cPCH itself requires two excitation sources and two detection channels.
In this thesis, an extension of the fluorescence cumulant analysis is presented that considers information from both the time and amplitude domain. We call this model the *mean single-molecule rate* (mSMR) [24]. The central quantity of the model is *Mandel's Q parameter*, which can be represented by the first two cumulants of a distribution. As shown by the work on FIMDA and TIFCA, the cumulants of a fluorescence trace can be defined for arbitrary sampling times [39, 38, 40], which allows the Q parameter to be expressed as a sampling time-dependent quantity. By normalizing the Q parameter to the sampling time, we obtain an expression that permits a comparable evaluation to the established FCS [24, p. 1883]. The mSMR can be extended with additional terms to describe photokinetic effects. Furthermore, the representation via cumulants allows a

direct correction of detector artefacts on the level of the cumulants [24, p. 1885-1886]. Since the mSMR works with a single excitation source in continuous wave mode and a single detection channel, it can be implemented in standard confocal setups.

1.1 Subject of the thesis

The overall aim of this work is to make fluorescence fluctuation experiments available to a broader scientific community. To achieve this, two objectives will be addressed. First, a home-built confocal plate reader is introduced (see section 3.2) and used to automatically record fluorescence fluctuation data. Thus, the reliability and single-molecule sensitivity of the system will be evaluated. Second, a new method to analyze of fluorescence fluctuation traces will be presented, the mean single-molecule rate (mSMR). It is subjected to a detailed review in a three-step process.

- The analysis of the mSMR by means of simulated fluorescence traces (see chapter 4).
- The comparison of the mSMR to the established FCS using a well-described dye system (see chapter 5).
- Measurements in a more complex biological system and analysis of the fluorescence traces using the mSMR (see chapter 6).

These systematic analyses should demonstrate the suitability of the methods, both on the instrument side and on the analysis side, thus establishing the mean single-molecule rate as an alternative framework for evaluating fluorescence fluctuations at the single-molecule level.

2 Theory

After a brief introduction to single-molecule detection and the work's objectives, the theory chapter provides the necessary background knowledge for a deeper understanding of the topic. It starts with a brief introduction to fluorescence, also noting quantum mechanical phenomena that lead to saturation effects and dye blinking. Then, the principles of fluorescence fluctuation spectroscopy (FFS) are presented, including both diffusion as the cause of the fluctuations and the confocal optics required for detection. This provides the basis to understand the theory behind fluorescence correlation spectroscopy (FCS) and its common extensions to describe the photokinetic effects of triplet state transitions and isomerization. Subsequently, the *mean single-molecule rate* (mSMR) model is introduced, which forms the core of this thesis. The mSMR bases on the first two sampling time-dependent cumulants of a distribution and is extended to the photokinetic effects of triplet state transition and isomerization. The chapter finishes with a brief review of typical noise sources in FFS experiments.

2.1 Fluorescence

Fluorescence is the spontaneous emission of light by a molecule after it has absorbed energy in form of light. Fluorescence can be explained using a *Jabłoński diagram* (see figure 2.1). An incident photon is absorbed by a fluorophore. The energy of the photon

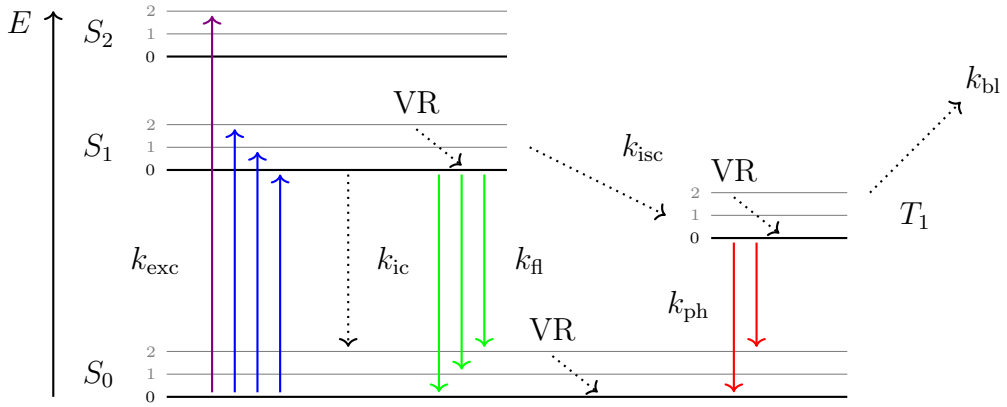

Figure 2.1: Simplified Jabłoński diagram showing fluorescence and phosphorescence of a fluorophore. Reproduced and modified from [2, p. 5].

depends on its frequency ν or respectively its wavelength λ and is given by

$$E = \nu\hbar = \frac{\hbar c}{\lambda}, \tag{2.1}$$

with $\hbar$ as *Planck constant* ($6.626 \times 10^{-34}\,\mathrm{J\,s}$) and c as speed of light ($2.998 \times 10^{8}\,\mathrm{m\,s^{-1}}$). Due to the absorbed energy, an electron is lifted from the ground singlet state S_0 to an energetically higher state S_1, and less frequently to even higher states such as S_2. Normally,

a vibrational relaxation (VR) from higher vibration levels to the ground vibration levels ($n = 0$) takes place directly after excitation, then the electron returns from the ground vibration level $n = 0$ of the higher state back to the ground state S_0 while radiating the excess energy as a photon (*Kasha rule*). Due to heat dissipation, the emitted fluorescence photon has a lower energy than the previously absorbed photon. This is reflected by a redshift of the fluorescence spectrum, denoted as *Stokes shift*. Figure 2.2 shows a typical absorption-emission spectrum of a fluorescent dye (here Alexa Fluor 488). The shift of the

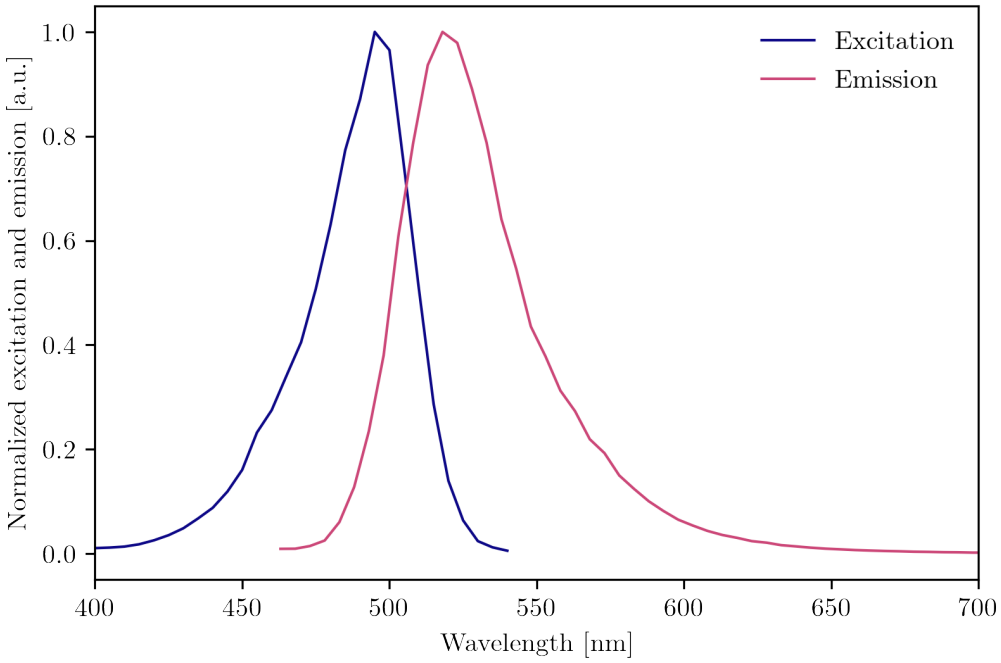

Figure 2.2: Normalized absorption and emission spectra of an Alexa Fluor 488 measurement in water. The excitation maximum is at 495 nm and the emission maximum at 519 nm.

emission spectrum towards longer wavelengths is clearly visible (Stokes-Shift). Another typical property of fluorescence spectra is the reflection of the two spectra along an imaginary line (*mirror image rule*), which results from the *Franck-Condon principle* stating that vibronic transitions are more likely to happen with strongly overlapping vibrational wave functions. The fluorescence lifetime τ_{fl} of a fluorophore is usually in the range of a few nanoseconds and depends on both its properties and the environment. An important measure for the fluorescence capability of a fluorophore is the fluorescence quantum yield θ_{fl}. It is defined by the ratio of excited molecules N_{fl} emitting fluorescence photons to the total number of excited molecules N_{exc}.

$$\theta_{\mathrm{fl}} = \frac{N_{\mathrm{fl}}}{N_{\mathrm{exc}}} \tag{2.2}$$

In addition to fluorescence, a spin reversal can occur which transfers the electron into an overlapping triplet state (intersystem crossing). The triplet state is meta-stable. A return to the S_0 state can only occur via a quantum mechanically "forbidden" spin reversal. This process is also accompanied by the emission of a photon (phosphorescence). A typical lifetime of the triplet state τ_{ph} is usually in the range of several milliseconds. Since an excited fluorophore in the long-lived triplet state cannot undergo further fluorescence cycles, continuous excitation repeatedly leads to phases in which no fluorescence can

occur. This behavior is known as fluorescence blinking.
Apart from the photon emitting pathways of fluorescence and phosphorescence, transitions can also occur without emitting a photon. The reversible case is called internal conversion (IC), where during the transition to the ground state the energy release occurs as heat. Because of the large energy difference between S_1 and S_0, this transition is unlikely. In the irreversible case of photobleaching, the fluorophore is destroyed after excitation, thereby losing its ability to emit photons [42, p. 2588]. Photobleaching is a dye-specific property and is characterized by the average number of excitation-emission cycles a fluorophor passes through until it is bleached [43, p. 830-831], which is referred to as quantum efficiency of photobleaching [43, p. 831]:

$$\theta_{\mathrm{bl}} = \frac{\text{number of bleached molecules}}{\text{number of absorbed photons}}. \tag{2.3}$$

The probability of photobleaching is directly dependent on the duration of irradiation, since an increasing number of excitation cycles also raises the fluorophore's chance to bleach [44, p. 91][45, p. 2651]. Photobleaching occurs either in the excited singlet or triplet state. Since the triplet state has a much longer lifetime ($\tau_{\mathrm{fl}} \ll \tau_{\mathrm{ph}}$), it is considered the main cause of photobleaching [43, p. 831]. The kinetics of photobleaching for freely diffusing fluorophores in solution follow an exponential decay [42, p. 2588]. The extent of photobleaching depends on different conditions, such as the excitation power, the photochemical properties of the fluorophore [45, p. 2656] or the oxygen content in the solvent [42, p. 2594-2595]. Oxygen seems to play an ambivalent role in photobleaching. Since oxygen is a strong triplet state quencher, it should minimize triplet state-associated photobleaching. Conversely, reactive singlet oxygen also appears to be a principal reactant in dye depletion [43, p. 831].

A three-level system describes the fluorescence process more precisely. As in the description of fluorescence on the Jabłoński diagram, the individual photokinetic processes occur on very different time scales. If the decay processes occur much faster than the fluorescence process, the process can be significantly simplified. With the occupation numbers N_0, N_1 and N_2 of the energy states S_0, S_1 and T_1, we can formulate a differential equation system [46, p. 5-7]:

$$\frac{\mathrm{d}}{\mathrm{d}t}\begin{pmatrix} N_0(t) \\ N_1(t) \\ N_2(t) \end{pmatrix} = \begin{pmatrix} -k_{\mathrm{exc}} & k_{\mathrm{fl}} & k_{\mathrm{ph}} \\ k_{\mathrm{exc}} & -(k_{\mathrm{fl}} + k_{\mathrm{isc}}) & 0 \\ 0 & k_{\mathrm{isc}} & -k_{\mathrm{ph}} \end{pmatrix} \begin{pmatrix} N_0(t) \\ N_1(t) \\ N_2(t) \end{pmatrix}. \tag{2.4}$$

The stationary solution of the above system is:

$$\begin{pmatrix} N_0 \\ N_1 \\ N_2 \end{pmatrix} = \begin{pmatrix} k_{\mathrm{fl}} + k_{\mathrm{isc}} \\ k_{\mathrm{exc}} \\ k_{\mathrm{exc}} \frac{k_{\mathrm{isc}}}{k_{\mathrm{ph}}} \end{pmatrix} \frac{N}{k_{\mathrm{fl}} + k_{\mathrm{isc}} + k_{\mathrm{exc}}(1 + \frac{k_{\mathrm{isc}}}{k_{\mathrm{ph}}})}. \tag{2.5}$$

N_j/N is the fractional population of level j and N is given by $N = \sum N_j$. In single photon excitation with a continuous laser, a linear approximation for the excitation rate holds for small excitation intensities [43, p. 830]:

$$k_{\mathrm{exc}} = \sigma_{\mathrm{a}}\, I_{\mathrm{exc}}. \tag{2.6}$$

with σ_{a} being the absorption cross-section (cm^2) and I_{exc} being the intensity of the excitation light (photons/cm^2 s). Instead of the absorption cross-section, the molar attenuation

coefficient ϵ also known as molar extinction coefficient is often given in literature. The molar attenuation coefficient indicates how strongly a chemical substance attenuates at a given wavelength. It is usually given in the unit $\mathrm{mol}^{-1}\mathrm{cm}^{-1}$. The attenuation coefficient and the absorption cross-section are related via the *Avogadro constant* N_A as follows [2, p. 59]:

$$\sigma_\mathrm{a} = \frac{\ln(10)\,10^3\,\epsilon}{N_\mathrm{A}} \approx 3.8235 \times 10^{-21}\,\epsilon. \tag{2.7}$$

If considering the mean fluorescence rate of a single molecule to be proportional to the fluorescence rate k_fl and the fraction of excited population N_1/N from equation 2.5, the fluorescence rate is given by the following expression [46, p. 7]:

$$F = \frac{C\,k_\mathrm{fl}}{1+Q}\frac{I_\mathrm{exc}/I_\mathrm{s}}{1+I_\mathrm{exc}/I_\mathrm{s}}, \tag{2.8}$$

The parameter C combines all properties of the detection system such as concentration of the dye solution and transmission losses through the measurement optics or the detector. The parameter Q is given by

$$Q = R\frac{\tau_\mathrm{ph}}{\tau_\mathrm{fl}}, \tag{2.9}$$

with $R = k_\mathrm{isc}/(k_\mathrm{fl}+k_\mathrm{isc})$ as the triplet crossing yield. The fluorescence lifetime is $\tau_\mathrm{fl} = (k_\mathrm{fl}+k_\mathrm{isc}+k_\mathrm{bl})^{-1} \approx k_\mathrm{fl}^{-1}$ [47, p. 29], and the phosphorescence lifetime is $\tau_\mathrm{ph} = k_\mathrm{ph}^{-1}$. The saturation intensity is given by [46, p. 7]

$$I_\mathrm{s} = \frac{h\nu}{\sigma_\mathrm{a}}\left(\frac{k_\mathrm{fl}+k_\mathrm{isc}}{1+\frac{k_\mathrm{isc}}{k_\mathrm{ph}}}\right). \tag{2.10}$$

If a molecule is excited with the saturation intensity, the absorption rate is exactly equal to the rate at which the molecule returns to the ground state [47, p. 32]. Fluorescence saturation is caused by an increasing number of fluorophores in the excited state, depleting molecules in the ground state S_0. While it is nearly impossible to achieve pure singlet saturation in experiments due to the very short lifetime of the excited S_1 state, the longevity of the triplet state T_1 means that a significant saturation effect can be observed even at low excitation powers. Figure 2.3 shows fluorescence rates of two commonly used fluorescent dyes Alexa Fluor 488 and Fluorescein as obtained from equation 2.8 for parameters from the literature (2.1).

Table 2.1: Photokinetic parameters of Fluorescein (FITC) and Alexa Fluor 488.

Parameter	Fluorescein	Alexa Fluor 488
Quantum yield q	0.95 [2, p. 54]	0.92 [48, p. 39]
Molar attenuation coefficient ϵ [$\mathrm{mol}^{-1}\mathrm{cm}^{-1}$]	77 000 [48, p. 68+72]	73 000 [48, p. 38-39]
Cross-section σ_a [cm^2] (using equation 2.7)	2.94×10^{-16}	2.79×10^{-16}
Fluorescence lifetime τ_fl [ns]	3.8 [48, p. 68+72]	4.1 [48, p. 38-39]
Phosphorescence rate k_ph [$\mu\mathrm{s}^{-1}$]	0.45 [49, p. 615]	0.25 [50, p. 66-67]
Intersystem crossing rate k_isc [$\mu\mathrm{s}^{-1}$]	5.0 [49, p. 615]	0.234 [50, p. 66-67]

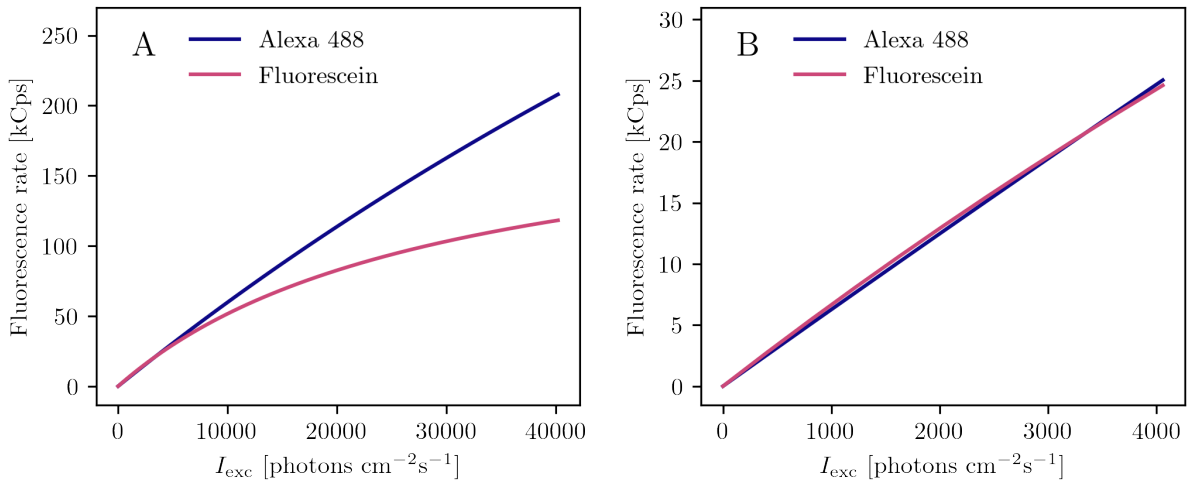

Figure 2.3: Fluorescence rates of Alexa Fluor 488 and Fluorescein for increasing excitation intensities. Equation 2.8 is modeled with the parameters from table 2.1 for an excitation wavelength of 488 nm. The bulk parameter C is set to $C = 0.01$. **A** Fluorescence rates are modelled up to an excitation intensity of 40 000 photons cm^{-2}s^{-1}. **B** A close-up view of the linear functional range at excitation intensities up to 4000 photons cm^{-2}s^{-1}.

In subplot A, the theoretical curve of the Alexa Fluor 488 dye lies considerably above the theoretical curve of the Fluorescein dye (FITC). Both dyes have almost the same fluorescence properties, but the Fluorescein dye shows a distinct triplet state, which causes the observed differences. At very low excitation rates, the difference between the dyes disappears and the graphs show the shape of a straight line (see subplot B). In experiments, the aim is therefore to find a compromise between negligible fluorescence saturation and the best signal-to-noise ratio [50, p. 13-14].

2.2 Fluorescence fluctuation spectroscopy

Fluorescence fluctuation spectroscopy (FFS) is an important technique for studying biomolecules in solution [24, p. 1883]. The basic principle is that fluorescent or fluorescently labeled molecules are excited by a laser. The laser is focused on a tiny volume. Molecules that travel through this volume are excited and emit photons. Due to the stochastic nature of the diffusive motion of the particles, fluorescence fluctuations occur in the signal. A fraction of the emitted photons is captured by a sensitive detector unit. A selection of FFS methods is briefly presented in the introduction 1.
First, the basic characterization of FFS setups is given, starting with a description of concentration fluctuations in small volumes and confocal optics, needed for the realization of FFS experiments. Then, non-ideal conditions are discussed and how they affect the models. In a further step, the diffusive transport of matter is described as a stochastic process introducing the concept of a random walk to model this phenomenon. Also, the special case of diffusing polymers such as nucleic acids is considered. Finally, two methods to analyze fluctuations are presented, the fluorescence correlation spectroscopy (FCS) and our newly developed *mean single-molecule rate* (mSMR).

2.2.1 Concentration fluctuations in tiny volumes

The basic principle of fluorescence fluctuation spectroscopy is the occurrence of concentration fluctuations in tiny observation volumes (~µm^3). Generally, the concentration C of a substance in a volume is given by the total number of particles N_{total} per total volume V_{total}.

$$C = \frac{N_{\text{total}}}{V_{\text{total}}} \tag{2.11}$$

In practice, the concentration is determined by averaging the measured particles in a volume. This approximation applies to systems that are in equilibrium and contain a sufficiently large number of molecules in the observation volume. In very small observation volumes, these requirements are no longer met and spatial, statistical fluctuations in the number of particles occur. Figure 2.4 illustrates this observation. The black dots are randomly distributed over a surface. If this area is now gradually divided into small subfields, differences in the number of dots in the individual subfields become more and more apparent.

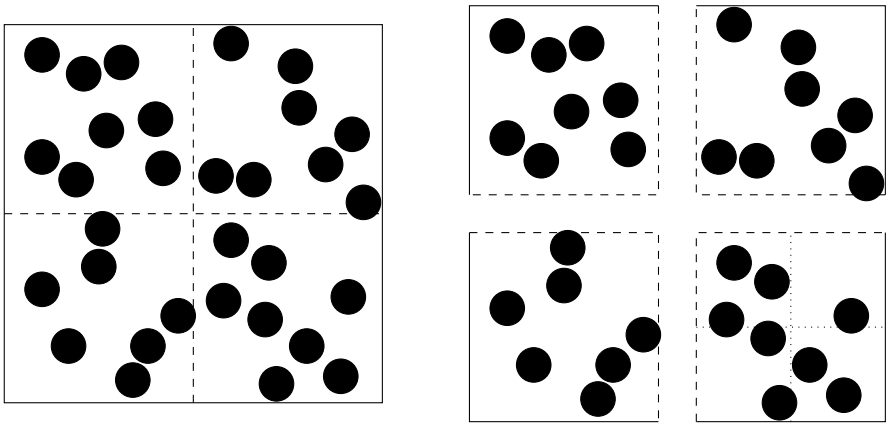

Figure 2.4: Visualization of concentration fluctuations in femtoliter volumes. While the number of particles is relatively uniformly distributed in a large volume, significant fluctuations are evident in smaller sub volumes. Reproduced from [51, p. 5].

The number of particles N in a sub volume V follows a *Poisson distribution* with $\mu = N$, which corresponds to the mean number of particles [52, p. 44][36, p. 557].

$$P(n|\mu = N) = \frac{N^n}{n!}e^{-N} \tag{2.12}$$

An essential characteristic of *Poisson distributions* is that the expected value corresponds to the variance: $N = \text{Var}(N)$. Therefore, the relative fluctuation of the particles in a volume is given by the following relationship [53, p. 10]:

$$\frac{\Delta N}{N} = \frac{\sqrt{\text{Var}(N)}}{N} = \frac{1}{\sqrt{N}}. \tag{2.13}$$

It becomes clear that the relative fluctuations decrease for increasing particle numbers. For fluorescence fluctuation experiments, therefore, optical setups are required that guarantee sufficiently small observation volumes to be able to observe sufficiently large fluctuations. Confocal optics meet the requirements for this type of measurement.

2.2.2 Confocal optics

The methods of fluorescence fluctuation spectroscopy require optical setups that can detect single photon events. This is achieved by co-localizing the excitation and observation volume of a focused laser spot and thus minimizing the detection volume [51, p. 16]. Due to diffusion, fluorophores are entering and leaving the focus. Excited by the laser light, they start to emit photons that are shifted towards longer wavelengths due to the Stokes shift. A dichroic mirror separates the excitation light of the laser from the emitted light of the molecules. Essential for confocal optics is a pinhole which cuts off fluorescence events from all planes except the focal plane and thus reduces background noise. A highly sensitive photodiode collects the incoming photon events. Figure 2.5 shows the schematic setup

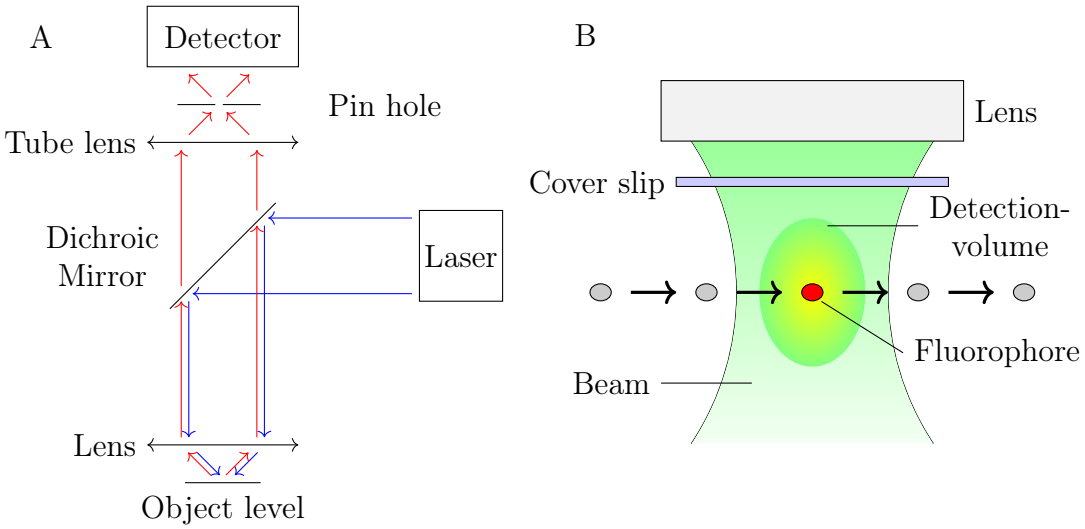

Figure 2.5: Schematic of the fluorescence fluctuation measurement principle. **A** A laser emits light (blue) that falls on a dichroic mirror. The mirror directs the light through an objective onto the sample. Fluorophores excited in the sample begin to emit photons (red). Due to the Stokes shift, the emitted light can now pass through the dichroic mirror. A tube lens focusses the light onto a pinhole which improves the signal-to-noise ratio by cutting off photon events from other planes. A detector counts the incident photons. **B** A diffusing fluorophore enters the detection volume and is excited to fluorescence. The mean residence time in the volume is correlated with the diffusion coefficient of the fluorophore. Reproduced from [54, p. 4].

generally used for FFS experiments. Focussing the laser on a tiny volume, fluorescence fluctuations occur, which are caused by concentration fluctuations. These fluctuations are subject to FFS analysis. Since confocal optics are required to measure these fluctuations, they will henceforth be presented.
The intensity profile of a laser near the focal point can be described by a *Gauss profile* in radial direction and a *Lorentz profile* in the z-direction [28, p. 169].

$$I(x,y,z) = \frac{2P}{\pi w^2(z)} \exp\left(-2\frac{(x^2+y^2}{w(z)^2}\right), \tag{2.14}$$

where x, y, and z represent the three spatial directions. The waist width of the beam is w_0 in the focal plane and defocuses in z-direction with

$$w(z) = \sqrt{w_0^2 + z^2\left(\frac{\lambda_0}{n\,\pi\,w_0}\right)^2}. \tag{2.15}$$

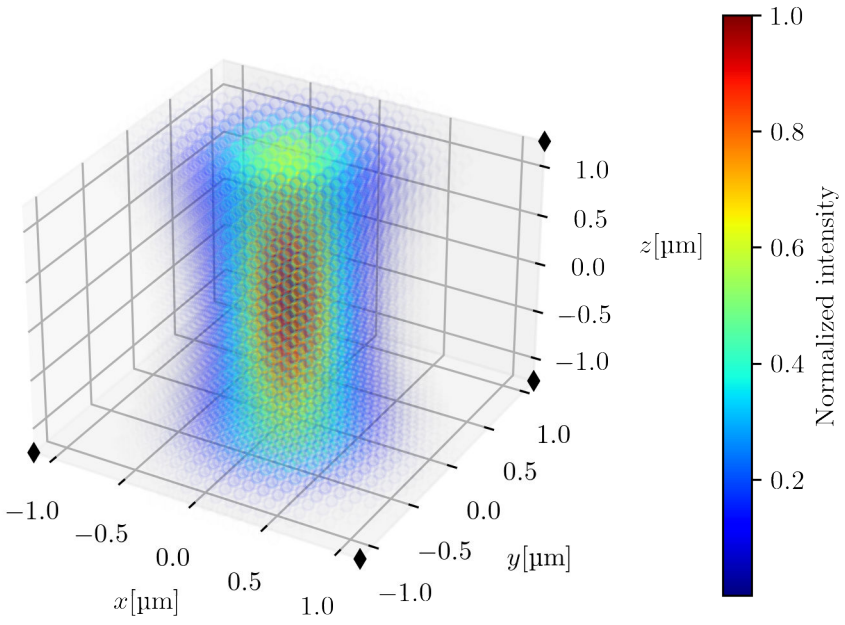

Figure 2.6: Excitation profile of a laser in a confocal setup. The profile is modelled via equation 2.14 with $P = 10\,\mathrm{mW}$, $\lambda_0 = 488\,\mathrm{nm}$, $n = 1$ and $w_0 = 0.5\,\mu\mathrm{m}$.

Figure 2.6 shows the intensity profile of equation 2.14. According to equation 2.6, the excitation of a fluorophore is proportional to the local intensity for intensities far below the saturation intensity. Thus, equation 2.14 sufficiently describes the local excitation of a fluorophore. For the model of a Gaussian-Lorentz profile to be considered valid, the waist width w_0 of the laser needs to be significantly smaller than the radius of the input aperture of the microscope objective used. In addition, the objective lens and the refractive index n of the sample solvent must be compatible [55, p.11-15].
The *point spread function* (PSF) describes the detectability of a point source. The PSF defines the probability with which a light quantum from a point source of the sample reaches the detector. We start the consideration with the semi-geometrical approximation of a luminous point in (x', y', z), which is defined in the focal plane ($z = 0$) as a small disk with a size corresponding to the resolution R_0 of the optical setup. Outside the focal plane, the disc enlarges according to a Lorentz function.

$$R(z) = \sqrt{R_0^2 + z^2 \tan^2(\alpha)} \tag{2.16}$$

The PSF can now be approximated as follows [28, p. 170].

$$\mathrm{PSF}(\mathbf{r}', \mathbf{r}, z) = \frac{\mathrm{circ}\left(\frac{|\mathbf{r}'-\mathbf{r}|}{R(z)}\right)}{\pi R^2(z)} = \begin{cases} \frac{1}{\pi R^2(z)} & \text{for } \frac{\sqrt{(x'+x)^2+(y'+y)^2}}{R(z)} \leq 1 \\ 0 & \text{otherwise} \end{cases} \tag{2.17}$$

The disk area function $\mathrm{circ}(\mathbf{r})$ is a step function which has the value 1 for radii $|\mathbf{r}| \leq 1$ and otherwise the value 0.
The influence of the pinhole on the image plane of the microscope can be described by the *collection efficiency function* $CEF(\mathbf{r}', z)$. The CEF indicates the proportion of light from a point source that passes through the pinhole [56, p. 1319-1321]. The transmission

function of the pinhole is represented by the disk function [28, p. 170]

$$T(\mathbf{r}') = \mathrm{circ}\left(\frac{\mathbf{r}'}{s_0}\right) = \begin{cases} 1 & \text{for } \frac{|\mathbf{r}'|}{s_0} \leq 1 \\ 0 & \text{otherwise,} \end{cases} \tag{2.18}$$

with s_0 as the radius of the pinhole. With these concepts, the CEF can be defined as follows [57, p. 1187]

$$\mathrm{CEF}(\mathbf{r}, z) := \frac{1}{\Delta} \int T(\mathbf{r}')\, \mathrm{PSF}(\mathbf{r}', \mathbf{r}, z)\, \mathrm{d}^2 r'. \tag{2.19}$$

The term $\Delta = \int T(\mathbf{r}')\mathrm{PSF}(\mathbf{r}', \mathbf{r} = 0, z = 0)\, \mathrm{d}^2 r'$ normalizes the expression. The *molecule detection efficiency* (MDE) is defined as the CEF multiplied by the excitation intensity I_{exc} [28, p. 171]:

$$\mathrm{MDE}(x, y, z) = \mathrm{CEF}(x, y, z)\, I(x, y, z). \tag{2.20}$$

In FFS experiments, a three-dimensional Gaussian ellipsoid is usually assumed for approximating the MDE [28, p. 172-174][58, p. 2300].

$$\mathrm{MDE}(x, y, z) \approx W(\mathbf{r}) = W_0\, e^{-\frac{2(x^2+y^2)}{r_0^2}}\, e^{-\frac{2z^2}{z_0^2}} \tag{2.21}$$

The scalar factor W_0 includes the excitation intensity of the laser, the transmission loss through the optical setup and the efficiency of the photodetector. This approximation is justified for an appropriate choice of optical components. Normalizing equation 2.21 gives

$$\widehat{W}(\mathbf{r}) = e^{-\frac{2(x^2+y^2)}{r_0^2}}\, e^{-\frac{2z^2}{z_0^2}}. \tag{2.22}$$

Figure 2.7 shows a Gaussian ellipsoid according to equation 2.22. The MDE corresponds to the observation volume in fluorescence fluctuation experiments. Particles that diffuse through the laser profile are excited to fluoresce. According to the MDE, the emitted photons are detected with a certain probability by the detector of the measuring apparatus.

2.2.3 Non-gaussian observation volume

For fluorescence fluctuation measurements, a Gauss profile is usually assumed for the observation volume. However, it has been shown that this assumption is not tenable for many confocal microscope systems. A non-Gaussian observation volume leads to difficulties in fitting the models to the data. This is usually shown by oscillations in the fit residuals. It is often tried to improve the fit by extending the models by introducing exponential terms or using two-component models for a one component system. These adjustments usually significantly improve the fit of the data. However, they do not reflect the physics. Hess and Webb [58] have investigated these effects thoroughly. They could show that the non-Gaussian shape of the observation volume is mainly caused by the illumination of the objective and detector apertures. An overfilling of the detector aperture (realized by a pinhole or a glass fiber in confocal setups) leads to a strong deviation from the Gauss profil. This leads to fringes in the observation volume which are far away from the focus of the lens and contribute to the FFS analysis. Due to their spatial expansion,

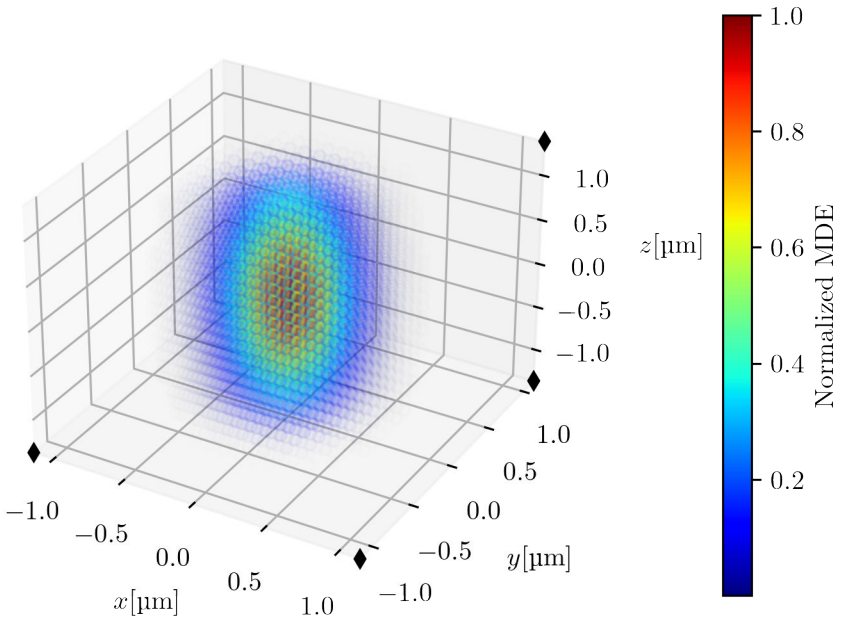

Figure 2.7: Normalized molecular detection efficiency (MDE). The MDE is approximated by a Gaussian ellipsoid using equation 2.22 with $r_0 = 0.5\,\mu m$ and $z_0 = 1.5\,\mu m$.

they occupy a large volume and lead to much larger axial ratios than expected, up to a divergence of the ratio to infinity. An extension of the model by the above terms then improves the fit significantly. It should be noted that if an optical fiber is used instead of a pinhole, it usually has a larger effective diameter than specified. Therefore, optical fibers as confocal apertures cannot guarantee a Gaussian observation volume [58, p. 2305-2316]. A way out is provided by non-analytical models that do not rely on a Gauss profile. However, the calculation of these models is much more complex, which is why they are rarely used. When using 2-photon lasers, the assumption of a Gaussian profile is usually justified [58, p. 2311].

2.2.4 Fluorescence saturation in FFS experiments

Besides optics, photophysical quantities also have an influence on FFS experiments. Especially fluorescence saturation, which has already been presented in section 2.1, needs to be mentioned here. In the case of fluorescence saturation, the approximation of the MDE by a Gaussian ellipsoid (see section 2.2.2) is no longer tenable and equation 2.22 needs to be adjusted. A model for the MDE that takes saturation effects into account is given by [59, p. 3+5]:

$$\widehat{W}_{\mathrm{sat}}(\mathbf{r}) = (1 + \frac{I_{\mathrm{exc}}}{I_{\mathrm{s}}}) \frac{\widehat{W}(\mathbf{r})}{1 + \frac{I_{\mathrm{exc}}}{I_{\mathrm{s}}} \widehat{W}(\mathbf{r})} \tag{2.23}$$

It should be noted that numerator and denominator are represented by the same distribution. This is not physically exact, but as an approximation it is well suited to describe the experimental findings [59, p. 4]. Figure 2.8 shows the change in shape of the Gauss profile along the lateral axis for different intensity ratios $\frac{I_{\mathrm{exc}}}{I_{\mathrm{s}}}$.
It becomes clear how for increasing $\frac{I_{\mathrm{exc}}}{I_{\mathrm{s}}}$ ratios the Gauss profile becomes more and more distorted and a clear plateau is formed, which leads to systematic deviations in the anal-

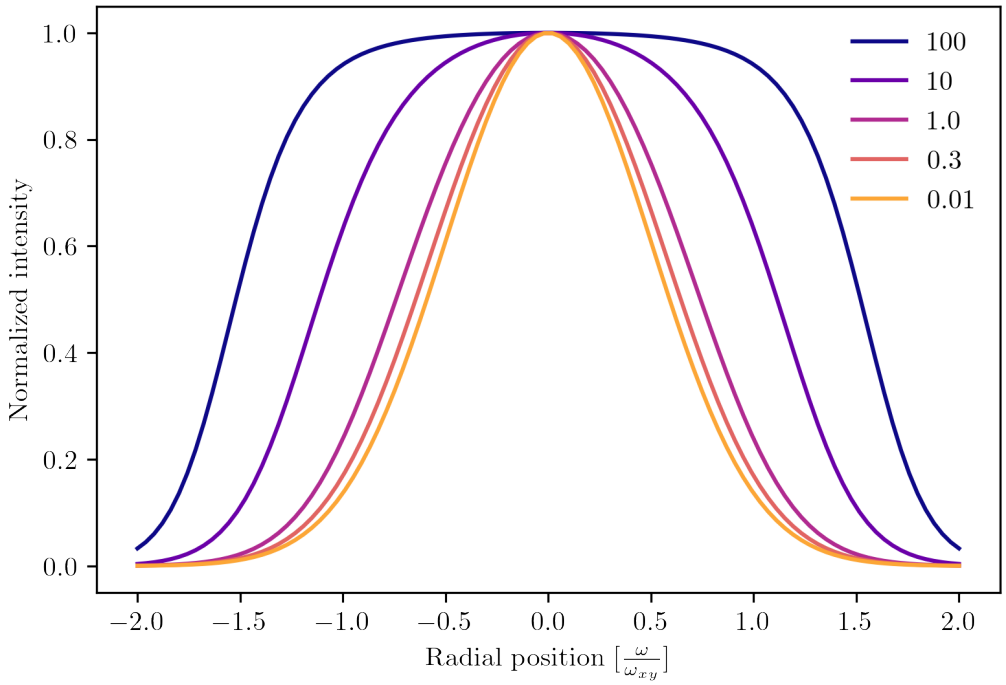

Figure 2.8: Influence of fluorescence saturation on the molecular detection efficiency. Representation of a normalized Gaussian ellipoid along the lateral axis for different excitation to saturation intensity ratios $\frac{I_{\mathrm{exc}}}{I_{\mathrm{s}}}$. Reproduced from [59, p. 4].

ysis of FFS experiments. Thereby especially the observation volume is overestimated. To minimize the influence of fluorescence saturation in FFS experiments, the excitation intensity should not be set too high. A measurement series with increasing excitation intensities can be used to determine up to which power the increase in fluorescence is linear with the excitation intensity.

2.2.5 Modelling diffusion

After a closer look at confocal optics in FFS experiments, the diffusive processes that lead to fluctuations in the studied fluorescence signal are now described.

Molecule diffusion

As mentioned earlier, fluorescence fluctuation spectroscopy exploits concentration fluctuations in a tiny observation volume to gather information about fluorescent particles in solution. These concentration fluctuations are caused by diffusive motions of the particles because of *Brownian molecular motion*. These thermal fluctuations in fluids were initially described by Brown in 1827 in his microscopic observations of floating pollen [60]. The following introduction to diffusion can be read in detail here [61, p. 6-18+37-39]. To start with, the *Einstein diffusion equation* generally describes the microscopic transfer of matter and heat [61, p. 38].

$$\partial_t\, p(\mathbf{r}, t|\mathbf{r}_0, t_0) = D\nabla^2 p(\mathbf{r}, t|\mathbf{r}_0, t_0) \tag{2.24}$$

where $p(\mathbf{r}, t|\mathbf{r}_0, t_0)$ is a stochastic process that describes the probability of finding a particle with diffusion coefficient D at location $\mathbf{r}$ at time t given that it was at location $\mathbf{r}_0$ at time

t_0. Using the following initial and boundary conditions

$$p(\mathbf{r}, t \to t_0|\mathbf{r}_0, t_0) = \delta(\mathbf{r} - \mathbf{r}_0), \qquad p(|\mathbf{r}| \to \infty, t|\mathbf{r}_0, t_0) = 0, \tag{2.25}$$

we can derive the so-called *Wiener process* [61, p. 38]. The process, described by $\mathbf{r}(t)$ for $t \geq 0$, is characterized for d dimensions by the following probability distribution [61, p. 39]:

$$p(\mathbf{r}, t|\mathbf{r}_0, t_0) = (4\pi\, D\, \Delta t)^{-\frac{d}{2}} \exp\left(-\frac{(\mathbf{r} - \mathbf{r}_0)^2}{4D\, \Delta t}\right) \tag{2.26}$$
$$\text{with } \Delta t = (t_1 - t_0).$$

The Wiener process is a *Markov process*, meaning its conditional probabilities depend only on $\mathbf{r}_0$ and t_0. Equation 2.26 is also referred to as the *Green's function*. The mean squared displacement (MSD) is an experimentally accessible measure for the spatial extent of the diffusive motion of a particle. For the MSD, the following relationship can be derived from the above *Einstein diffusion equation* 2.24 [61, p. 38]

$$\left\langle (\mathbf{r}(t) - \mathbf{r}(t_0))^2 \right\rangle = 2N\, D\, \Delta t, \qquad \text{for } N \text{ dimensions.} \tag{2.27}$$

Now, the relationship between the theoretical modeling of diffusion as a Wiener process and the description by a discrete random process will be presented in more detail. To simulate diffusion as a discrete process, the model of a random walk can be used. A random walk is realized as a stochastic sequence S_n, with $S_0 = 0$, defined by [61, p. 14]

$$S_n = \sum_{t=1}^{n} X_t. \tag{2.28}$$

X_t is an independently and identically distributed random variable. In free diffusion (without drift) there is an equal probability in all spatial directions for the particle to move, thus the random walk is *symmetric*. In figure 2.9 we see the distribution of 10000 random walkers in 1D along with the probability density functions for different Δt.
The particles started at the origin and moved randomly stepwise forward and backward in discrete simulated time steps. The distributions shown are snapshots after different elapsed time intervals Δt. They become broader over time. For a finite volume we get a homogeneous distribution over the whole volume in the limit. For the limiting case of infinitely short time steps, the discrete path in time and space of the random walk becomes a continuous wave and can be described as a Wiener process. For the one-dimensional case, according to equation 2.26, the Wiener process is given by the following expression [61, p. 10]

$$p(\omega_1, t_1|\omega_0, t_0) = \frac{1}{\sqrt{4\pi\, D\, \Delta t}} \exp\left(-\frac{(\Delta\omega)^2}{4D\, \Delta t}\right) \tag{2.29}$$
$$\text{with } \Delta\omega = (\omega_1 - \omega_2).$$

As we see in figure 2.9, the probability density distribution of a one-dimensional Wiener process perfectly describes the distribution from the discrete random walk at any elapsed time Δt. An exemplary random walk in 3D as part of an FFS simulation can be seen in section 3.1 in figure 3.1.

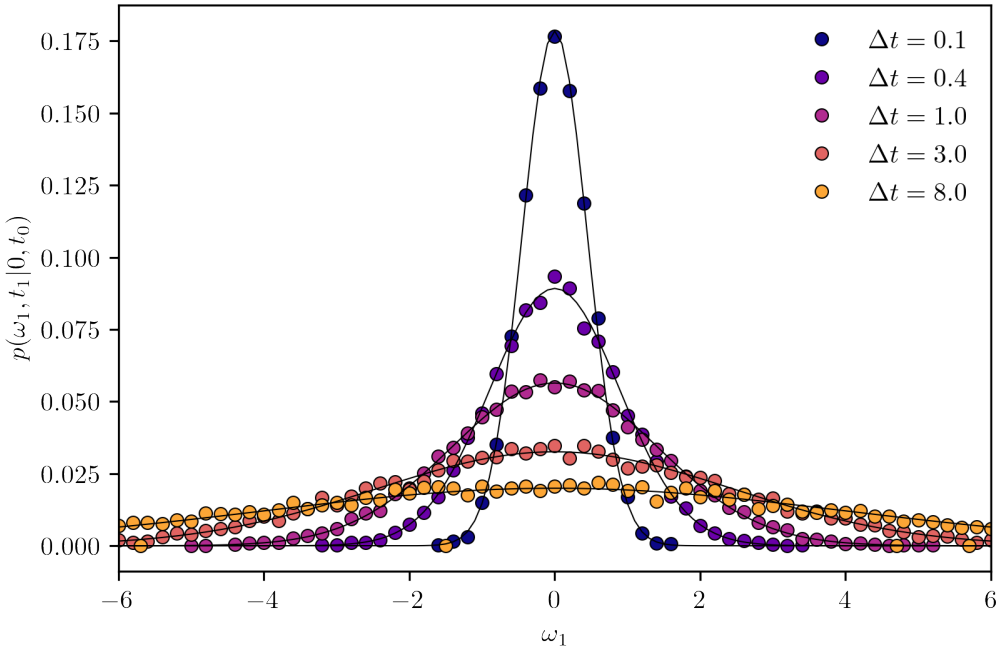

Figure 2.9: Random walk of diffusing particles along an axis starting at the origin. The stepwise forward and backward motion of 10000 particles along an axis is simulated ($D = 1, \epsilon = 0.1$). The distribution density is calculated for different time intervals according to equation 2.29. Based on [61, p. 10] and complemented by the computation of a random walk.

2.2.6 Diffusion of nucleic acids

In the present work, we will also address the diffusion of nucleic acids. The nucleic acids DNA (deoxyribonucleic acid) and RNA (ribonucleic acid) consist of a sugar backbone of ribose, which are linked together by a phosphodiester bond. The bases adenine, thymine (in RNA uracil), guanine and cytosine are the actual carriers of genetic information. They are each located on a ribose phosphate monomer and together form a nucleotide. The sequence of the nucleotides determines the genetic code. The bases of the nucleotides form hydrogen bonds to other bases in an aqueous environment. Adenine and thymine (in RNA uracil) as well as guanine and cytosine preferably form hydrogen bonds to each other. Due to this interaction, complementary nucleic acids come together on their own and form a double strand, which in the case of double stranded DNA (dsDNA) winds into a double helix. In the body, the much more stable double strand is the predominant form of DNA. An important property of nucleic acids is the negative charge due to the phosphodiester bond and the phosphate group at the 5' end of the molecule. Because of the formation of a double helix, double-stranded DNA is much more rigid than single-stranded nucleic acids.

To describe the diffusive dynamics of nucleic acids satisfactorily, we need to consider this rigidity of the polymer, which is called the persistence length. The persistence length is particularly important when considering short nucleic acid fragments, which behave like rods below the persistence length. At very long fragment lengths, on the other hand, they behave like a flexible chain.

Rod shaped

In the first case, we consider a rod-shaped polymer whose diffusion coefficient can be described by a cylinder with thickness d and length L for $2 < L/d < 30$ [62, p. 2047-2048]

$$D = \frac{A\, k_\mathrm{B} T}{3\pi\eta L}, \quad \text{with } A = \ln\frac{L}{d} + 0.312 + 0.565\frac{d}{L} - 0.100\frac{d^2}{L^2}. \tag{2.30}$$

k_B is the *Boltzmann constant*, T is the absolute temperature and η is the viscosity of the solvent. This approach does not consider internal dynamics of the rods.

Ideal chain

In case of an ideally flexible polymer the *Zimm model* can be employed [63]. It considers the hydrodynamic interactions of the polymer segments with each other. The moving segment in the solvent generates a flow field, which in turn affects other segments. The diffusion constant of the center of gravity of the polymer is given by [64, p. 17-18]

$$D = \frac{8 k_\mathrm{B} T}{3(6\pi^3)^{1/2}\eta R_\mathrm{ee}} \approx 0.196\frac{k_\mathrm{B} T}{\eta R_\mathrm{ee}}. \tag{2.31}$$

R_ee describes the distance between the two ends of the polymer chain and is dependent on the bending properties of the polymer, thus its persistence length l_p. Considering an ideal chain with $l_\mathrm{p} \ll L$, we obtain for the Zimm model the relation [64, p. 7-10]

$$R_\mathrm{ee} = \sqrt{2\, L\, l_\mathrm{p}}. \tag{2.32}$$

It is notable that equation 2.31 of the Zimm model resembles the well-known *Stokes Einstein equation*

$$D = \frac{k_\mathrm{B} T}{6\pi\, \eta\, R_\mathrm{h}}. \tag{2.33}$$

The diffusive behavior can be interpreted as that of a hard sphere with hydrodynamic radius

$$R_\mathrm{h} = \frac{R_\mathrm{ee}}{6\pi\, 0.196}. \tag{2.34}$$

Semiflexible polymer

The diffusive behavior of biomolecules such as DNA cannot be satisfactorily described for fragment lengths $<100\,000$ bp using the Zimm model [65, p. 3]. This is due to the relatively large persistence length of DNA, which means that bending modes must be considered due to the stiffness of the polymer. The theory for the transition region from the rod-shaped particle to the ideal chain was elaborated by Harnau et al. [66]. For the diffusion coefficient, the model is described by the following expression, which contains an integral over the parameter s representing the parameterization along the polymer:

$$D = \frac{k_\mathrm{B} T}{3\pi\, \eta\, L}\left[1 + \frac{\sqrt{6}}{\sqrt{\pi}\, L}\int_d^L \mathrm{d}s \frac{(L-s)}{\sqrt{a(s)}} \exp\left(-\frac{3d^2}{2a(s)}\right)\right], \tag{2.35}$$

with $a(s)$ given by

$$a(s) = \begin{cases} |s|2l_\mathrm{p} & \text{for } s > l_\mathrm{p}, \\ s^2 & \text{otherwise.} \end{cases} \tag{2.36}$$

The function $a(s)$ describes the predictions for a random coil for spatial scales greater than the persistence length. For smaller scales, the function shows the behavior of a rigid rod. This transition region is in the range of several persistence lengths of the polymer.

Figure 2.10 shows a comparison between the rod model and the Zimm model with the two cases ideal chain and semiflexible polymer. For the diffusion modeling, the persistence length of double-stranded DNA under near-physiological salt concentrations was approximated by $l_\mathrm{p} = 51\,\mathrm{nm}$ or $150\,\mathrm{bp}$ [67, p. 6188][68, p. 3607][65, p. 3]. In fact, the persistence length of DNA depends on a variety of factors such as ionic strength of the solvent, temperature, presence of proteins, or solvent type. The models for the

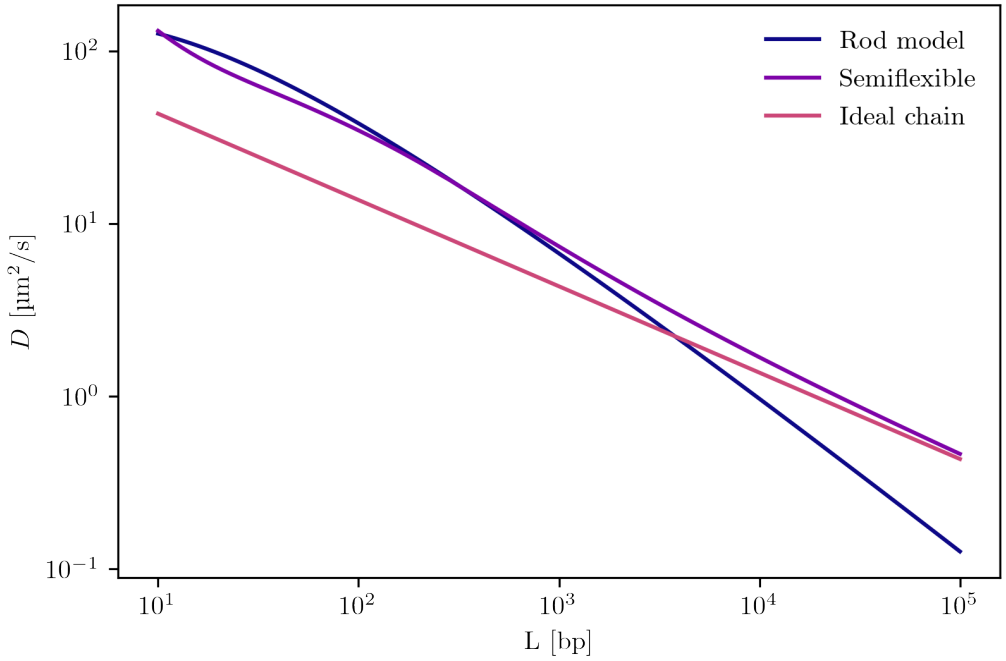

Figure 2.10: Comparison of three models to describe the diffusion of DNA. For short fragment lengths the rod model is a good approximation and for long fragments the ideal chain model. The semiflexible model, on the other hand, describes the diffusion behavior over the entire fragment length distribution. The used parameters are $l_\mathrm{p} = 51\,\mathrm{nm} = 150\,\mathrm{bp}$ and $d = 2.5\,\mathrm{nm}$. The rod model is calculated using equation 2.30. The semiflexible chain is modeled by solving equation 2.35 numerically. The Zimm model for the ideal chain is calculated via equation 2.31.

rod-like polymer and the ideal chain show different slopes. The rod model predicts higher diffusion coefficients for short polymers, but then falls off more steeply. For the ideal chain, we can observe an almost linear relation in the double logarithmic representation:

$$D \propto L^\nu, \qquad \text{with } \nu = \frac{1}{2}. \tag{2.37}$$

The semiflexible polymer model gives quite similar diffusion coefficients compared to the rod model for small fragment lengths (at $\approx 10\,\mathrm{bp}$) and approaches an ideal gaussian chain for very large fragment lengths. It thus represents the persistence length dependent transition between these two models.

2.3 Fluorescence correlation spectroscopy

A proven method for the analysis of stationary fluctuations in a signal trace is autocorrelation. Autocorrelation is a term from stochastics and signal processing and describes the correlation of a time series $x(t)$ with itself shifted in time $x(t+\tau)$ [54, p. 2]. Autocorrelations are calculated on series of time-dependent data to clarify non- random relationships in time series. For example, if a fluorophore diffuses through the confocal volume, there is a certain chance that the fluorophore will still be found in the volume at a later time. Therefore, the correlation between the signal at time t and the signal at time $t+\tau$ will be greater than zero. Generally, the autocorrelation r_{xx} of a time-data sequence $x(t)$ is defined as

$$r_{xx} = \langle x(t)x(t+\tau)\rangle_t. \tag{2.38}$$

The expression $\langle \dots \rangle_t$ denotes the time average of an expression over the time variable t [54, p. 2]:

$$\langle x(t)\rangle_t = \lim_{T\to\infty} \frac{1}{T} \int_0^T x(t)\,\mathrm{d}t \tag{2.39}$$

In fluorescence correlation spectroscopy (FCS), the intensity trace $I(t)$ is the only measured quantity and can be regarded as a stationary stochastic process. It contains all information about the involved dynamic processes [64, p. 25-27]. For FCS, the autocorrelation is calculated for small intensity fluctuation in the detection volume, originating from the underlaying stochastic processes. The intensity fluctuation $\delta I(t)$ at a certain time is given by [53, p. 10]:

$$\delta I(t) = I(t) - \langle I(t)\rangle_t \tag{2.40}$$

By normalizing the autocorrelation 2.38 to its squared mean intensity $\langle I(t)\rangle_t^2$ and considering that the time-data sequence consists of real values, the known form of autocorrelation is obtained [53, p. 11].

$$G(\tau) = \frac{\langle \delta I(t)\cdot \delta I(t+\tau)\rangle_t}{\langle I(t)\rangle_t^2} \tag{2.41}$$

Inserting equation 2.40 into equation 2.41, the autocorrelation function can be transformed into:

$$G(\tau) = \frac{\langle I(t)\cdot I(t+\tau)\rangle_t}{\langle I(t)\rangle_t^2} - 1. \tag{2.42}$$

In this form the autocorrelation can be computed from a given fluorescence trace of a measurement. Figure 2.11 shows exemplary the fluorescence trace and the calculated autocorrelation of an FCS experiment. In the left graph, the intensity fluctuation in the signal during the measurement can be seen. They result from diffusion-related concentration fluctuations in the detection volume and illustrate the stochastic character of the time series. Since it is a stationary process, the mean fluorescence rate and the mean variance in the signal do not change over time. The graph on the right shows the calculated autocorrelation from the fluorescence trace. The time axis is logarithmic. For small time shifts τ the autocorrelation is > 0 and drops to 0 for increasing τ. The shape of the autocorrelation curve is sigmoidal. With a suitable model, information about the measured species in solution can be derived from the amplitude and the sigmoidal course of the autocorrelation data.

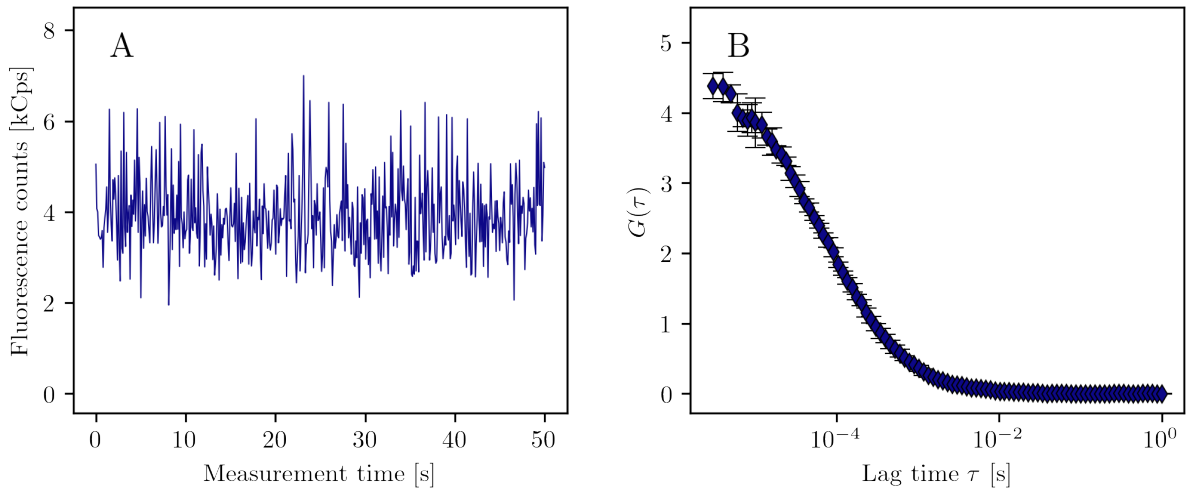

Figure 2.11: The autocorrelation reveals hidden information in fluorecence fluctuations. **A** Fluorescence trace of an FFS experiment. **B** Autocorrelation curve from the fluorescence trace. The amplitude and the temporal course contain information about the diffusing species.

2.3.1 Diffusion model of FCS

A suitable model is necessary to the analysis the autocorrelation curves of an FFS experiment. The derivation of the analytical standard model of FCS is given, e.g., in Schwille and Haustein [53, p. 10-18]. The standard FCS model is based on a single excitation source in continuous wave mode and a confocal measurement setup. We start with the measured fluorescence intensity, which depends on the geometry of the considered volume and the fluctuations of the fluorophore concentration $C(\mathbf{r}, t)$ in the system [64, p. 25]:

$$I(t) = \int_V \mathrm{MDE}(\mathbf{r})\, C(\mathbf{r}, t)\, \mathrm{d}^3 r. \tag{2.43}$$

Here, the fluorophore's fluorescence properties are assumed to be constant over time. The molecular detection efficiency $\mathrm{MDE}(\mathbf{r})$ characterizes the detection volume and combines both the excitation laser profile $I(\mathbf{r})$ and the detection geometry described by the collection efficiency function $\mathrm{CEF}(\mathbf{r})$ (see equations 2.19 and 2.20). For a confocal detection apparatus, the MDE is well approximated by a Gaussian ellipsoid 2.21 with radius r_0 in the xy-plane and extension z_0 in the z-direction (see section 2.2.2). Inserting equation 2.43 into the definition of the autocorrelation for FCS 2.42 and considering the case of one diffusing species results in [53, p. 11]

$$G(\tau) = \frac{\int_V \int_V W(\mathbf{r})\, W(\mathbf{r}')\, \langle \delta C(\mathbf{r}, t) \delta C(\mathbf{r}', t+\tau) \rangle\, \mathrm{d}^3 r\, \mathrm{d}^3 r'}{(C \int_V W(\mathbf{r})\, \mathrm{d}^3 r)^2}. \tag{2.44}$$

For an ideal solution of freely diffusing point-like particles in an open 3D volume, the concentration fluctuations in the system at any given time are independent and spatially uncorrelated. In this case with diffusion coefficient D, the following expression holds [53, p. 12]:

$$\langle \delta C(\mathbf{r}, 0) \delta C(\mathbf{r}', \tau) \rangle = \langle C \rangle (4\pi\, D\, \tau)^{-\frac{3}{2}} \exp\left(-\frac{(\mathbf{r} - \mathbf{r}')^2}{4 D\, \tau} \right). \tag{2.45}$$

The right-hand side can be identified as *Green's function* in 3D 2.26. Inserting equation 2.45 into equation 2.44 yields [53, p. 13]:

$$G(\tau) = \frac{1}{\langle C\rangle (4\pi\, D\, \tau)^{\frac{3}{2}}} \frac{\int_V \int_V W(\mathbf{r})\, W(\mathbf{r}')\, \exp\left(-\frac{(\mathbf{r}-\mathbf{r}')^2}{4D\,\tau}\right) \mathrm{d}^3 r\, \mathrm{d}^3 r'}{(\int_V W(\mathbf{r})\, \mathrm{d}^3 r)^2}. \tag{2.46}$$

Using the definition of the effective detection volume and considering the approximation of the MDE by a Gaussian profile 2.21, we get [53, p. 13]

$$V_{\text{eff}} := \frac{(\int_V W(\mathbf{r})\, \mathrm{d}^3 r)^2}{\int_V W^2(\mathbf{r}) \mathrm{d}^3 r} = \pi^{3/2} r_0^2 z_0. \tag{2.47}$$

V_{eff} thus depends exclusively on the waist parameters of the confocal optics. Using the following relationship for the diffusion coefficient [53, p. 13]

$$D = \frac{r_0^2}{4\tau_{\text{D}}}, \tag{2.48}$$

and considering the mean molecule number $\langle N\rangle$ in the effective detection volume as

$$\langle N\rangle = \langle C\rangle V_{\text{eff}}, \tag{2.49}$$

equation 2.46 can be solved analytically and gives an expression for the free diffusion of a particle species in 3D [53, p. 13]:

$$\begin{aligned} G(\tau) &= \frac{1}{\langle N\rangle} \frac{1}{1+\frac{\tau}{\tau_{\text{D}}}} \frac{1}{\sqrt{1+\frac{r_0^2}{z_0^2}\frac{\tau}{\tau_{\text{D}}}}} \\ &= \frac{1}{\langle N\rangle} g_{\text{3DG}}(\tau). \end{aligned} \tag{2.50}$$

$g_{\text{3DG}}(\tau)$ is called the correlation function for free diffusion in 3D assuming a Gaussian profile for the MDE. Figure 2.12 shows data series generated using equation 2.50 for varying parameters. In a semi-logarithmic representation, the FCS curves resemble a decreasing sigmoidal curve. Decreasing diffusion coefficients, i.e., slower diffusing molecules, shift the FCS curves to larger shifting times τ (subplot A). The limit value for $\tau \to 0$ corresponds to the reciprocal particle number $\frac{1}{\langle N\rangle}$ in the effective volume. Subplot B shows this dependency. For increasing mean particle numbers in the effective volume, the amplitude of the FCS curves decreases.

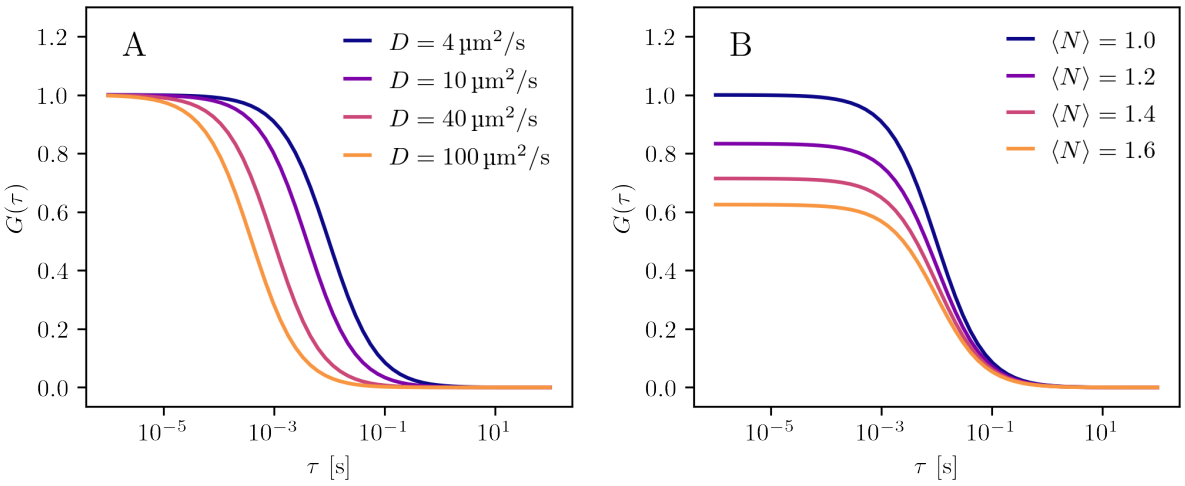

Figure 2.12: The FCS model for varying parameters. **A** Varying diffusion coefficients D. **B** Varying mean molecule numbers in the effective detection volume $\langle N \rangle$.

2.3.2 Photokinetic effects in FCS

Diffusive processes take place on comparatively large time scales. However, there are other photokinetic effects that can be observed on very small time scales. Frequently occurring processes are rotational diffusion, triplet states of the fluorescent dye, as well as isomerization effects. These short-time phenomena have an influence on the emission characteristics of the particles under study [69, p. 174-185]. Since rotational diffusion arises on the order of nanoseconds and cannot be resolved in our setting, it is neglected in our studies. In contrast, triplet states and isomerization effects are not negligible and are discussed in the following.

Triplet state effects in FCS

The probably most important photokinetic effect is the triplet decay [64, p. 30-32]. This is caused by the long-lived triplet state (see the Jablonski diagram in figure 2.1). The transition of a fluorophore into a triplet state means that the fluorophore cannot emit photons for a certain time. Like the translational diffusion of molecules, the change between the singlet and triplet states leads to fluorescence fluctuations. Since these fluctuations occur at much smaller time scales, the intensity fluctuations of diffusion and singlet-triplet transitions can be considered independent of each other [70, p. 13371]. For the observation of the fluctuations of the relatively fast single-triplet transitions the fluorophores can be assumed to be immobile. In contrast, for the observation of diffusive processes, caused by the movement of the fluorophores, the singlet-triplet interactions are in a steady-state [70, p. 13371]. The normalized diffusive triplet model is [71, p. 152]:

$$g_{\text{trip}}(\tau) = 1 + \frac{F_{\text{trip}}}{1 - F_{\text{trip}}} \exp^{-\frac{\tau}{\tau_{\text{trip}}}} . \tag{2.51}$$

F_{trip} is the fraction of fluorophores in the dark triplet state and τ_{trip} is the triplet-state relaxation time. Since triplet state transitions are usually much faster than the diffusive process through the detection volume, the two processes can be linked multiplicatively.

$$G(\tau) = \frac{1}{\langle N \rangle} g_{\text{3DG}}(\tau)\, g_{\text{trip}}(\tau) \tag{2.52}$$

Figure 2.13 shows the proportion of the triplet state in the FCS. In subplot A, the two

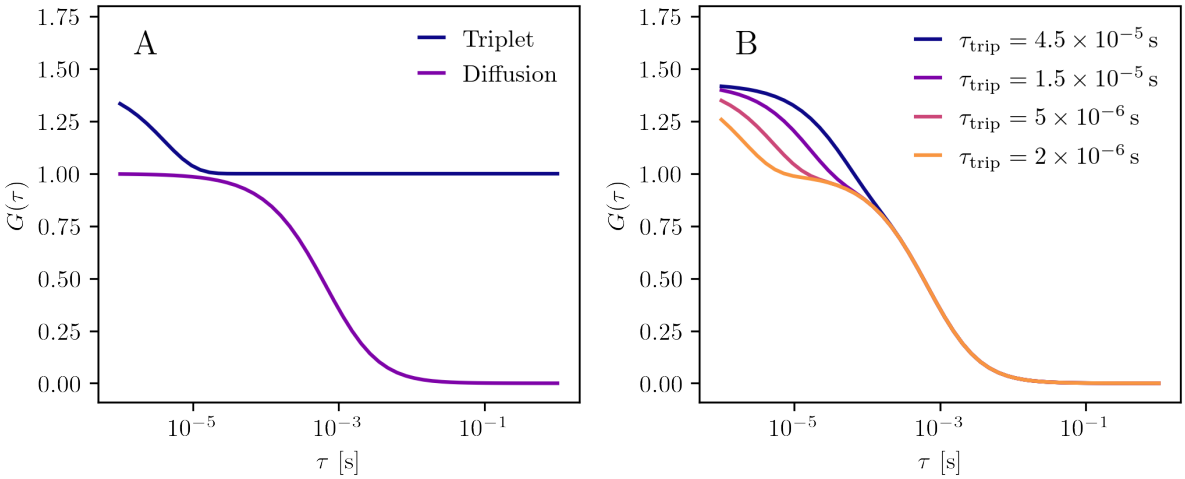

Figure 2.13: Visualization of the triplet model in FCS analysis. **A** Plot of the triplet term g_{trip} and the diffusion term g_{diff}. **B** Product of g_{trip} and g_{diff} for varying relaxation times and constant triplet fraction F_{trip}.

portions of the model are shown as individual data series. For short time intervals, the triplet state forms a considerable part of the FCS. For longer times, the triplet fraction drops to one. Since the complete model is a multiplication of the two terms, the triplet fraction disappears for large τ. Subplot B shows the combined model for varying relaxation times with constant triplet fractions. Increasing relaxation times shift the triplet fraction of the model to larger τ. It also becomes clear that in the case of a superposition of diffusion and triplet state, a distinction of the fractions becomes difficult. Usually, the decay times of the triplet state are significantly smaller than the diffusion times and a good separation of the the components is possible. In case of an overlapping of the diffusive part and the triplet effect, the latter can be reduced by lowering the excitation intensity, thus, facilitating the differentiation.

Isomerization effects in FCS

A widely used dye family in fluorescence measurements are cyanine dyes including the unsymmetric cyanine dyes RiboGreen and PicoGreen which are ideally suited for the fluorescent labeling of nucleic acids [72, 73]. Many cyanine dyes exhibit a characteristic cis-trans isomerization in their hydrocarbon backbone, resulting in blinking upon fluorescence emission [74, p. 290-293]. This isomerization affects the photophysical properties of the dyes and differs significantly between different dyes [74, p. 290-293]. Thus, when working with cyanine dyes for fluorescent labeling, this effect must be considered.
Most simply, isomerization can be regarded as a two-state system switching between a bright and dark state. For modeling isomerization, the diffusion process can be viewed as stationary, since it proceeds much slowler than isomerization. This allows to consider the processes independently. With this assumption, the same expression is obtained for a simple on/off system as for the description of the triplet state [64, p. 54-65]:

$$g_{\text{iso}}(t) = 1 + \frac{F_{\text{iso}}}{1 - F_{\text{iso}}} \exp^{-\frac{t}{\tau_{\text{iso}}}} . \tag{2.53}$$

Here F_{iso} is the fraction of fluorophores in the non-emissive dark state and τ_{iso} arises from the sum of the switching rates k_{on} and k_{off}. Using a simple isomerization model for fluorescence correlation spectroscopy, the blinking of GFP proteins was studied [69], as was the cis-trans isomerization of the cyanine dye Cy5 [75]. The simplified on/off model represents an approximation, since in the present case M fluorophores intercalate with a DNA polymer. Such a system displays a *finite birth and death process* involving $M + 1$ states ranging from completely dark to all fluorophores emitting. Keller [64, p. 54-65] has mathematically described such a system for fluorescence correlation spectroscopy analysis. Even though no closed analytical expression can be given for the representation of such a system, it consists at least of superimposed exponential functions with the eigenvalues as decay constants.

$$g_{\text{iso}}(t) = \sum_{i=0}^{M} b_i \, \exp\left(\lambda_i \, t\right) \tag{2.54}$$

In general, the binary on/off isomerization model provides a sufficiently good description of experimental data [24, p. 1887]. Hence, it is used throughout this thesis for the analysis of fluorescence fluctuations in DNA measurements.

2.3.3 Error estimation in FCS experiments

To accurately evaluate the FCS data, an error estimate of the FCS is needed. There are several methods to calculate the standard deviation directly from the fluorescence trace [76, 77]. However, the simplest option is to calculate the standard deviation from the autocorrelated data of several measurements, or alternatively from a single measurement that has been split into several subsamples. The FCS signal represents the correlation level above the random background noise[76, p. 1939]. Thus, for error estimation $G(\tau) - G_\infty$ is considered and a normalized value for all data points can be defined [77, p. 2992]:

$$\bar{g}(\tau) = \frac{1}{L} \sum_{l=1}^{L} \frac{G_l(\tau) - G_{l,\infty}}{G_l(0) - G_{l,\infty}}. \tag{2.55}$$

L is the number of averaged FCSs (single measurements or subsamples of one measurement) and l the corresponding index. The standard deviation is thus calculated as follows [77, p. 2992]:

$$\sigma_{\text{FCS}}(\tau) = \sqrt{\frac{1}{L-1} \sum_{l=1}^{L} \left(\frac{G_l(\tau) - G_{l,\infty}}{G_l(0) - G_{l,\infty}} - \bar{g}(\tau) \right)^2}. \tag{2.56}$$

The values for $G(0)$ and $G_{l,\infty}$ can be estimated from averaging multiple measurement points for short- and long-time intervals τ or approximated from a previous unweighted fit. To obtain the standard error of the measurement, we divide the standard deviation by the square root of the number of measurements.

$$\sigma^*_{\text{FCS}}(\tau) = \frac{\sigma(\tau)}{\sqrt{L}} \tag{2.57}$$

Since a normalized value for the calculation of the standard error is used, the result needs to be multiplied by $G(0)$ if non-normalized FCS data are required.

2.4 The mean single-molecule rate (mSMR)

An essential part of this thesis is the development and evaluation of the *mean single-molecule rate* (mSMR) for the analysis of FFS experiments that includes information from both the time and amplitude domain. In the following, the step-by-step derivation of the mSMR model is presented as described in Sparrenberg et al. [24].

2.4.1 Derivation of the mSMR

Probability distributions are described using different types of moments such as ordinary moments, central moments, factorial moments as well as cumulants and factorial cumulants. The ordinary moments of a probability distribution $P(k)$ given by the quantized photon number k are

$$\langle k^m \rangle = \sum_{k=0}^{\infty} k^m P(k). \tag{2.58}$$

The central moments of a discrete probability distribution are defined as follows.

$$\langle \Delta k^m \rangle = \sum_{k=0}^{\infty} (k-\mu)^m P(k) \tag{2.59}$$

with μ being the expected value of the distribution. An important quantity for the characterization of distributions is *Mandel's Q parameter*, which includes the first two ordinary or central moments [78, p. 206][36, p. 564].

$$Q = \frac{\langle \Delta k^2 \rangle - \langle k \rangle}{\langle k \rangle} = \frac{\langle k^2 \rangle - \langle k \rangle^2 - \langle k \rangle}{\langle k \rangle} \tag{2.60}$$

The Q parameter is a measure of the deviation of a measured photon distribution from a Poisson distribution [78, p. 206]. In case of a Poisson distribution $Q = 0$ is observed. Q parameters greater than zero are referred to as super-Poissonian and Q parameters less than zero are called sub-Poissonian [79, p. 12-13]. We study the fluorescence emission of diffusing particles in a tiny volume (~µm^3). The detected photons of a fluorescence emission under homogeneous excitation conditions follows a Poissonian distribution [80, p. 441-442][36, p. 560]. Since the concentration fluctuations in a small volume are also Poissonian distributed [52, p. 81-83][36, p. 557], one would initially assume that photon counts originating from diffusing particles also exhibit a Poisson distribution. However, this is not the case. Diffusion causes concentration fluctuations in an inhomogeneous excitation profile, which introduces intensity fluctuations. These intensity fluctuations lead to correlations between the photon counts, resulting in a broadening of the distribution and thus in super-Poissonian statistics [36, p. 559-560+563]. As Mandel's Q parameter reflects these deviations, it is a suitable measure for the study of photon count distributions [81, 82]. For further analysis, we need to relate the moments of the photon distribution to the fluorescence intensity distribution. Theoretical considerations typically use the continuous distribution of fluorescence intensity. But even for a constant fluorescence intensity, the number of detected photons varies within a defined counting interval. This is due to the quantum mechanical nature of photon emission, which can be described by a Poisson distribution, also known as shot-noise [36, p. 555-556]. Qian and Elliot have derived expressions for the moments of the fluorescence intensity distribution in terms of

cumulants, which in turn are functions of the single-molecule brightness ϵ and the mean number of molecules in the observation volume N [83, 84]. For the first to cumulants of the intensity distribution, we get [81, p. 1957]:

$$\begin{aligned}\kappa_1 &= \langle I \rangle = \gamma_1 \epsilon\, N, \\ \kappa_2 &= \langle \Delta I^2 \rangle = \langle I^2 \rangle - \langle I \rangle^2 = \gamma_2 \epsilon^2 N.\end{aligned} \tag{2.61}$$

The coefficient γ_r is generally defined as [36, p. 565-566]

$$\gamma_r = \frac{\int_V (\overline{PSF}(\mathbf{r}))^r \,\mathrm{d}\mathbf{r}}{\int_V \overline{PSF}(\mathbf{r})\,\mathrm{d}\mathbf{r}}. \tag{2.62}$$

The normalized *point spread function* $\overline{PSF}$ can be approximated by the profile of a Gaussian ellipsoid, which is defined as

$$\overline{PSF}(\mathbf{r}) = \exp\left(-2\frac{(x^2+y^2)}{r_0^2} - 2\frac{z^2}{z_0}\right). \tag{2.63}$$

This gives for the coefficient γ_r the following solutions with $r = 1, 2$:

$$\gamma_1 = 1, \tag{2.64}$$

$$\gamma_2 = \frac{1}{2\sqrt{2}}. \tag{2.65}$$

In the next step we can relate the intensity moments to the photon number moments. In fact, we can express the ordinary moments of the intensity distribution as factorial moments of the photon number distributions [76, p.1940][81, p. 1957],

$$\begin{aligned}\langle I \rangle &= \langle k \rangle, \\ \langle I^2 \rangle &= \langle k(k-1) \rangle = \langle k^2 \rangle - \langle k \rangle.\end{aligned} \tag{2.66}$$

Combining equations 2.61 and 2.66, we can express the Q parameter (equation 2.60) in terms of intensity cumulants.

$$Q = \frac{\kappa_2}{\kappa_1} = \gamma_2 \epsilon. \tag{2.67}$$

This expression is valid on the condition that the sampling time T is significantly shorter than the characteristic diffusion time τ_D of the molecules. We will now abandon this limitation and turn to the general case of arbitrary sampling rates to specify the Q parameter.

$$Q(T) = \frac{\kappa_2(T)}{\kappa_1(T)} \tag{2.68}$$

The sampling time-dependent first intensity cumulant $\kappa_1(T)$ can be displayed as follows [38, p. 3984][40, p. 2724]:

$$\kappa_1(T) = \epsilon\, N = \mu_0\, T\, N \tag{2.69}$$

with $\mu_0 = \frac{\epsilon}{T}$ being the count rate or single-molecule brightness rate of a molecule. The sampling time-dependent second intensity cumulant $\kappa_2(T)$ is defined as [38, p. 3984][40, p. 2724]

$$\kappa_2(T) = \gamma_2\, \mu_0^2\, T^2\, N\, \Gamma_\mathrm{diff}(T). \tag{2.70}$$

The dimensionless binning function Γ_{diff} relates the second intensity cumulant to the data sampling time and is given by [40, p. 2722-2724]

$$\Gamma_{\text{diff}}(T) = \frac{2}{T^2} \int_0^T (T - \tau)\, g(\tau)\, \mathrm{d}\tau \tag{2.71}$$

and includes the correlation function $g(\tau)$. Assuming a Gaussian PSF, the correlation function is specified as follows:

$$g_{3\text{DG}}(\tau) = \left[\left(1 + \frac{\tau}{\tau_{\text{D}}} \right) \sqrt{1 + \frac{\tau}{r^2 \tau_{\text{D}}}} \right]^{-1}, \tag{2.72}$$

with the axial to lateral ratio $r^2 = z_0^2 / r_0^2$ of the Gaussian PSF. This is exactly the same expression for $g_{3\text{DG}}(\tau)$ as in the FCS model in section 2.3.1. Solving equation 2.71 for $g_{3\text{DG}}$ yields [39, p. 2860][41, p. 11]:

$$\Gamma_{\text{diff,3DG}}(T) = \begin{cases} \frac{8}{\alpha^2} \left(\frac{\alpha}{2} - \sqrt{1+\alpha} + 1 \right) & \text{for } r = 1, \\ \frac{4}{\alpha^2 \beta} \left[\frac{\beta(1+\alpha)}{\sqrt{1-\beta}} \operatorname{artanh}\left(\sqrt{1-\beta} \frac{(\sqrt{1+\alpha\,\beta}-1)}{(\beta+\sqrt{1+\alpha\,\beta}-1)} \right) - \sqrt{1+\alpha\,\beta} + 1 \right] & \text{for } r > 1, \end{cases} \tag{2.73}$$

with the dimensionless sampling time $\alpha = T/\tau_{\text{D}}$ and $\beta = r^{-2} = r_0^2 / z_0^2$. Putting equation 2.69, 2.70 and 2.73 into equation 2.68 yields the sampling time-dependent Q parameter.

$$Q_{3\text{DG}}(T) = \gamma_2\, \mu_0\, T\, \Gamma_{\text{diff,3DG}}(T) \tag{2.74}$$

The above expression for the Q parameter depends solely on the single-molecule brightness rate μ_0 and the mean diffusion time τ_{D} for a given geometric parameter r. The latter represents an instrument constant determined by calibration with a dye of known concentration and diffusion coefficients. Figure 2.14 shows on the left side the graphs of equation 2.74 for varying parameters. By dividing equation 2.74 by the sampling time T, we display the Q parameter as a rate, called the mean single-molecule rate (mSMR).

$$\mu(T) = \frac{Q(T)}{T} = \gamma_2\, \mu_0\, \Gamma_{\text{diff,3DG}} \tag{2.75}$$

This normalization makes the influence of the diffusion time τ_{D} on the graphs directly apparent, which can be inferred from the subplots on the right-hand side. In this presentation, the graphs of the mSMR curves show close resemblance to the sigmoidal shapes of fluorescence correlation spectroscopy (compare this with the curves of the FCS model 2.12). The main difference is that in mSMR the amplitude is a measure of the single-molecule brightness rate instead of the average particle number as in FCS analysis.
The model is suitable for an experimental setup with a single excitation source and a single detection channel. This represents an important benefit compared to the cPCH method, which also combines information from both the time and the amplitude domain, but relies on multiple excitation and detection channels [41].

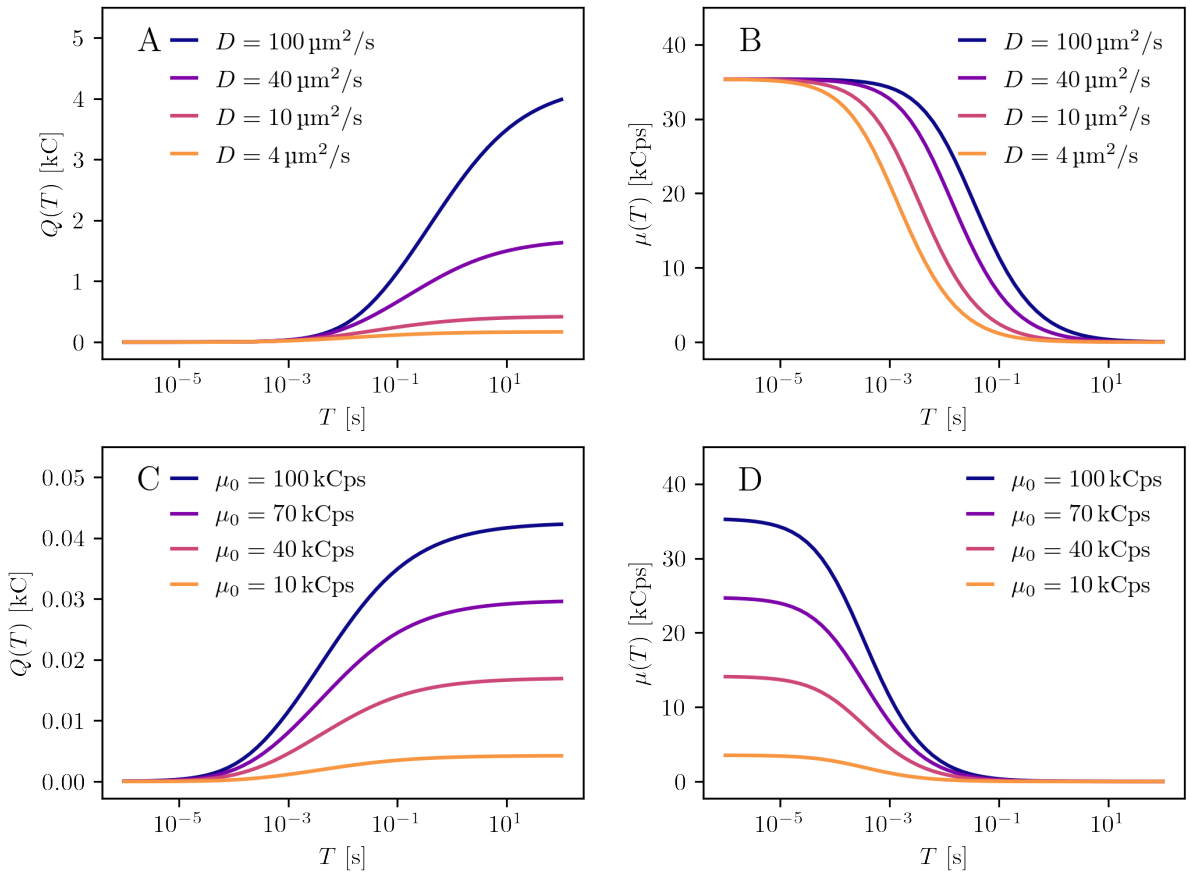

Figure 2.14: The mSMR model for varying parameters. A comparison of equations 2.74 and 2.75 of the mSMR model. The left side shows the sample size dependent Q parameters, and the right side shows the normalized Q parameter μ. The curve shapes of the normalized Q parameter reveal a strong similarity to the autocorrelation curves of the FCS (see 2.12). **A** and **B** Characteristic curves for varying diffusion coefficients D. **C** and **D** Characteristic curves for varying single-molecule brightness rates μ_0.

2.4.2 Photokinetic effects in the mSMR

In the following, photokinetic effects will be considered for the mSMR model. As with FCS, triplet states and isomerization effects are envisaged in more detail.

Triplet states of the mSMR

Like for FCS analysis singlet to triplet transitions of the fluorophores must be considered for small sampling times. Again, since triplet transitions and diffusive behavior occur on different time scales, the systems are considered decoupled. For the mSMR, we can therefore handle the triplet term $g_{\text{trip}}(\tau)$, already known from FCS (see section 2.3.2), in the same way as the diffusive term $g_{\text{diff}}(\tau)$ by inserting it into the integral of the dimensionless binning function (equation 2.71) and subsequently integrating over the sampling time [39, p. 2860]:

$$\begin{aligned}\Gamma_{\text{trip}}(T) &= \frac{2}{T^2}\int_0^T (T-\tau)\, g_{\text{trip}}(\tau)\,\mathrm{d}\tau \\ &= 1 + \frac{2}{T^2}\frac{F_{\text{trip}}\tau_{\text{trip}}T - (1-\exp^{-\frac{T}{\tau_{\text{trip}}}})F_{\text{trip}}\tau_{\text{trip}}^2)}{(1-F_{\text{trip}})}.\end{aligned} \tag{2.76}$$

This results in the entire expression for the sampling time-dependent Q parameter:

$$Q(T) = \gamma_2 \, \mu_0 \, T \, \Gamma_{\text{diff}}(T) \, \Gamma_{\text{trip}}(T), \tag{2.77}$$

and accordingly for $\mu(T)$, we get by normalization to the sampling time:

$$\mu(T) = \gamma_2 \, \mu_0 \, \Gamma_{\text{diff}}(T) \, \Gamma_{\text{trip}}(T). \tag{2.78}$$

Isomerization effects in the mSMR

As already seen in section 2.3.2, the simple isomerization model represented by an on/off system and the triplet state model are identical. Thus, equation 2.53 is simply inserted into the binning integral 2.71. By solving this integral, we obtain the following expression for the simple on/off isomerization model:

$$\begin{aligned} \Gamma_{\text{iso}}(T) &= \frac{2}{T^2} \int_0^T (T - \tau) \, g_{\text{iso}}(\tau) \, \mathrm{d}\tau \\ &= 1 + \frac{2}{T^2} \frac{F_{\text{iso}} \tau_{\text{iso}} T - (1 - \exp^{-\frac{T}{\tau_{\text{iso}}}}) F_{\text{iso}} \tau_{\text{iso}}^2)}{(1 - F_{\text{iso}})}. \end{aligned} \tag{2.79}$$

This yields for the time-dependent Q parameter the following overall expression:

$$Q(T) = \gamma_2 \, \mu_0 \, T \, \Gamma_{\text{diff}}(T) \, \Gamma_{\text{iso}}(T), \tag{2.80}$$

and finally by normalizing to the sampling time, the mSMR model $\mu(T)$ with isomerization term is obtained:

$$\mu(T) = \gamma_2 \, \mu_0 \, \Gamma_{\text{diff}}(T) \, \Gamma_{\text{iso}}(T). \tag{2.81}$$

This simplified model allows a mathematical representation in a closed form, whereas more complex isomerization models can only be solved numerically.

After taking a closer look at the theory behind FCS and mSMR, common noise sources, which generally affect the results of FFS analyses, are considered.

2.5 Noise sources in FFS experiments

FFS experiments involve high-precision and correspondingly sensitive measurement systems. The measurement setups and components used are not free of errors and can thus influence the results of the analysis. In addition, further sources of noise occur which are in the nature of the measurement method and cannot be eliminated by further technical effort. The most common sources of noise are discussed below.

2.5.1 Detector artefacts

The breakthrough for fluorescence fluctuation examinations came in the 1990s with the advent of highly sensitive detectors. These so-called avalanche photon diodes use the photoelectric effect to trigger an electron avalanche and thus amplify the measurement signal inside. Detectors operated above the breakdown voltage can detect individual photon events. They are therefore also referred to as single-photon avalanche diodes

(SPAD). Although modern photodiodes have made fluorescence fluctuation analyses on the single-molecule level possible due to major improvements, the detection of single-molecule events is less a question of sensitive detection than of background noise [47, p. 21]. Common noise sources are detector artefacts such as afterpulsing and detector dead time and to a small extend shot noise. The noise sources are presented in more detail in the following sections.

Afterpulsing

Each time a signal is triggered at the photon detector of the SPAD, there is a certain chance that another spurious event will be induced, which is called afterpulsing. The reason for this behavior of avalanche photodiotes is due to the way the diodes work. An incident photon causes a chain of ionizations in the detector, resulting in a breakdown pulse at the detector output. Occasionally, some of the generated charge carriers are temporarily retained in the junction depletion layer and later released by thermal excitation. This can give rise to free charge carriers resulting in a pulse correlated to the initial event [85, p. 2]. The probability for an afterpulsing event decreases rapidly with time and is specific for the detector [82, p. 3536]. Typical afterpulsing probabilities are in the order of 1 % and have a nano- to microsecond delay to the previous signal [86, p. 3]. An afterpulsing event can cause further events, which are then referred to as second, third etc. order afterpulsing [24, p. 1886]. In fluorescence correlation spectroscopy afterpulsing shows a strong signal increase at small τ ($<1 \times 10^{-6}$ s). Since for most of the molecules studied the diffusion events take place on larger time scales, afterpulsing is only a minor problem for FCS. However, on Mandel's Q parameter the afterpulsing has a broadening effect [87, p. 2457] and should therefore be considered for the analysis of single-molecule brightness.
The easiest way to eliminate afterpulsing is to install a beam splitter and to detect the photons via two channels. Since afterpulsing is only correlated within the signal trace of one detector, it can be completely eliminated by cross-correlation across both detector channels.

Dead time

After each triggered electron avalanche, a SPAD needs a short time to return to its original state, which is called detector dead time. During this time interval of typically some tens to hundreds of nanoseconds, no further photon events can be detected and the detector is blind for a short time [24, p. 1886]. This effect has a decreasing impact on Mandel's Q parameter, such that the measured Q parameter is lower than the true value [87, p. 2457]. To minimize the influence of the detector dead time, the signal intensity should be kept low to operate the detector at low count rates (i.e., low concentration and/or low excitation power).

2.5.2 Other noise sources in FFS experiments

Besides the already presented detector artefacts, there are several other noise sources that influence FFS experiments.

Fluorescence impurities

The fluorescence of contaminants is often caused by biological sample matrices. FFS experiments require high standards for the purity of the samples. Great care must therefore be taken in the composition and processing of the samples to be measured. Thorough cleaning of the measuring equipment is therefore also a prerequisite for reliable FFS measurements.

Scattered light

The occurrence of scattered light depends on the laser power used and is directly proportional to it. Scattered light has two different mechanisms, elastic scattering (*Rayleigh scattering*) and inelastic scattering (*Raman scattering*). Elastic scattering includes reflec-

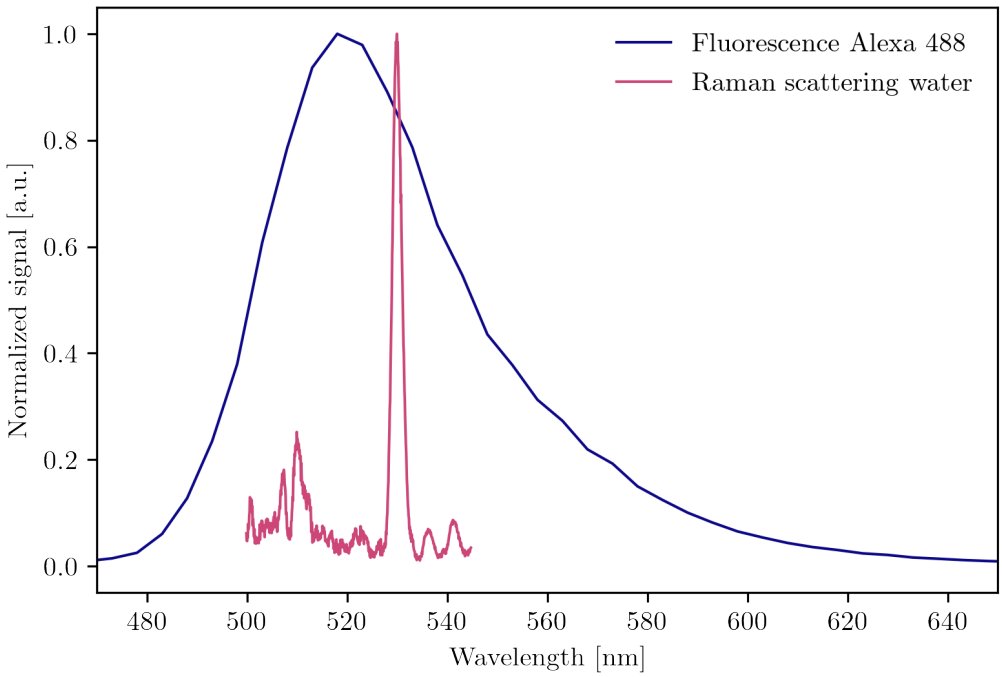

Figure 2.15: Fluorescence emission spectrum of Alexa Fluor 488 and Raman scattering of water. The Raman spectrum was recorded at a wavelength of 532 nm and corrected to 488 nm. For better comparability, the spectra were normalized to unity. In fact, the probability to observe fluorescence photons is several orders of magnitude higher compared to Raman scattering.

tions from excitation light and scattering from the object slide. Due to the Stokes shift in fluorescence for the dyes used, Rayleigh scattering can be suppressed by suitable band filters in the optics. In contrast, inelastic Raman scattering on water molecules has a similar wavelength as the emission spectra of commonly used fluorescence dyes and cannot be distinguished from fluorescence photons by optical filters [47, p. 21-22]. Figure 2.15 shows the fluorescence spectrum of Alexa Fluor 488 and the Raman scattering of water. The Raman scattering was recorded at a wavelength of 532 nm and corrected to 488 nm. The

spectra were normalized to unity. With a common filter set of 535/50 for the recording of Alexa Fluor 488 measurements, the peak of Raman scattering is located exactly in this area. Even though the Raman signal is orders of magnitude lower than the fluorescence signal, Raman scattering introduces another noise term into the measurement. The most efficient method to minimize Raman scattering is to realize a small observation volume. Since there are fewer water molecules in a small volume, the amount of Raman scattering also decreases. In addition, the excitation intensities in the experiment should be kept as low as possible.

Shot noise, white noise, Gaussian noise

The cause of shot noise is the discrete nature of light and electric current and is described by a Poisson process.

$$\mathrm{Poi}(\langle b\rangle, k) = \frac{\langle b\rangle^k}{k!} e^{-\langle b\rangle} \tag{2.82}$$

$\mathrm{Poi}(\langle b\rangle, k)$ returns the probability of observing k noise photons for a given mean noise fraction of $\langle b\rangle$ in the measurement. Shot noise becomes relevant when the finite number of particles carrying energy becomes sufficiently small. This is the case with the detection of photons in FFS experiments.

Uncorrelated noise generally leads to a reduction in amplitude in FCS and mSMR. This means that in FCS the mean number of particles in the observation volume is overestimated and in mSMR the single-molecule brightness rate is underestimated. Therefore, appropriate actions must be taken to suppress the noise influence on the experiments and to correct the remaining noise.

3 Methods and instrumentation

After gaining insight into the theoretical concepts and models relevant for this thesis, the methods and instruments for the practical implementation of fluorescence fluctuation experiments are envisaged. First, the Monte Carlo method to generate fluorescence fluctuations under well-defined conditions is introduced. Then, our home-built confocal measurement system is presented, which is a plate reader that automatically scans the wells of a microtiter plate and acquires the fluorescence fluctuations of the studied samples. Finally, the processing of the fluctuation data is demonstrated including the efficient calculation of the FCS and the mSMR from a fluorescence trace, the correction of measurement artefacts as well as the data fitting using non-linear regression.

3.1 Monte Carlo simulation

The Monte Carlo method is a powerful tool for the simulation of fluorescence fluctuations. As seen in section 2.2.5, the diffusive motion of particles can be realized as a random walk, and since the emission of photons can be modeled by a Poisson process depending on the local excitation intensity, the Monte Carlo method represents thanks to its probability-based approach the appropriate tool for a description of these processes. The method has been presented in Sparrenberg et al. [24, p. 1887]. For the realization of the simulation, a cuboid volume is first defined. The side lengths correspond to 12× the length of the axial and lateral expansions (z_0 and r_0) of the confocal observation volume. The lattice constant ϵ is set to 20 nm. To ensure the validity of the Wiener process for describing a random walk for diffusing species, the time slices Δt of the simulation are given by the diffusion coefficient D of the fastest diffusing species in a simulation run. Through the mean squared displacement of diffusion (see section 2.2.5), the time slice is given for a three-dimensional system as follows:

$$\Delta t = \frac{\epsilon^2}{6D}. \tag{3.1}$$

For each time slice, a random generator decides in which of the 6 possible spatial directions a particle moves. The mean squared displacement of each particle is determined by its diffusion coefficient D and the time slice Δt. A Gaussian profile is used for the molecular detection efficiency profile (see equation 2.63). For convenience, all optical properties of the simulated particles (e.g. quantum efficiency, effective cross section and excitation intensity) are summarized in the factor ϕ_0. Thus, we have for the local photon count rate

$$\phi(\mathbf{r}) = \phi_0 \overline{PSF}(\mathbf{r}). \tag{3.2}$$

The number of photons detected from an immobilized particle under constant excitation conditions is given by a Poisson distribution [36, p. 556].

$$\mathrm{Poi}(\phi(\mathbf{r}), k) = \frac{(\phi(\mathbf{r}))^k}{k!} e^{-\phi(\mathbf{r})}. \tag{3.3}$$

The Poisson distribution in this form returns for each simulated particle at location **r** the probability of detecting k photons. The location of each particle is then updated for each time slice by a random motion in x, y or z direction and the associated probabilities to detect k photons are calculated and summed over all simulated particles. The working principle of the Monte Carlo simulation is shown in figure 3.1. In the center of the

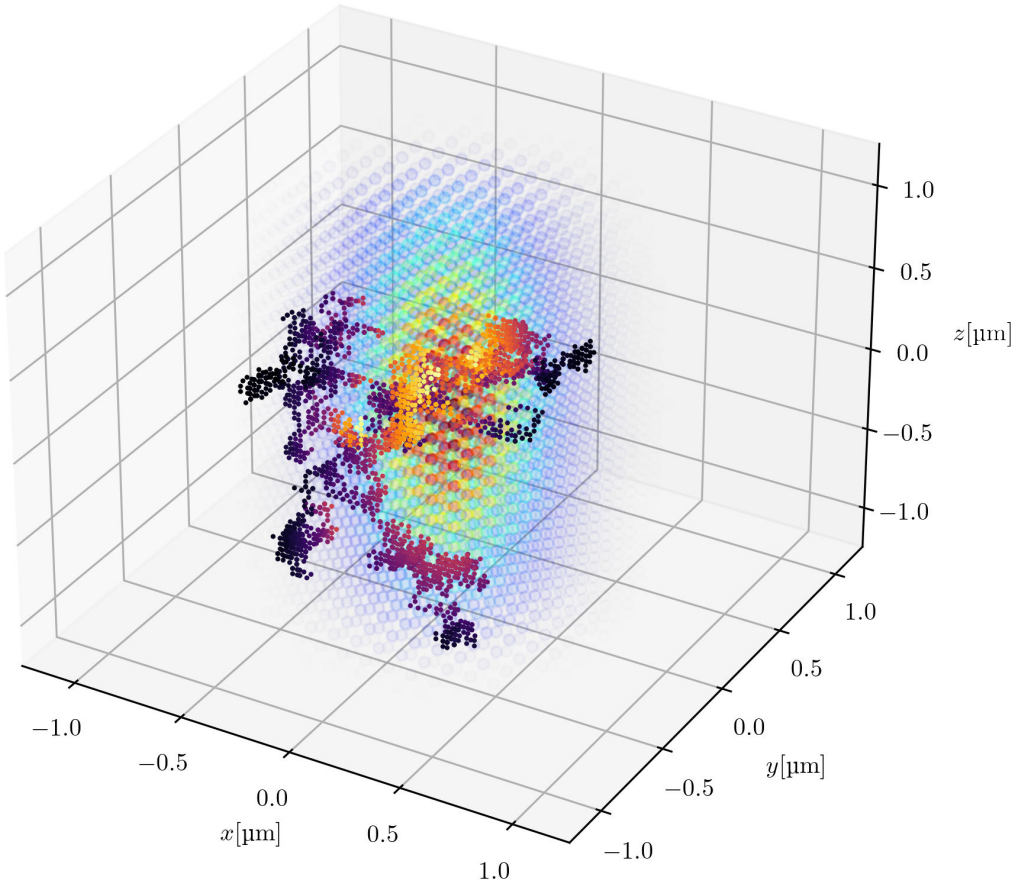

Figure 3.1: The working principle of the Monte Carlo simulation. The diffusion of $n = 3$ particles is modeled by a random walk. The excitation is position dependent and determines the molecule's probability of emitting a photon.

graph, the molecular detection efficiency, modeled by a Gaussian ellipsoid, is shown as an intensity profile. It represents the convolution of the excitation profile and confocal optics. The diffusion of n particles is modeled by a random walk. Whenever a particle comes close to the Gaussian ellipsoid, the probability of emitting k photons increases as a function of the local intensity. The emission probability is highlighted in color. The number of emitted photons of all particles in a time slice is summed up and constitutes the fluorescence trace of the simulation. The fluorescence trace is then evaluated in the same way as the measured fluorescence trace of an experiment. Our simulation also allows the modeling of detector artefacts beyond the simple study of diffusion. Thus, afterpulsing and detector dead time can be simulated. It is also possible to superimpose Poissonian noise to model background noise.

3.2 The confocal plate reader

The measurement system is a home-built confocal plate reader which has been developed by our group. Being a fully functional confocal microscope integrated into a benchtop system, the plate reader automatically scans microtiter plates with transparent bottoms and records the fluorescence fluctuations of the examined sample. The author was substantially involved in the development of the plate reader. We were motivated by the circumstance that FFS systems involve high investment costs and at the same time require great technical understanding as well as a lot of manual labor for the measurement. By the realization of a confocal microscope as a plate reader, we intend to facilitate the implementation and conduction of FFS experiments. The plate reader and the data processing has been presented in Sparrenberg et al. [24, p. 1887-1889].

3.2.1 Instrumentation

The confocal plate reader consists of essentially the same components as commercially available confocal microscope used to record fluorescence fluctuations. Figure 3.2 shows a schematic illustration of the measurement system. A laser (488 nm, Laser2000, France) serves as excitation source and is coupled into the system via a fiber. The laser beam exits the fiber via a collimator and is attenuated by a neutral filter (not shown). This has several reasons. Firstly, only a few µW of laser power are required for excitation. Thus, to use the full dynamic range of the laser control, the beam must be attenuated. Measurements have also shown that when the laser beam is coupled directly into the optical system, mode fluctuations occur that are presumably caused by reflected light. This effect can be eliminated by installing the neutral filter in a tilted position.

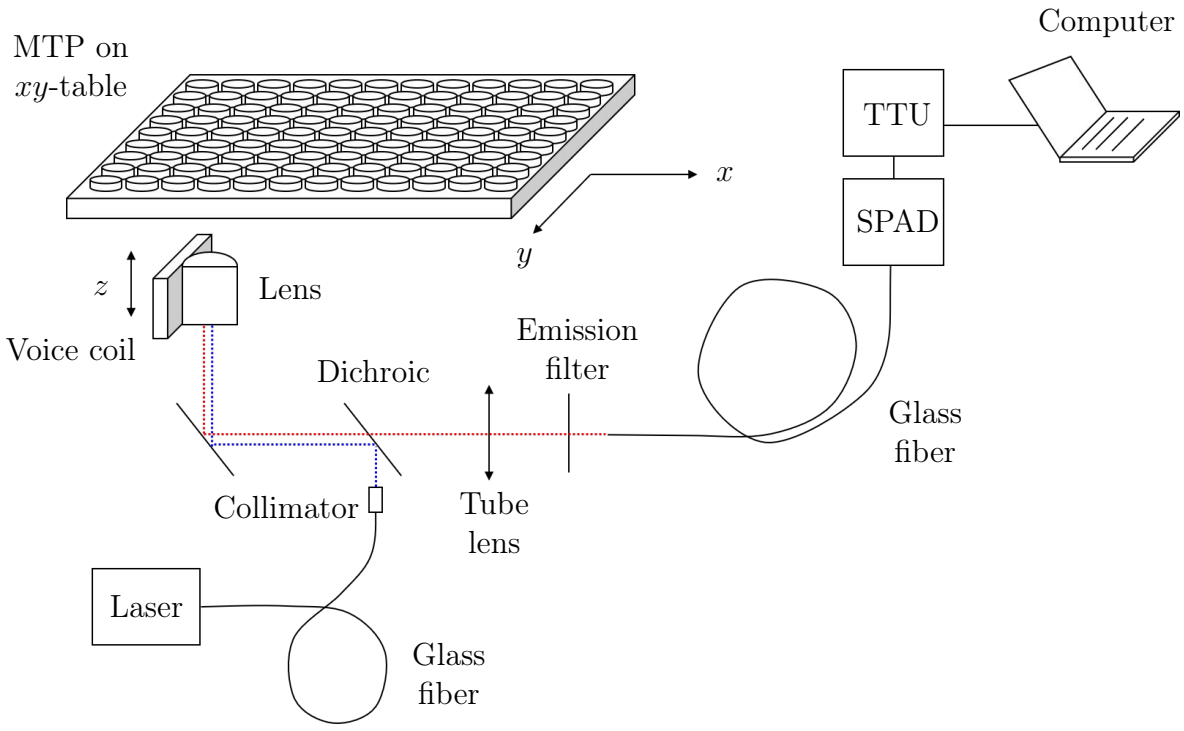

Figure 3.2: Schematic of the confocal plate reader for the automated measurement in a microtiter plate. The excitation laser beam is shown in blue, the collected emission light in red. Reproduced from [24, p. 1888].

A dichroic mirror (LP500) serves as a bandstop filter. The laser beam is initially reflected by the mirror and directed into a microscope objective (Neofluar, 63x, LD, NA = 0.75, Zeiss, Germany). The objective focuses the beam through the transparent bottom of a microtiter plate onto the sample. Theoretically, the objective lens corrects plate bottoms thicker than 1 mm via a correction ring. However, pre-tests have shown that it is advantageous if the transparent bottom is as thin as possible (approximately 140 µm). Suitable materials are glass and polystyrene, whereas other materials such as cyclic olefin copolymer (COC) could not convince. Fluorophores in the well of the microtiter plate start emitting photons. Parts of the emitted fluorescence photons are collected by the objective and due to the Stoks shift can now pass through the dicroitic mirror. A tube lens (160 mm) focuses the parallel light from the measurement onto the optical fiber of the detector. An emission filter (535/50) between the tube lens and the fiber blocks remaining residual excitation light from progressing. The remaining measurement signal is then transmitted via an optical fiber (50 µm, Thorlabs, Germany) to a photodiode (PDM, Micro Photon Devices, Italy). Due to its small diameter, the fiber also serves as a pinhole to realize the confocal setup. A time tagger card (Time Tagger 20, Swabian Instruments, Germany) processes the outgoing TTL signal of the photodiode. The time tagger card assigns a time stamp to each TTL signal of the detector. The data annotated in this way contain many zero entries and can therefore be saved very well via a sparse matrix to save memory. The calculation of the FCS and the mSMR is done externally on the computer. Very efficient methods can be used for the calculation, which are presented in section 3.3.

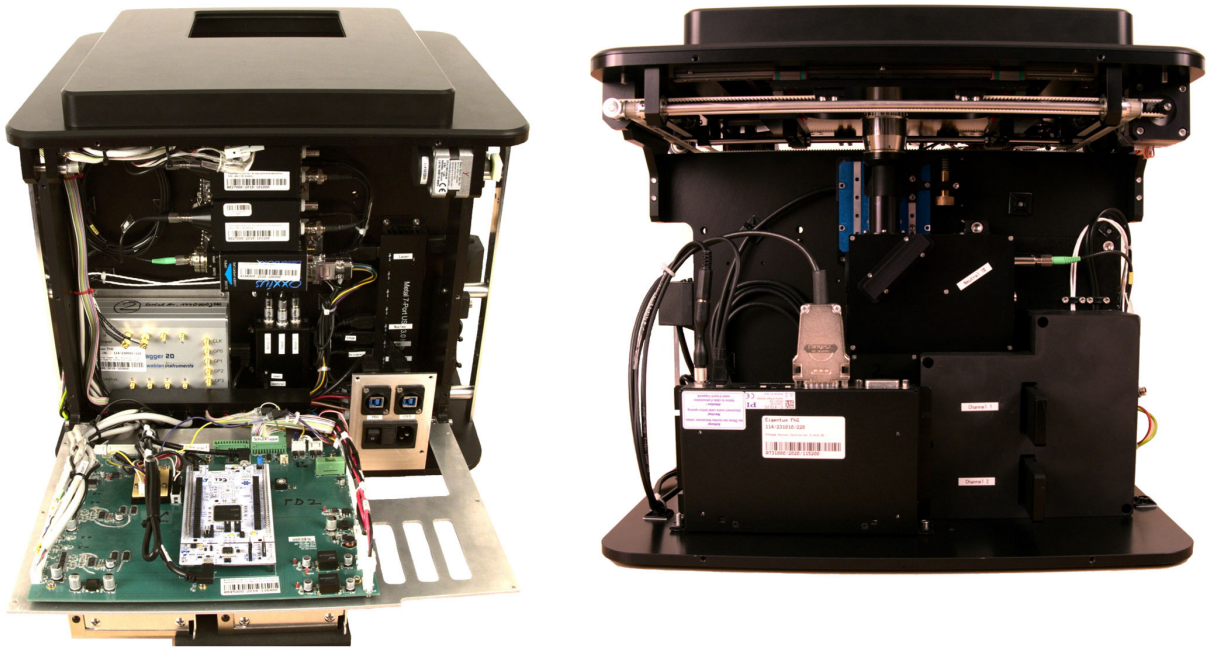

Figure 3.3: Rear and front view of the home-built confocal plate reader. All components are integrated in a handy benchtop device. The outer shielding was dismantled for the photo shoot. **Left:** View of the opened back side with the photodiodes, the excitation laser, the time tagger card, and the PCI board with the microcontroller for controlling the components. **Right:** View of the microscope objective lens and the z-drive as well as the associated controller. The optical channels are shielded from incident ambient light. Neutral density filters, emission filters and dichroic can be exchanged via slide-in modules.

An essential difference to ordinary confocal microscopes is, besides the use of a long-distance objective lens, which is discussed in the next paragraph, the realization as a plate reader. The scanning of the microtiter plate is automated. An xy-table developed

according to our specifications (Jüke, Germany) moves along the specified wells of the plate. At each well, an autofocus (section 3.2.2) finds the correct z-plane for the measurement. For this task, a voice coil drive (PI, Germany) moves the objective lens in the z-direction step by step and to find the optimal measurement height. Then 5 measuring positions in the well are moved in succession and the measurement is carried out. To obtain the most accurate measurements possible, all optical components in the measuring system are shielded from the outside to prevent ambient light from entering. The control of the hardware components is also handled by a self-written software. This software also provides a clear interface for planning the measurement routines, monitoring the measurement results, and visualizing the measurement data.

In the following, the long-distance objective lens (Neofluar, 63x, LD, NA = 0.75, Zeiss, Germany) used in our setup will be briefly discussed. Usually, high aperture immersion lenses are used for FFS experiments to collect as many photons as possible. However, because of automation, the use of a long-distance air lens is much more appropriate. On the one hand, the air objective allows scanning a microtiter plate well by well without having to find technically complex solutions for immersion microscopy. On the other hand, long distance objectives are suitable for measurements through the transparent bottom of the microtiter plate since these objectives allow a flexible coverslip correction and can thus be optimized for the used plate type. To estimate how much signal is lost, a comparative calculation for a typical oil immersion objective lens and the used long-distance objective lens will be presented in the following. The term $\frac{RA}{R\Omega}$ is the proportion of a luminous sphere surface that can be imaged through the lens and is given by the following expression:

$$\frac{RA}{R\Omega} = \frac{\int_0^{\theta}\int_0^{2\pi} r^2 \sin(\theta)\,\mathrm{d}\phi\,\mathrm{d}\theta}{4\pi r^2} = \frac{1-\cos(\theta)}{2}. \tag{3.4}$$

To express equation 3.4 in terms of the numerical aperture, we convert the definition of $NA = n\sin(\theta)$ to $\theta = \arcsin(\frac{NA}{n})$ and insert it into equation 3.4, which gives

$$\frac{RA}{R\Omega} = \frac{1-\cos(\arcsin(\frac{NA}{n})}{2}. \tag{3.5}$$

A typical oil immersion lens for confocal microscopy has a numerical aperture of $NA = 1.4$ and a refractive index for the employed oil of $n = 1.518$ which calculates as $\frac{RA}{R\Omega} = 0.307$. For our setup we get for $NA = 0.75$ and $n = 1.0$ a sphere coverage of $\frac{RA}{R\Omega} = 0.169$. This means we capture 55.2 % of the emitted photons that the high aperture immersion objective would capture, which is justifiable. In addition, the use of a long-distance lens has already been demonstrated in other work to analyze fluorescence fluctuations [54].

3.2.2 Autofocus and well offset

For technical reasons, the plate reader performs the measurements through the bottom of the microtiter plate. However, microtiter plates have a curvature of the plate bottom due to the manufacturing process. Additionally, the position of the microtiter plate can be shifted by a few micrometers when inserted into the system. Thus, the exact orientation of the plate is not known at the start of the measurement and high-precision measurements cannot be ensured. To solve this problem, the plate reader features an autofocus. Before each measurement in a new well, the objective lens is moved in z-direction in 2 µm steps.

At each step, the laser intensity of the scattered light is measured. When reaching the bottom side of the plate, part of the laser light is reflected into the measuring system giving a clear intensity peak. The software detects this peak and moves the lens to the correct measurement position. The offset between the detected bottom of the plate and the ideal measuring position must be determined once during the first calibration of the system and depends mainly on the material and thickness of the microtiter plate bottom as well as on the exact setting of the correction ring on the objective. The correct measuring position is determined by an optimization procedure. Over a series of FFS measurements, the offset is changed stepwise, and both the fluorescence counts and the results of the FFS analysis are compared (see figure 3.4). The measured values change for

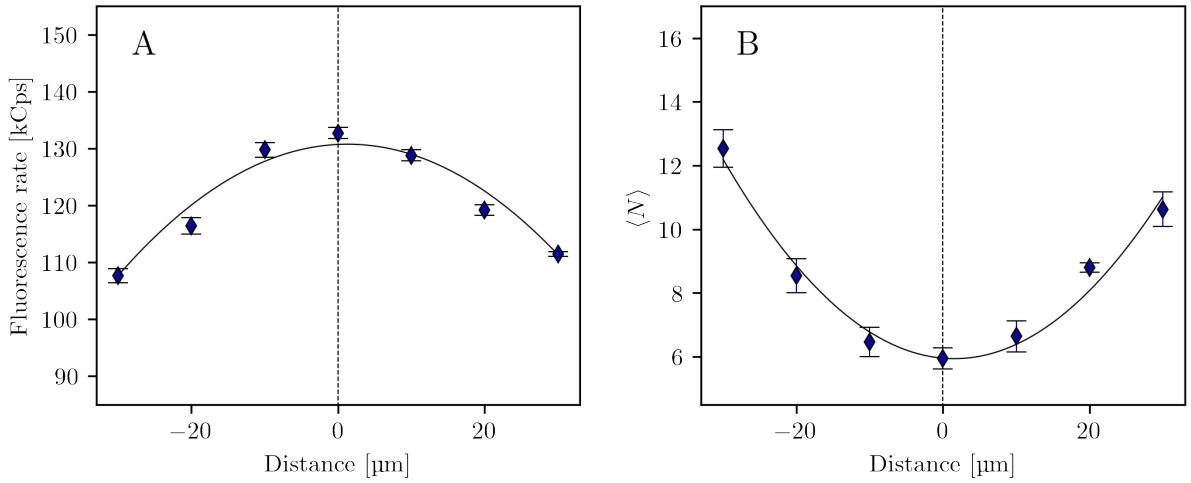

Figure 3.4: The influence of the offset on the measurement results. By varying the offset distance between plate bottom and focal plane step by step, the optimal offset ist found. The measurements are conducted on a 1 nM Alexa Fluor 488 solution.

increasing deviations from the optimal offset. A maximum is formed for the count rates and a minimum for the mean particle count of the FCS analysis. By varying the offset and fitting the fluorescence rates and mean particle counts with a 2nd order polynomial, the optimal offset for an uncalibrated measurement setup is derived.

3.2.3 Influence of temperature

In addition to the exact measurement position, temperature also has an important influence on FFS measurements. From the Stokes Einstein equation 2.33, the influence of temperature on the diffusion coefficient is evident. The temperature appears directly in the nominator and indirectly in the viscosity of the solvent in the denominator. In literature, the diffusion coefficient is usually given for 298.15 K. For measurements in water, the diffusion coefficient can be corrected with $\eta_{298.15\,\mathrm{K}} = 8.9 \times 10^{-4}\,\mathrm{Pas}$ as follows

$$D(T) = D_{298.15\,\mathrm{K}} \frac{T}{298.15\,\mathrm{K}} \frac{\eta_{298.15\,\mathrm{K}}}{\eta(T)}. \tag{3.6}$$

The viscosity of water $\eta(T)$ can be approximated for the entire liquid phase with an error of $< 1\,\%$ via [88, p. 939]

$$\eta(T) = \eta_{293.15\,\mathrm{K}} \times 10^{-\frac{A}{B}} = 1.0016 \times 10^{-3}\,\mathrm{Pas} \times 10^{-\frac{A}{B}} \tag{3.7}$$

with

$$A = 1.37023\,(T - 293.15) + 8.36 \times 10^{-4}\,(T - 293.15)^2,$$
$$B = -146.15 + T.$$

The temperature has a considerable impact on the diffusion coefficient. E.g., Alexa Fluor 488 has a reported diffusion coefficient of $D_{298.15\,\mathrm{K}} = 435\,\mu\mathrm{m}^2/\mathrm{s}$ in water [89, p. 1442]. If a measurement is made at 294.15 K, the diffusion coefficient reduces by about 10 % with $D_{294.15\,\mathrm{K}} = 389\,\mu\mathrm{m}^2/\mathrm{s}$. Therefore, the temperature is tracked for each measurement to correct the derived diffusion coefficients from the analysis if necessary.

3.3 Data processing

After presenting the methods used to collect fluorescence fluctuations, data processing will be addressed. In general, large amounts of data are generated when analyzing FFS experiments. This is because the original data sets must have significantly smaller sampling times than the time intervals required for a molecule to cross the observation volume. In experiments with sufficiently small sampling times ($\leq 1 \times 10^{-6}\,\mathrm{s}$), tens of millions of data points are collected per time series, making the calculation of the models very computation- and storage-intensive. Regarding the storage problem, the concept of sparse matrices can be used for data processing. These are suitable for handling data sets with many zero entries. This prerequisite is given for the data sets at hand. In a sparse matrix, only those entries are stored which contain a non-zero value. Thus, the storage volume can be reduced drastically. Refering to computation, we will introduce efficient algorithms to calculate the FCS and mSMR models from FFS data.

3.3.1 Calculating the autocorrelation for FCS

Probably the most elegant way to calculate the autocorrelation of FCS is using the *Wiener-Khinchin theorem*, since it reduces the computational cost enormously. Via a Fourier transform, the fluorescence trace is transformed into the reciprocal space and can be squared here by a simple multiplication with itself. Through the inverse Fourier transform, the data set is transferred back again, and the calculation is completed. In the following we will go through the necessary calculation steps. According to the Wiener-Khinchin theorem the so-called *power spectral density* (PSD) is related to the autocorrelation by its Fourier transform:

$$S_{xx}(\omega) = \int_{-\infty}^{\infty} r_{xx}(\tau) e^{-i\omega\tau}\,\mathrm{d}\tau, \tag{3.8}$$
$$r_{xx}(\tau) = \frac{1}{2\pi}\int_{-\infty}^{\infty} S_{xx}(\omega) e^{i\omega\tau}\,\mathrm{d}\omega. \tag{3.9}$$

The PDF indicates the strength of signal variations distributed over the frequency, i.e. at which frequencies the variations are strong and at which frequencies they are weak. The PSD is defined as [90, p. 4]:

$$S_{xx}(\omega) = |\hat{x}(\omega)|^2, \tag{3.10}$$

where $\hat{x}(\omega)$ is the Fourier transform of $x(t)$.

$$\hat{x}(\omega) = \int_{-\infty}^{\infty} x(t) e^{-i\omega\tau} \, \mathrm{d}\tau = \mathcal{F}\{x(t)\} \tag{3.11}$$

It follows:

$$r_{xx}(\tau) = \frac{1}{2\pi} \int_{-\infty}^{\infty} S_{xx} e^{i\omega\tau} \, \mathrm{d}\omega = \frac{1}{2\pi} \int_{-\infty}^{\infty} |\hat{x}(\omega)|^2 e^{i\omega\tau} \, \mathrm{d}\omega. \tag{3.12}$$

And in short-hand notation with $\mathcal{F}$ for the Fourier transform and $\mathcal{F}^{-1}$ for the inverse Fourier transform, we get:

$$r_{xx}(\tau) = \mathcal{F}^{-1}\big\{|\mathcal{F}\{x(t)\}|^2\big\}. \tag{3.13}$$

Finally, inserting expression 3.13 into equation 2.42, yields an expression for the normalized autocorrelation function $G(\tau)$ of a continuous intensity trace $I(t)$ based on the Wiener-Khinchin theorem.

$$G(\tau) = \frac{\mathcal{F}^{-1}\big\{|\mathcal{F}\{I(t)\}|^2\big\}}{\langle I(t)\rangle_t^2} - 1 \tag{3.14}$$

So far, the continuous case of the Fourier transform was considered. In real experiments, a finite amount of discrete data occurs and the discrete Fourier transform (DFT) applies. Highly efficient algorithms referred as *fast Fourier transform* (FFT) have been developed, which are contained in common programming libraries. The complexity scales with $\mathcal{O}(N \log(N))$ for time-data series of length N compared to $\mathcal{O}(N^2)$, which means the complexity is linearly constrained [91, p. 27]. Therefore, the Wiener-Khinchin theorem allows a very fast calculation of the FCS of a given time-data sequence.

As a completion, a calculation of fluorescence correlations for higher orders is included in the appendix 10.1. However, this so-called higher order FCS (HOFCS) will not find any further use in the present thesis.

3.3.2 Calculating the mSMR

The concept for calculating the mSMR for a given fluorescence trace is based on repeated binning, which, starting at the original sampling time $T_{\min}$, progressively aggregates the data points to larger sampling times T. The minimum sampling time depends on the experimental setup and the acquisition parameters. The signal trace of length T_{obs} consists of $n = T_{\mathrm{obs}}/T_{\min}$ entries. All integer divisors N_i of n are searched to divide the signal trace into equidistant sampling intervals. We thus obtain the possible sampling times $T_i = T_{\min} N_i$. Binning is implemented using matrix multiplication, which will be illustrated using the integer divisor $N = 4$ as an example. In this case, a signal trace with originally n entries and a sampling time of e.g. $T_{\min} = 1 \times 10^{-6}\,\mathrm{s}$ is aggregated into a signal trace of length $n/4$ and a sampling time of $T = 4 \times 10^{-6}\,\mathrm{s}$. The original fluorescence signal trace is given by:

$$F_{n\times 1} = \begin{bmatrix} a_1 \\ \vdots \\ a_n \end{bmatrix}. \tag{3.15}$$

First, the $n \times 1$ matrix is reshaped into a $n/4 \times 4$ matrix. For clearness, the original indexing of the entries is preserved.

$$F_{\frac{n}{4}\times 4} = \begin{bmatrix} a_1 & a_2 & a_3 & a_4 \\ \vdots & \vdots & \vdots & \vdots \\ a_{n-3} & a_{n-2} & a_{n-1} & a_n \end{bmatrix} \tag{3.16}$$

Then, the matrix is multiplied by a 4×1 all-ones matrix to get a binned $n/4 \times 1$ matrix with a sampling time of $4 \times 10^{-6}\,\mathrm{s}$.

$$F_{\frac{n}{4}\times 1} = F_{\frac{n}{4}\times 4} \times \begin{bmatrix} 1 & 1 & 1 & 1 \end{bmatrix}^{\intercal} = \begin{bmatrix} b_1 \\ \vdots \\ b_{n/4} \end{bmatrix}. \tag{3.17}$$

This process is repeated for all integer divisors of n to calculate the respective binned fluorescence trace for all possible sampling times. For each newly binned fluorescence trace, the associated statistical moments are calculated, yielding them as a function of the sampling time. If the moments are calculated from real measurement data, detector artefacts must be considered. In this case, the required correction of the moments is computed as described in section 3.3.3 via equations 3.30 and 3.30. From the moments, the mean single-molecule rate calculates as follows:

$$\mu(T) = \frac{Q(T)}{T} = \frac{\langle k^2 \rangle_{\mathrm{m}}(T) - \langle k \rangle_{\mathrm{m}}^2(T) - \langle k \rangle_{\mathrm{m}}(T)}{T \langle k \rangle_{\mathrm{m}}(T)}. \tag{3.18}$$

The mSMR data points from the fluorescence trace can then be fitted by an appropriate model to retrieve the physical parameters from the experimental data.

3.3.3 Correction of detector artefacts and background noise

As already seen in section 2.5, several noise sources occur that must be considered in FFS experiments. For a reliable evaluation of the FFS experiments, the impact of these quantities must be minimized. But even the best conditions cannot suppress all noise sources.

Correction of afterpulsing and detector dead time

Since afterpulsing and detector dead time influence the results of the evaluation (see section 2.5.1), a reliable correction of the measurement data is desirable. The easiest way to avoid afterpulsing is to use two detection channels in the measurement setup. Since the afterpulsing between two detectors is completely uncorrelated, afterpulsing can be effectively avoided [85, p. 3]. Detector dead time plays a minor role in FCS because it occurs on nanosecond time scales that are irrelevant to the evaluation [85, p. 2]. However, subsequent correction of detector artefacts after the measurement is difficult in FCS. With the mSMR, however, we can correct the photocounting moments from the experiment. Our goal is a correction term that allows to calculate the ideal moments $\langle k^n \rangle$ from the measured moments $\langle k^n \rangle_{\mathrm{m}}$ of a fluorescence trace.
Considering the *probability density function* (PDF) of the incoming photons k, the dead time affected PDF $P'(k)$ represented by the ideal PDF $P(k)$ and the detector dead time

t_{dead} is sought. The first order correction is given for the dimensionless dead time $\delta = \frac{t_{\mathrm{dead}}}{T}$ by [92, p. 114]:

$$P'(k) = P(k) + \delta\big[k\,(k+1)\,P(k+1) - k\,(k-1)\,P(k)\big] \tag{3.19}$$

An afterpulsing-affected PDF $P^*(k)$ represented by the ideal PDF $P(k)$ and the afterpulsing probability P_A can be found using an algorithm from literature [93]. Assuming only first order afterpulsing events and $P_A \ll 1$, the expression is given by [94, p. 5]

$$P^*(k) = (1 - k\,P_A)\,P(k) + (k-1)\,P_A\,P(k-1). \tag{3.20}$$

The above expressions is a first order correction term, which holds for setups where only occasionally a single incoming photon is not detected due to dead time. Discarding multiphoton events in the same dead time interval is not considered. The same applies to afterpulsing. Theoretically, an afterpulsing event can trigger further afterpulsing events. However, the occurrence of afterpulsing is very rare. Since moderate photon counts are usually encountered, neglecting higher afterpulsing terms is justified. The measured PDF $P_{\mathrm{m}}(k)$ must hold the following conditions.

$$P_{\mathrm{m}}(k) = P'(k) \quad \text{for } P_A = 0, \tag{3.21}$$

$$P_{\mathrm{m}}(k) = P^*(k) \quad \text{for } \delta = 0, \tag{3.22}$$

$$\sum_k P_{\mathrm{m}}(k) = 1. \tag{3.23}$$

These conditions are satisfied by the following expression:

$$P_{\mathrm{m}}(k) = P'(k) + P^*(k) - P(k). \tag{3.24}$$

Insert equation 3.19 and equation 3.20 into the above expression gives [94, p. 6]:

$$\begin{aligned} P_{\mathrm{m}}(k) =& P(k) + \delta\big[k\,(k+1)\,P(k+1) - k\,(k-1)\,P(k)\big] \\ &+ (k-1)\,P_A\,P(k-1) - k\,P_A\,P(k). \end{aligned} \tag{3.25}$$

The corrected photon-counting moments $\langle k^n \rangle$ can be obtained from the measured photon counting moments $\langle k^n \rangle_{\mathrm{m}}$ by inverting equation 3.26. If $\delta \ll 1$ and $P_A \ll 1$ holds, we can make the following approximation:

$$\begin{aligned} P(k) &\approx P_{\mathrm{m}}(k) + \delta\big[k\,(k+1)\,P_{\mathrm{m}}(k+1) - k\,(k-1)\,P_{\mathrm{m}}(k)\big] \\ &\quad + (k-1)\,P_A\,P_{\mathrm{m}}(k-1) - k\,P_A\,P_{\mathrm{m}}(k), \\ &= P_{\mathrm{m}}(k) - P'_{\mathrm{m}}(k) - P^*_{\mathrm{m}}(k) \end{aligned} \tag{3.26}$$

with

$$P'_{\mathrm{m}}(k) = \delta\big[k(k+1)P_{\mathrm{m}}(k+1) - k(k-1)P_{\mathrm{m}}(k)\big], \tag{3.27}$$

$$P^*_{\mathrm{m}}(k) = (k-1)P_A P_{\mathrm{m}}(k) - kP_A P_{\mathrm{m}}(k). \tag{3.28}$$

Using the definition of the moments of a distribution, we get:

$$\begin{aligned} \langle k^n \rangle &= \sum_{k=0}^{\infty} k^n P(k) = \sum_{k=0}^{\infty} k^n \big(P_{\mathrm{m}}(k) - P'_{\mathrm{m}}(k) - P^*_{\mathrm{m}}(k)\big) \\ &= \langle k^n \rangle_{\mathrm{m}} - \langle (k')^n \rangle_{\mathrm{m}} - \langle (k^*)^n \rangle_{\mathrm{m}}. \end{aligned} \tag{3.29}$$

Now, the first two corrected moments $\langle k \rangle$ and $\langle k^2 \rangle$ are obtained by inserting the definitions 3.27 and 3.28 into equation 3.29 and solving for $n = 1$ and $n = 2$. The solution reads [94, p. 6]:

$$\langle k \rangle = \langle k \rangle_{\mathrm{m}}(1 - P_A - \delta) + \delta \langle k^2 \rangle_{\mathrm{m}}, \tag{3.30}$$

$$\langle k^2 \rangle = \langle k^2 \rangle_{\mathrm{m}}(1 - 2P_A - 3\delta) + 2\delta \langle k^3 \rangle_{\mathrm{m}} + (\delta - P_A)\langle k \rangle_{\mathrm{m}}. \tag{3.31}$$

Because of $\delta = \frac{t_{\mathrm{dead}}}{T}$, the above expression represents a function of the sampling time T and is therefore suitable without further adjustment for the correction of the sampling time-dependent moments as used in the mSMR. The correction terms are valid only for $\langle k \rangle \, \delta \ll 1$ [81, p. 1951]. Since the product of $\langle k \rangle \, \delta$ is constant for all sampling times and the detector dead time is given by the apparatus, the only adjustment screw is the mean count rate, which can be reduced experimentally most easily by low analyte concentrations and low excitation powers.

One final note for the implementation of the correction, for large sampling times, very large numerical values can result during the calculation of the correction. This can lead to problems when analyzing measurements with high count rates. When implementing the correction, therefore, care must be taken to ensure that the number types are sufficiently large. It is recommended to use float64 types to prevent a possible integer overflow.

3.3.4 Correction of uncorrelated background noise in FFS experiments

Already during the design of the measurement setup and the experiments, the influence of noise must be considered (see section 2.5.2). Selecting suitable filter sets minimizes the influence of scattered light, especially Rayleigh scattering from the excitation. The, shielding the measurement system blocks ambient light, while detector coooling suppresses white noise from the electronics. These steps significantly reduce the noise ratio in a measurement. The remaining uncorrelated background noise, however, influences the amplitude of FFS experiments and thus leads to an overestimation of the mean particle count in FCS analysis and to an underestimation of the single-molecule brightness rate in the mSMR analysis. Figure 3.5 shows this effect. At small concentrations, the S/N ratio becomes less favorable and thus the effect on the parameters more pronounced. This effect can be minimized using the background noise $\langle b \rangle$ and the fluorescence rate of a measurement $\langle k \rangle_{\mathrm{m}}$ to calculate a correction term [76, p. 1943-1944][58, p. 2304]. For FCS analysis this term is given by

$$\frac{1}{\chi^2} = \frac{1}{(1 + \frac{\langle b \rangle}{\langle k \rangle_{\mathrm{m}} - \langle b \rangle})^2}. \tag{3.32}$$

The actual corrected particle number in the observation volume is obtained using the following relation.

$$\langle N \rangle_{\mathrm{corr}} = \langle N \rangle \frac{1}{\chi^2} \tag{3.33}$$

In addition to the posterior correction of the mean particle numbers, the FCS curve can also be corrected directly. The following applies here:

$$G_{\mathrm{corr}}(\tau) = \frac{1}{\langle N \rangle} g_{\mathrm{diff}} \, \chi^2. \tag{3.34}$$

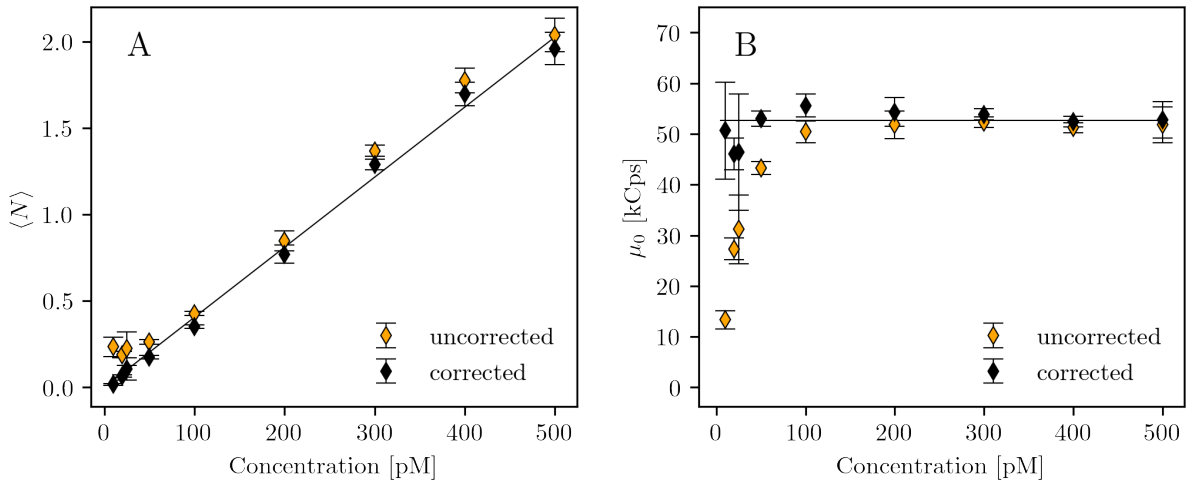

Figure 3.5: The influence of background noise on the mean particle number and the single-molecule brightness rate. The FCS and mSMR data are retrieved from fluorescence fluctuations of an Alexa Fluor 488 dilution series. **A** Uncorrected and corrected mean particle number $\langle N \rangle$ from FCS analysis. **B** Uncorrected and corrected single-molecule brightness rate μ_0 from mSMR analysis.

Analogous to the correction of the mean number of particles $\langle N \rangle$, the single molecular brightness rate μ of mSMR experiments can be corrected. In theory the following relationship applies:

$$\mu_0 = \frac{\langle k \rangle}{\langle N \rangle}. \tag{3.35}$$

In the experiment, however, the measured fluorescence counts are superimposed by background noise $\langle k \rangle_\mathrm{m} = \langle k \rangle + \langle b \rangle$. With this consideration, we adapt equation 3.33 as follows

$$\begin{aligned} \mu_{0,\mathrm{corr}} &= \frac{\langle k \rangle_\mathrm{m} - \langle b \rangle}{\langle N \rangle_\mathrm{corr}} = \frac{\langle k \rangle_\mathrm{m} - \langle b \rangle}{\langle N \rangle} \chi^2 \\ &= \left(1 - \frac{\langle b \rangle}{\langle k \rangle_\mathrm{m}}\right)^{-1} \mu_0. \end{aligned} \tag{3.36}$$

Equation 3.36 effectively corrects μ_0. As for FCS, it is also possible to correct the mSMR data points directly using

$$\mu_\mathrm{corr}(T) = \gamma_2 \, \mu_0 \, \Gamma_\mathrm{diff} \left(1 - \frac{\langle b \rangle}{\langle k \rangle_\mathrm{m}}\right)^{-1}. \tag{3.37}$$

The effect of the correction routine is also shown in figure 3.5. Using the background noise obtained from a blank measurement, the mean particle numbers $\langle N \rangle$ can be brought into a linear relationship. Also, the single-molecule brightness rates μ_0 can be corrected to be almost constant over all concentration steps.

3.4 Data fitting

Fitting a model correctly to the measured data is a critical step for analysis. If the model can be represented in the following form, linear regression applies for analysis.

$$y_i = \beta_0 + \beta_1 f_1(x_i) + \cdots + \beta_p f_p(x_i) + \epsilon_i, \qquad i = 1, \ldots, n, \tag{3.38}$$

whereas y_i is the dependent variable and $f_i(x_i)$ are the regressors. The error variable ϵ_i adds noise to the linear system of dependent variable and regressors. Some of the regressors $f_i(x_i)$ can be non-linear functions, which is the case for a polynomial fit. In linear regression, there is a closed-form solution for the regression coefficients β_j with $j = 0, 1, \ldots, p$, which is derived via the least squares method and can be found in statistic literature (e.g., [95, p. 311-338]). The ordinary least square method aims to minimize the following term:

$$Q(\beta_0, \ldots, \beta_p) = \sum_{i=1}^{n} \epsilon_i^2 = \sum_{i=1}^{n} (y_i - \hat{y}_i)^2, \tag{3.39}$$

with $\hat{y}_i$ being the empirical regression function and ϵ_i is given by $\epsilon_i = y_i - \hat{y}_i$. For the minimum applies the necessary condition

$$\frac{\partial Q(\beta_0, \beta_1, \ldots, \beta_p)}{\partial \beta_i} = 0, \qquad j = 0, 1, \ldots, p, \tag{3.40}$$

The solution of this problem is in matrix notation:

$$\hat{\boldsymbol{\beta}} = (\mathbf{X}^\intercal \mathbf{X})^{-1} \mathbf{X}^\intercal \mathbf{y}. \tag{3.41}$$

with the following vectors and matrices for the n data points:

$$\mathbf{X} = \begin{pmatrix} 1 & f_1(x_1) & \ldots & f_p(x_1) \\ 1 & f_1(x_2) & \ldots & f_p(x_2) \\ \vdots & \vdots & \ddots & \vdots \\ 1 & f_1(x_n) & \ldots & f_p(x_n) \end{pmatrix}, \tag{3.42}$$

$$\mathbf{y} = \begin{pmatrix} y_1 \\ \vdots \\ y_n \end{pmatrix}, \hat{\boldsymbol{\beta}} = \begin{pmatrix} \hat{\beta}_0 \\ \vdots \\ \hat{\beta}_p \end{pmatrix}, \boldsymbol{\epsilon} = \begin{pmatrix} \epsilon_1 \\ \vdots \\ \epsilon_n \end{pmatrix}. \tag{3.43}$$

The hat of $\hat{\boldsymbol{\beta}}$ indicates that it is an estimator. Important assumptions for linear regression are, besides the linear independence of the independent variables, stochastic independence of the measurement errors, constant variances (homoscedasticity) and no correlation in the observed variances [96, p. 148]. In case of non-constant variances (heteroscedasticity), we can introduce a weighting matrix $\mathbf{W}$ with the variances in the diagonal $W_{ii} = \frac{1}{\sigma_i^2}$, for $i = 1, 2, \ldots, n$ and the solution for the linear regression reads:

$$\hat{\boldsymbol{\beta}} = (\mathbf{X}^\intercal \mathbf{W} \mathbf{X})^{-1} \mathbf{X}^\intercal \mathbf{W} \mathbf{y}. \tag{3.44}$$

In practice, the variance for a measurement point is obtained by repeating the measurement several times. If this is not possible, the variance can be estimated from the residuals of a previous ordinary linear regression [97, p. 236-237]. In linear regression, the minimum

found also represents the global minimum. Since the FFS models presented in sections 2.3 and 2.4 cannot be expressed as a linear combination of $\boldsymbol{\beta}$, nonlinear regression is needed. Since in nonlinear regression $\frac{\partial e_i}{\partial \beta_j}$ from equation 3.40 is a function of both the independent variable and the regression coefficients, there is in general no closed form for the best fit parameters and numerical methods are needed for solving. However, these are prone to local minima and therefore need good estimates for the starting parameters in the regression process. By using an iterative process, the parameters are successively approximated.

$$\beta_j \approx \beta_j^{k+1} = \beta_j^k + \Delta\beta_j, \tag{3.45}$$

with k being the number of iterations and $\Delta\boldsymbol{\beta}$ being the shift vector. At each iteration, the model is linearly approximated by a first-order *Taylor expansion.*

$$f(x_i, \boldsymbol{\beta}) \approx f(x_i, \boldsymbol{\beta}^k) + \sum_{j=0}^{p} \frac{\partial f(x_i, \boldsymbol{\beta}^k)}{\partial \beta_j}(\beta_j - \beta_p^k) = f(x_i, \boldsymbol{\beta}^k) + \sum_{j=0}^{p} J_{ij}\Delta\beta_j \tag{3.46}$$

$\mathbf{J}$ is the *Jacobian matrix* and contains constants, independent variables, and parameters. It therefore changes with each iteration step. The gradients and the Jacobian are related as follows:

$$\frac{\partial e_i}{\partial \beta_j} = -J_{ij}. \tag{3.47}$$

Linearization allows the optimization problem to be transformed into a linear system of equations consisting of n normal equations.

$$(\mathbf{J}^\intercal\mathbf{J})\boldsymbol{\delta\beta} = \mathbf{J}^\intercal\Delta\mathbf{y} \tag{3.48}$$

For the case of unequal confidence observations, a diagonal weighting matrix $\mathbf{W}$ can be introduced as in the case of linear regression.

$$(\mathbf{J}^\intercal\mathbf{W}\mathbf{J})\boldsymbol{\delta\beta} = \mathbf{J}^\intercal\mathbf{W}\Delta\mathbf{y} \tag{3.49}$$

The most widely used method for solving this problem is the *Levenberg-Marquardt algorithm* [98, 99]. It is characterized by the fact that it combines the gradient method with the method of linearization of the fit function. In addition, the algorithm converges quickly and can also overcome smaller local minima. However, in this work we will use the trusted-region reflective algorithm [100]. In addition to the above-mentioned advantages of the Levenberg-Marquardt algorithm, it offers the possibility to define upper and lower boundaries for the regression coefficients. This makes it possible to achieve better fitting results in some cases. In case of weighted regression, the sum of the residuals exactly matches the definition of the χ^2 value, which is defined as

$$\chi^2 = \sum_{i=1}^{n} \left(\frac{y_i - f(x_i;\boldsymbol{\beta})}{\sigma_i}\right)^2 = \sum_{i=1}^{n} \left(\frac{e_i}{\sigma_i}\right)^2. \tag{3.50}$$

with the gaussian error σ of each data point i. The χ^2 can be used to make a statement about the goodness of fit. For comparability between two models, however, it is useful to use the reduced Chi-Square.

$$\chi_\nu^2 = \frac{\chi^2}{\nu}, \tag{3.51}$$

with the degrees of freedom $\nu = n - p$. p is the number of free parameters $\beta_0, \beta_1, \ldots, \beta_p$ in the mode. Ideally, for each data point i, the squared deviation of the measurement curve from the fit function is equal to the variance of the measurement points themselves. This means that the squared residuals are equal to the variance, resulting in a theoretical χ^2_ν of 1. Values of $\chi^2_\nu > 1$ are an indication of incomplete modeling. Values of $\chi^2_\nu < 1$ indicate overfitting of the measurement data or overestimation of the standard deviation of the measurement [101, p. 1-2]. However, the interpretation of the χ^2_ν is sometimes hard, especially when the number of repetitions of the experiment is small. Even if the true model with the true parameters of a data set is known, χ^2_ν is only 1 in theory, in practice considerable deviations from 1 will be observed, because χ^2_ν itself is susceptible to noise in the data [101, p. 6-8]. Finally, the reduced chi square allows only a limited statement in nonlinear regression, because in nonlinear regression the number of degrees of freedom is not clearly defined [101, p. 4-5]. Nevertheless, several papers use the reduced chi square χ^2_ν as a measure of the goodness of fit (e.g., [77, p. 2993] or [102, p. 77-79]) and we will stick to this routine. To obtain the standard deviations for each measurement point, the average over 5 measurements is calculated with the associated standard deviation. An example of data evaluation is shown in figure 3.6. The data points were fitted with the corresponding model. In addition to χ^2_ν and R^2, the residuals can be used to assess the

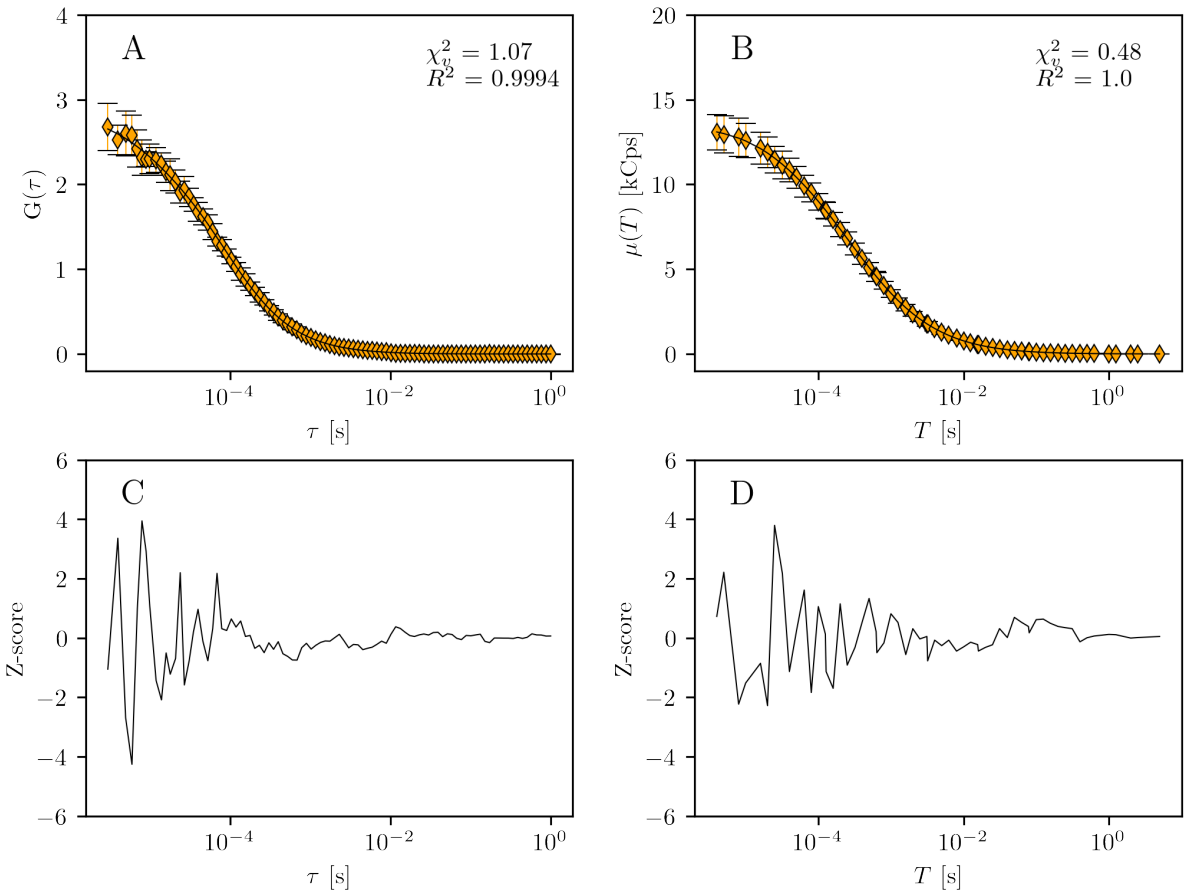

Figure 3.6: The fitting of FCS and mSMR curves via non-linear regression. Data retrieved from an Alexa Fluor 488 measurement . **A** Results of an FCS analysis with the associated residuals of the fit in subplot C. **B** Results of an mSMR analysis with the associated residuals of the fit in subplot D.

goodness of fit. The residuals from the fits are normalized using the following equation.

$$Z_i = \frac{(X_i - \mu)}{\sigma} \tag{3.52}$$

$(X_i - \mu)$ is the respective residual and σ is the standard deviation of the residuals. These normalized residuals are also called Z-transformed residuals or Z-scores and are plotted below the corresponding graphs. If no systematic deviations from the zero line are observed, the model used is suitable for describing the data. In the present example, there is no systematic deviation of the residuals from the zero line. The occurrence of larger deviations at small time intervals is common in FFS experiments. The visual impression of the fit together with the observation of the residuals and inconspicuous χ^2 and R^2 lead to the conclusion that the data in the present case are sufficiently well described by the models used.

4 The mSMR on simulated fluorescence fluctuations

In this chapter, the *mean single-molecule rate* (mSMR) is subjected to an initial review for the analysis of fluorescence fluctuations. The theoretical model of the mSMR in section 2.4 showed a comparable interpretation of the data curves to FCS analysis. In the mSMR model, however, the amplitude describes the single-molecule brightness rate instead of the reciprocal mean molecule number. The questition is, whether the mSMR model is also suitable for the analysis of fluorescence fluctuations under defined conditions. For this, it is appropriate to refer to simulated fluorescence traces. The usefulness of simulations to study single-molecule effects has been demonstrated in several studies. Using the Monte Carlo method, the influence of fluorescence saturation on the autocorrelation of FCS was examined [103, 46]. Also, the effect of detector dead time on FCS was systematically studied using simulated fluorescence traces [104]. The correlated photon-counting histogram (cPCH) model was developed and evaluated based on simulated data sets [41]. The same applies for a recent study, where an alternative framework was presented that, inspired by Bayesian non-parametric, requires only a few microseconds to seconds of fluorescence fluctuation data for analysis [105]. The examples show that the stochastic processes leading to fluorescence fluctuations are well understood, and simulation of these processes via the Monte Carlo method can yield new insights into the underlying mechanisms. We therefore use simulated fluorescence traces to subject the mSMR model to a systematic analysis. Thus, parameters that are difficult to access experimentally, such as the geometric ratio of the detection volume or the single-molecule brightness rate of a molecule, can be studied. In addition, measurement artefacts occur in real experiments (see section 2.5.1). The simulation allows to first analyze artefact-free fluorescence traces, then adding individual noise components to study their influence as well as their correction. Parts of this chapter were previously published in Sparrenberg et al. [24].

4.1 Experimental procedure

The fluorescence traces to analyze are retrieved via Monte Carlo simulation (see section 3.1). Table 4.1 shows the default values of the simulation. Fluorescence fluctuations are simulated for 10 s, with each run repeated 5 times to get better statistics. The lateral extension of the MDE or detection volume r_0 remains constant in all runs, while the axial extension may vary. The supplement *varied* behind some parameters indicates that this parameter is systematically changed in this study. Generally, only one parameter is varied at time. In some cases, however, the variation of one parameter causes another parameter to change, e.g., a change in the diffusion coefficient always affects the number of simulation steps for a given simulation time (see equation 3.1). Values that differ from the default values in table 4.1 are indicated in the results.

Table 4.1: General simulation parameters for the Monte Carlo experiments. The given values are default values. The supplement (varied) indicates whether this value is subject to systematical variations. The varied parameters are explicitly stated in the respective simulations.

Parameter	Value
Numer of cycles	5
Simulation time	10 s
Total steps	7 500 000 (varied)
Lattice - X	4.8 µm
Lattice - Y	4.8 µm
Lattice - Z	4.8 µm (varied)
MDE lateral (r_0)	0.4 µm
MDE axial (z_0)	0.4 µm (varied)
Transmission	100 %
Number of molecule species	1
Dead time	0 ns (varied)
Afterpulsing prob.	0 % (varied)
Afterpulsing decay	0 ns (varied)
Shot noise	0 kCps (varied)
Molecule species # 1	
Molecule number	20 (varied)
Diffusion coefficient	50 µm^2/s (varied)
Light factor	40 kCps (varied)
Bleach limit	Disabled

The systematic analysis of the simulated fluorescence traces is conducted in the following three steps:

1. FCS analysis of simulated fluorescence traces

To test reliability of our simulation engine, we generate fluorescence traces and analyze them by calculating the autocorrelation curves according to section 3.3.1. To fit the autocorrelation curves the FCS model is used 2.50. If the simulation engine works correctly, the initial simulation parameters from the fluorescence fluctuations should be recovered. In four simulation series the single-molecule brightness rate μ_0, the diffusion coefficient D, the number of simulated particles n_{sim}, and the axial to lateral ratio $r = z_0/r_0$ are varied systematically.

2. mSMR analysis on simulated fluorescence traces

Also, the simulated fluorescence traces from the previous step are analyzed using the mSMR method. From the fluorescence trace, mSMR curves are calculated as described in section 3.3.2. Then, a model fit is conducted to retrieve the initial simulation parameters from the mSMR curves.

3. Simulation of measurement artefacts

To better understand the influence of noise on FFS experiments, several measurement artefacts are mimicked in the simulation. First, afterpulsing events are simulated, which can occur with a certain probability. The time offset of the spurious afterpulsing event to the original event is modeled via an exponential probability distribution.

$$f(x;\lambda) = \lambda e^{-\lambda x} \qquad \text{for } x \geq 0, \tag{4.1}$$

with a rate parameter of $\lambda = 0.1\,\mu s$. Then, the influence of the detector dead time is considered by implementing a filter which only accepts one photon event within a detection window. If further photon events occur in this window, they will be ignored. Finally, uncorrelated background noise is analyzed. The noise is modeled by Poissonian noise (see equation 2.82) superimposing the fluorescence traces of diffusing particles.

4.2 Evaluation of the simulation engine using FCS

To test the reliability of the simulation engine, we evaluate a set of generated fluorescence fluctuations with the established fluorescence correlation spectroscopy. If the simulation works reliably, the input parameters should be recovered. The results are illustrated in figure 4.1. The autocorrelation curves of each five-fold parameter set are averaged into one curve and fitted with equation 2.50. Starting with the variation of the single-molecule rate μ_0 in subplot A, almost identical FCS curves are obtained for varying μ_0. All curves share the same amplitude. However, slight differences in noise occur between the FCS curves at small shifting times τ, whereas a higher single-molecule brightness rate results in less noise in the autocorrelations. Table 4.2 contains the results from the fit of the data with the FCS model. The diffusion times from the fit were converted to the diffusion coefficients via equation 2.48. Despite varying single-molecule brightness rates, the same mean particle number and same diffusion coefficient is obtained from the FCS model in each case. This illustrates the insensitivity of the FCS method to molecular brightness differences. However, there is less noise in the autocorrelation curves with larger single-molecule brightness rates. This is due to more photon events in these data, which has a favorable effect on the statistics. Overall, the model fitting results show good agreement with the original simulation parameters within standard deviations. Subplot B illustrates the systematic variation in diffusion coefficients. The FCS curves show the same amplitudes, but there are clear differences in the time course. With increasing diffusion coefficients, the FCS curves move towards shorter shifting times. Looking at the model fitting results in table 4.2, the initial simulation parameters are recovered by the FCS model within standard deviations. Thus, the observed shifts of the data points along the time axis in the graphs accurately represent the changes in the diffusion coefficients. Molecules with larger diffusion coefficients diffuse faster. So, they stay shorter in the detection volume, which shifts the FCS curves towards smaller τ and vice versa. Subplot C shows the FCS curves of the systematic variation of the particle numbers in the simulation volume. There are clear differences in the amplitudes of the curves. Small particle numbers result in higher amplitudes, whereas large molecule numbers yield lower amplitudes. Meanwhile, the time dependence of the curves seems to be unaffected.

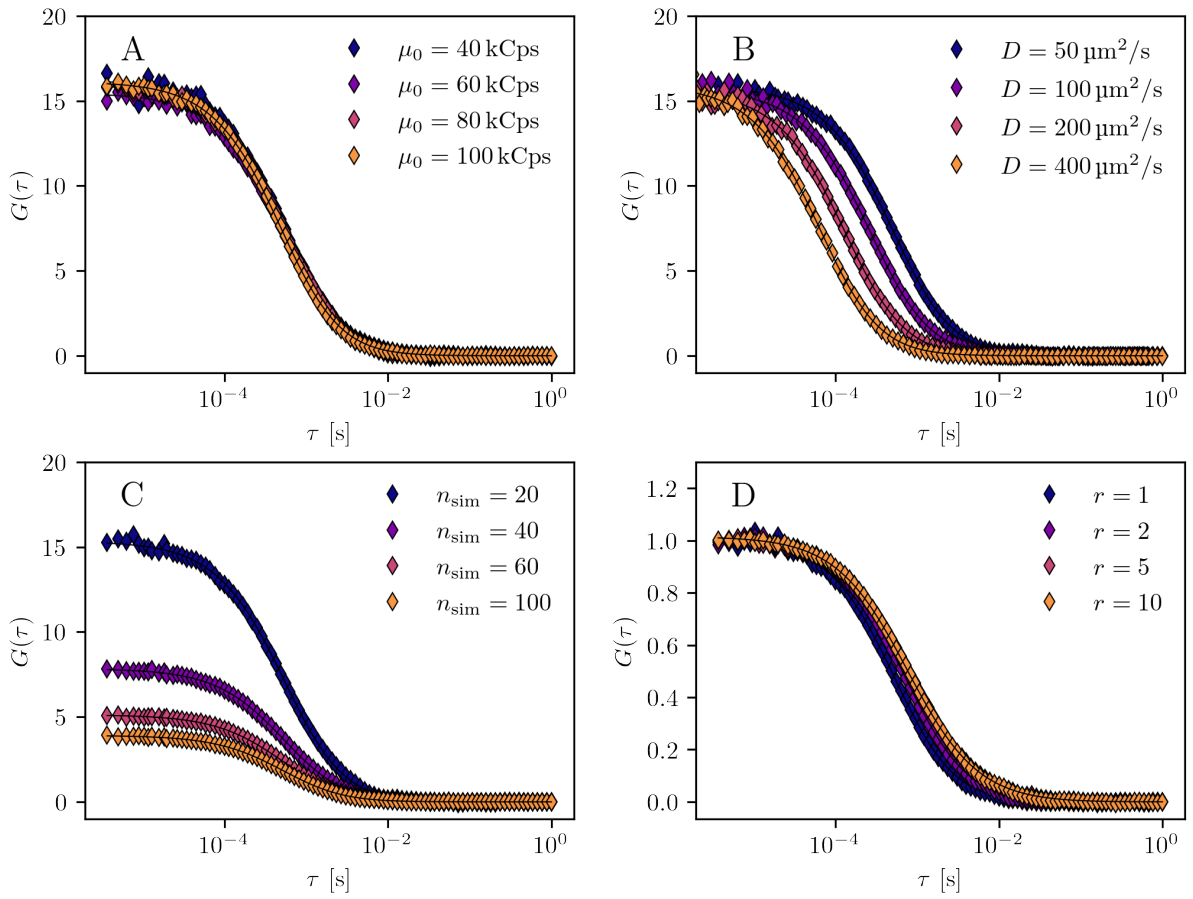

Figure 4.1: FCS results from simulated fluorescence traces. The general simulation parameters are: $r_0 = 0.4\,\mathrm{um}$, simulation time $t = 10\,\mathrm{s}$. **A** Varying single-molecule brightness rate μ_0. The other simulation parameters are $r = 1$, $D = 50\,\mu\mathrm{m}^2/\mathrm{s}$ and $n_{\mathrm{sim}} = 20$. **B** Varying diffusion coefficient D. The other simulation parameters are $r = 1$, $\mu_0 = 100\,\mathrm{kCps}$ and $n_{\mathrm{sim}} = 20$. **C** Varying simulated particle numbers n_{sim}. The other simulation parameters are $r = 1$, $D = 50\,\mu\mathrm{m}^2/\mathrm{s}$ and $\mu_0 = 100\,\mathrm{kCps}$. **D** Varying geometric ratio r. The other simulation parameters are $D = 50\,\mu\mathrm{m}^2/\mathrm{s}$, $\mu_0 = 100\,\mathrm{kCps}$ and $n_{\mathrm{sim}} = 20$. The data are normalized to unity for better comparability.

To compare the particle numbers n_{sim} in the simulation volume with the model fitting results $\langle N \rangle_{\mathrm{fit}}$, the expected mean particle numbers $\langle N \rangle_{\mathrm{sim}}$ in the effective detection volume must first be calculated via the following relation:

$$\langle N \rangle_{\mathrm{sim}} = n_{\mathrm{sim}} \frac{V_{\mathrm{eff}}}{V_{\mathrm{sim}}}, \tag{4.2}$$

whereas V_{eff} is given by equation 2.47. In this form, the results from the model fit and the simulation parameters can be compared in table 4.2. The results are in good agreement with the initial simulation parameters within the standard deviations. Since the amplitude is reciprocal to the mean number of particles, the decrease in amplitude correctly reflects the increase in particles in the simulation. Finally, subplot D displays the results for the simulations with varying geometric ratios of the effective detection volume. For the simulations the lateral expansion r_0 was kept constant while the axial expansion z_0 was increased stepwise. Since this changes the effective detection volume and thus the amplitude of the FCS curves, the curves are normalized to make them comparable to each other. The curve progressions for small r differ significantly, while for larger r there is hardly any difference to see. Simulations with $r = 20$ were also

Table 4.2: Results of the fit of the FCS model to the FCS curves of the simulated fluorescence traces. For the fitting parameters, the respective standard deviations are given.

Subplot A

Varied μ_0	$\langle N \rangle_{\text{fit}}$	$\langle N \rangle_{\text{sim}}$	D_{fit}	D_{sim}
40	0.062 ± 0.003	0.064	49.6 ± 3.1	50
60	0.065 ± 0.005	0.064	49.7 ± 1.7	50
80	0.063 ± 0.003	0.064	50.1 ± 1.9	50
100	0.063 ± 0.006	0.064	50.4 ± 2.7	50

Subplot B

Varied D	$\langle N \rangle_{\text{fit}}$	$\langle N \rangle_{\text{sim}}$	D_{fit}	D_{sim}
50	0.063 ± 0.004	0.064	53.1 ± 1.6	50
100	0.064 ± 0.004	0.064	100.9 ± 5.2	100
200	0.065 ± 0.002	0.064	201.4 ± 5.9	200
400	0.064 ± 0.002	0.064	404.7 ± 14.8	400

Subplot C

Varied N_{sim}	$\langle N \rangle_{\text{fit}}$	$\langle N \rangle_{\text{sim}}$	D_{fit}	D_{sim}
20	0.065 ± 0.001	0.064	49.5 ± 1.4	50
40	0.128 ± 0.002	0.129	49.7 ± 1.9	50
60	0.195 ± 0.008	0.193	51.4 ± 1.3	50
100	0.256 ± 0.004	0.258	50.4 ± 3.6	50

Subplot D

Varied r	$\langle N \rangle_{\text{fit}}$	$\langle N \rangle_{\text{sim}}$	D_{fit}	D_{sim}
1	0.063 ± 0.003	0.064	50.1 ± 4.7	50
2	0.110 ± 0.008	0.110	51.8 ± 2.5	50
5	0.191 ± 0.004	0.193	50.2 ± 2.7	50
10	0.254 ± 0.009	0.258	53.3 ± 2.7	50

carried out but cannot be distinguished from the curves with $r = 10$ and are therefore not shown. The differences occur mainly around the lower part of the FCS curve in the asymptotic approach to the baseline. However, there is also a slight change in the slopes. The table 4.2 also summarized the results of the fitting routine. Because of the model's low sensitivity to the geometric ratio, it is fixed during the fitting routine. Again, the FCS results agree within standard deviations with the initial simulation parameters.

After studying the reliability of the simulation engine by analyzing the fluorescence traces with the well-established FCS analysis, we can focus on the evaluation of the mSMR.

4.3 mSMR on simulated fluorescence traces

The mSMR is introduced as a new tool to analyze fluorescence traces and to make statements on the single-molecule level. As already mentioned in the theory section, the interpretation of the mSMR curves and the autocorrelation curves of FCS analysis is similar and comparisons between the FCS and mSMR models can easy be made. We use the data set from the previous section to study the validity of the mSMR systematically. Like the FCS, the mSMR should reliably reproduce the input parameters of the simulation. Figure 4.2 shows the results of the mSMR analysis. The mSMR curves of each five-fold parameter set are averaged and fitted with equation 2.75. Subplot A

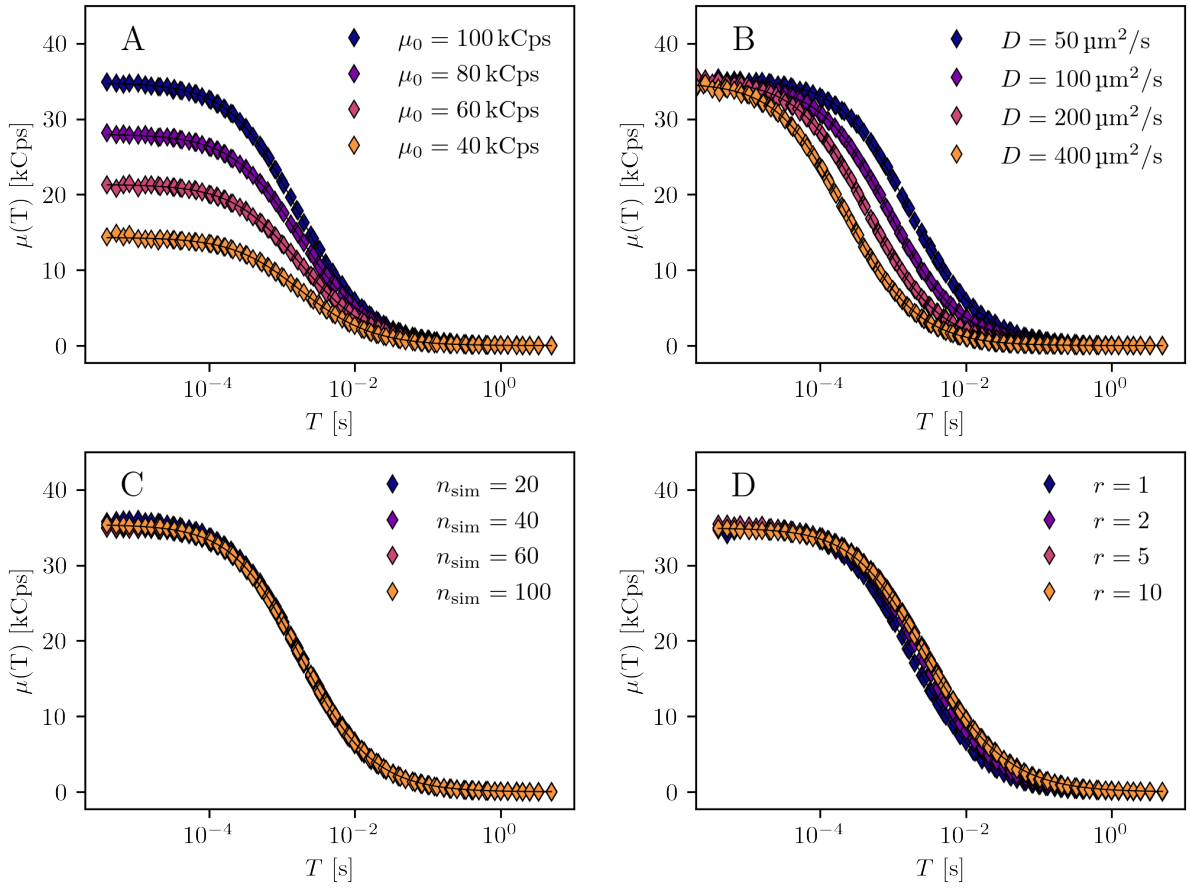

Figure 4.2: mSMR results from simulated fluorescence traces. The general simulation parameters are: $r_0 = 0.4$ um, simulation time $t = 10$ s. **A** Varying single-molecule brightness rate μ_0. The other simulation parameters are $r = 1$, $D = 50\,\mu\mathrm{m}^2/\mathrm{s}$ and $n_{\mathrm{sim}} = 20$. **B** Varying diffusion coefficients D. The other simulation parameters are $r = 1$, $\mu_0 = 100\,\mathrm{kCps}$ and $n_{\mathrm{sim}} = 20$. **C** Varying simulated particle number n_{sim}. The other simulation parameters are $r = 1$, $D = 50\,\mu\mathrm{m}^2/\mathrm{s}$ and $\mu_0 = 100\,\mathrm{kCps}$. **D** Varying geometric ratio r. The other simulation parameters are $D = 50\,\mu\mathrm{m}^2/\mathrm{s}$, $\mu_0 = 100\,\mathrm{kCps}$ and $n_{\mathrm{sim}} = 20$.

shows the mSMR curves for a varying single-molecule brightness rate. Clear differences appear in the amplitudes , which seem to be proportional to the given single-molecule brightness rates. The time dependence, on the other hand, appear to be the same for all curves. It is noticeable that the mSMR curves show a very smooth course. The results from the model fitting can be found in table 4.3. As with FCS, the mean diffusion times were converted to the diffusion coefficients via equation 2.48. The fitting results correspond to the initial parameters of the simulation within standard deviations. The change in amplitude thus accurately reflects the respective single-molecule brightness

Table 4.3: Results of the fit of the mSMR model to the mSMR curves of the simulated fluorescence traces. For the fitting parameters, the respective standard deviations are given.

Subplot A

Varied μ_0	$\mu_{0,\text{fit}}$	$\mu_{0,\text{sim}}$	D_{fit}	D_{sim}
40	40.5 ± 0.6	40	49.5 ± 3.6	50
60	60.3 ± 1.4	60	50.37 ± 1.7	50
80	79.2 ± 1.83	80	50.5 ± 1.6	50
100	98.4 ± 2.6	100	54.2 ± 3.1	50

Subplot B

Varied D	$\mu_{0,\text{fit}}$	$\mu_{0,\text{sim}}$	D_{fit}	D_{sim}
50	99.5 ± 4.8	100	53.3 ± 2.5	50
100	98.1 ± 2.2	100	102.4 ± 5.3	100
200	99.3 ± 2.5	100	204.2 ± 6.1	200
400	98.5 ± 2.3	100	406.8 ± 16.4	400

Subplot C

Varied N_{sim}	$\mu_{0,\text{fit}}$	$\mu_{0,\text{sim}}$	D_{fit}	D_{sim}
20	101.6 ± 3.4	100	49.9 ± 1.8	50
40	99.5 ± 0.6	100	50.2 ± 2.6	50
60	99.7 ± 1.6	100	51.1 ± 1.1	50
100	100.1 ± 3.1	100	50.5 ± 3.3	50

Subplot D

Varied r	$\mu_{0,\text{fit}}$	$\mu_{0,\text{sim}}$	D_{fit}	D_{sim}
1	99.6 ± 3.4	100	49.6 ± 4.4	50
2	99.4 ± 3.9	100	51.4 ± 2.4	50
5	99.7 ± 2.4	100	50.6 ± 2.7	50
10	98.8 ± 3.3	100	52.9 ± 3.2	50

rate, which confirms the visual impressions from the graph plots. Subplot B presents the mSMR curves for varying diffusion coefficients. As in the FCS analysis in the previous section, the curves differ only in the time scale. As with FCS, larger diffusion coefficients lead to a shift of the curves towards smaller sampling times. The amplitudes, however, are the same for all curves. A look at table 4.3 shows that the results from the model fit agree with the initial parameters within standard deviations. Thus, the observations correspond to the theoretical predictions of the model. Larger diffusion coefficients mean that the molecules are moving faster, thus having a shorter residence time in the detection volume. This results in a shift to shorter sampling times. On the other hand, the single-molecule brightness rates do not differ between the simulation runs and the amplitudes should be the same, which is what we see. The results of the varying particle numbers is depicted in subplot C. The four mSMR curves are almost completely superimposed and show the same amplitudes and time courses. The fitting results in table 4.3 confirm this visual impression. No significant differences are observed in the single-molecule brightness and the diffusion coefficient. Here, the complementary behavior of the mSMR to the FCS method is evident. While the FCS reacts sensitively to concentration changes and ignores brightness differences in the molecules, this is exactly

the opposite with the mSMR. The results are again the same as the initial simulation parameters within standard deviations. Finally, subfigure D depicts the mSMR data for different geometric ratios resulting from a stepwise increase of the axial expansion while keeping the lateral expansion constant. The curve shapes of the mSMR show the same amplitude, whereas the time courses have small differences. These are noticeably pronounced for small r and disappear for large $r > 5$. Between $r = 5$ and $r = 10$, practically no differences can be seen. As with FCS, the dependence of the model on r is weak for $r > 5$ and the model fit is therefore performed with fixed r. Table 4.3 illustrates that under this condition, the mSMR model can reliably recover the simulation parameters within the standard deviations.

The mSMR model reliably yields the initial simulation parameters from the fluorescence fluctuation data. The mSMR curves are characterized by their smooth course and seem to be less noisy than the FCS curves.

4.4 Consideration of measurement artefacts

So far, fluorescence traces have been studied under ideal conditions. In real measurements, however, measurement artefacts occur. The simulation engine is an ideal tool to access these effects for a systematic study. To study the influence of noise components in more detail and evaluate the correction terms, detector afterpulsing, detector dead time, and uncorrelated background noise is considered.

4.4.1 Afterpulsing

To visualize the impact of afterpulsing on FFS experiments, we compute a series of simulations with gradually increasing afterpulsing probabilities. The results of the mSMR and FCS analyses are shown in figure 4.3, whereas the curves of each five-fold parameter set are averaged. Subplot A shows the mSMR for varying afterpulsing probabilities. An additional exponential decay in the mSMR curves at short sampling times is striking. With increasing afterpulsing probabilities, this effect increases. But even at a low afterpulsing probability of 0.5 %, a significant impact on the mSMR curves at short sampling times is observable. For larger sampling times, the afterpulsing effect completely disappears and the remaining characteristic curve of the mSMR is preserved. In subplot B we can see the results of afterpulsing correction using the equations 3.30 and 3.31. The mSMR curves are now in good agreement with each other. For the afterpulsing probabilities of 0.5 % and 1.0 % there is practically no difference to the data without afterpulsing. Only for afterpulsing probabilities of 1.5 % a slight overcompensation of the mSMR curves can be seen. This shows a limitation of the correction, since only first-order afterpulsing events are taken into account. However, the simulation also models higher order afterpulsing events. Meaning, one afterpulsing event can cause further afterpulsing events. However, this poses no problem in practice since modern photodetectors have afterpulsing probabilities of $< 1\,\%$, which makes higher order afterpulsing events rare. Interestingly, the afterpulsing effect is not visible in the FCS analysis (see subplot C). But the FCS curves are significantly noisier than the corresponding mSMR curves. This becomes especially evident in the direct comparison between subplot B and C. Because we expect afterpulsing is to be also an issue in the FCS analysis, the time steps in the simulation are probably too large to resolve afterpulsing in the FCS. Therefore, we refer to

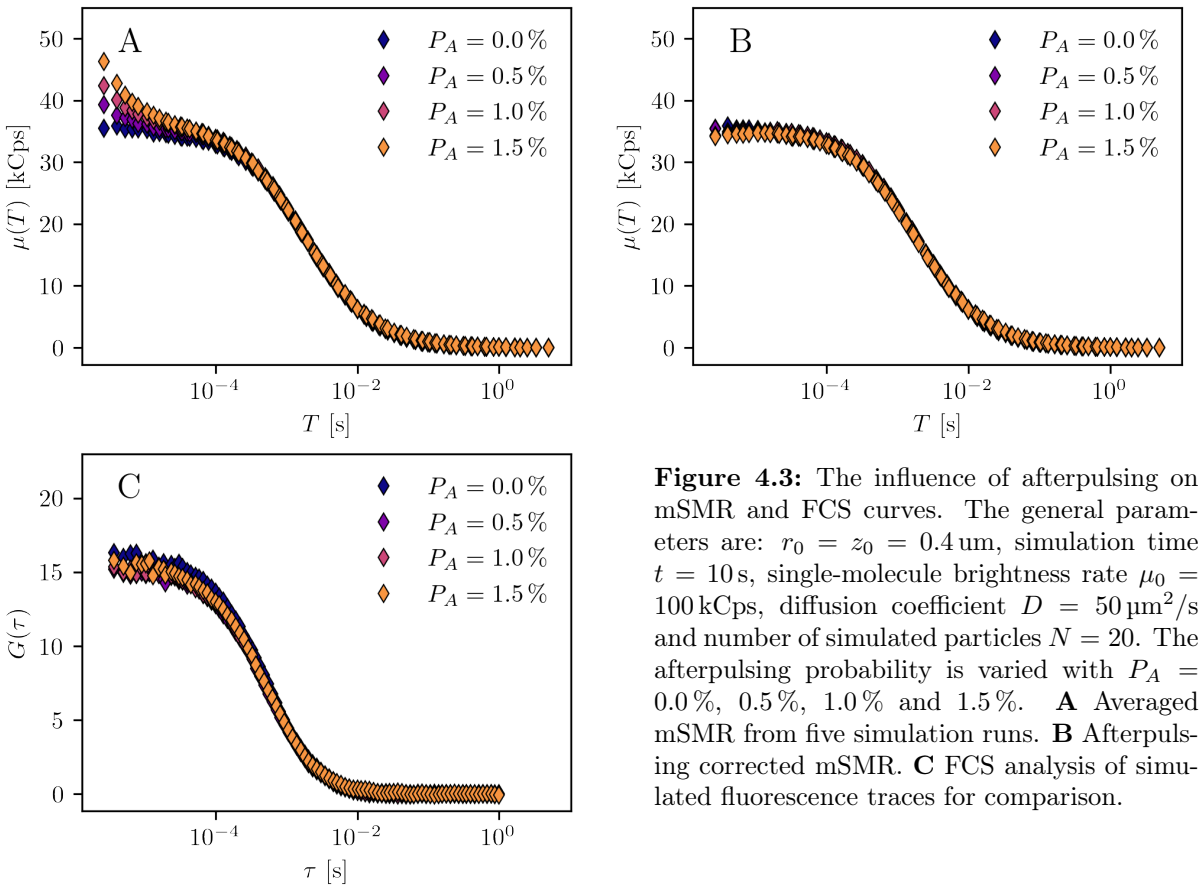

Figure 4.3: The influence of afterpulsing on mSMR and FCS curves. The general parameters are: $r_0 = z_0 = 0.4\,\mu m$, simulation time $t = 10\,s$, single-molecule brightness rate $\mu_0 = 100\,kCps$, diffusion coefficient $D = 50\,\mu m^2/s$ and number of simulated particles $N = 20$. The afterpulsing probability is varied with $P_A = 0.0\,\%$, $0.5\,\%$, $1.0\,\%$ and $1.5\,\%$. **A** Averaged mSMR from five simulation runs. **B** Afterpulsing corrected mSMR. **C** FCS analysis of simulated fluorescence traces for comparison.

data sets with $10\times$ more time steps ($75\,000\,000\,s^{-1}$ instead of $7\,500\,000\,s^{-1}$) and can indeed observe afterpulsing effects in the autocorrelation curves (see figure 10.2 in the appendix).

To conclude, the correction of afterpulsing for commonly occurring probabilities works well for the mSMR analysis. Especially for the analysis of photokinetic effects a correction is necessary.

4.4.2 Detector dead time

For the analysis of detector dead time, fluorescence fluctuations of particles with increasing single-molecule brightness rates are computed, while the detector dead time is set to 100 ns. For a constant particle concentration, this leads to higher photon counts increasing the probability that photon events occur within the dead time and thus are not counted. The averaged results of each five-fold parameter set are included in figure 4.4. In subplot A, the normalized dead time affected mSMR curves are shown. Due to the different single-molecule brightness rates, a meaningful comparison is not possible without normalization. So, simulations without detector dead time are also conducted to normalize the amplitudes of the dead time affected mSMR curves. For increasing μ_0, a decrease in the mSMR curves appears, especially at short sampling times. While for small μ_0, the mSMR is hardly affected, larger μ_0 even cause a decrease of the amplitude. Without correction, this strongly affects the evaluation of the mSMR curves. The dead time corrected mSMR curves can be seen in subplot B. Equations 3.30 and 3.31 were used for correction. Now, all curves form a plateau at about $\mu(T) = 1.0\,kCps$. However, for the mSMR with very bright μ_0, we can still detect a slight downward deviation from

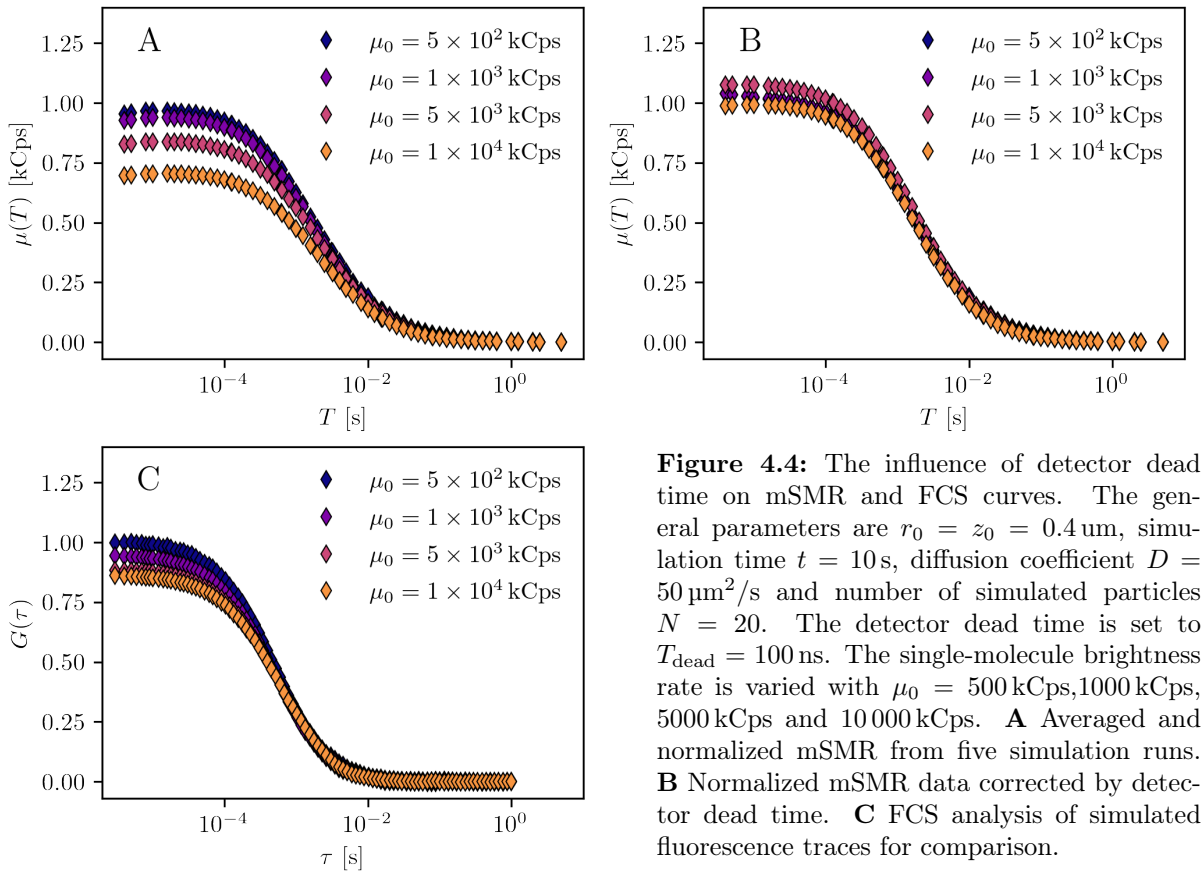

Figure 4.4: The influence of detector dead time on mSMR and FCS curves. The general parameters are $r_0 = z_0 = 0.4\,\mu m$, simulation time $t = 10\,s$, diffusion coefficient $D = 50\,\mu m^2/s$ and number of simulated particles $N = 20$. The detector dead time is set to $T_{dead} = 100\,ns$. The single-molecule brightness rate is varied with $\mu_0 = 500\,kCps$,1000 kCps, 5000 kCps and 10 000 kCps. **A** Averaged and normalized mSMR from five simulation runs. **B** Normalized mSMR data corrected by detector dead time. **C** FCS analysis of simulated fluorescence traces for comparison.

the other curves. The FCS analysis of the simulated fluorescence traces is shown in subplot C. As for the mSMR, we see an influence of the detector dead time on the data curves. Compared to the mSMR, the deviations are significantly smaller, but they are clearly present. In contrast to the mSMR, however, no correction is available for FCS analysis.

The previous results proved a strong dead time effec on the mSMR curves at high count rates. However, this can be eliminated by an appropriate correction.

4.4.3 Background noise

In this section, we subject the background noise to a more detailed analysis. For this, the simulated fluorescence traces are overlaid with different amounts of Poissonian noise. For better statistics, each simulation run is conducted five-fold and averaged after analysis. The results of the analysis are illustrated in figure 4.5. The mSMR data series for increasing background noise fractions are included in subplot A. With increasing noise, the amplitude of the mSMR curves decreases. Without correction, this leads to a significant underestimation of the single-molecule brightness rate. For the correction we need to determine the background noise of the measurement. In practice, we would perform a blank measurement for this purpose. In the present case, we know the noise component from the simulation and can correct the mSMR directly using equation 3.37. The results of the background noise correction are depicted in subplot B. The correction brings the mSMR data series into precise alignment. For FCS analysis, the same effect of

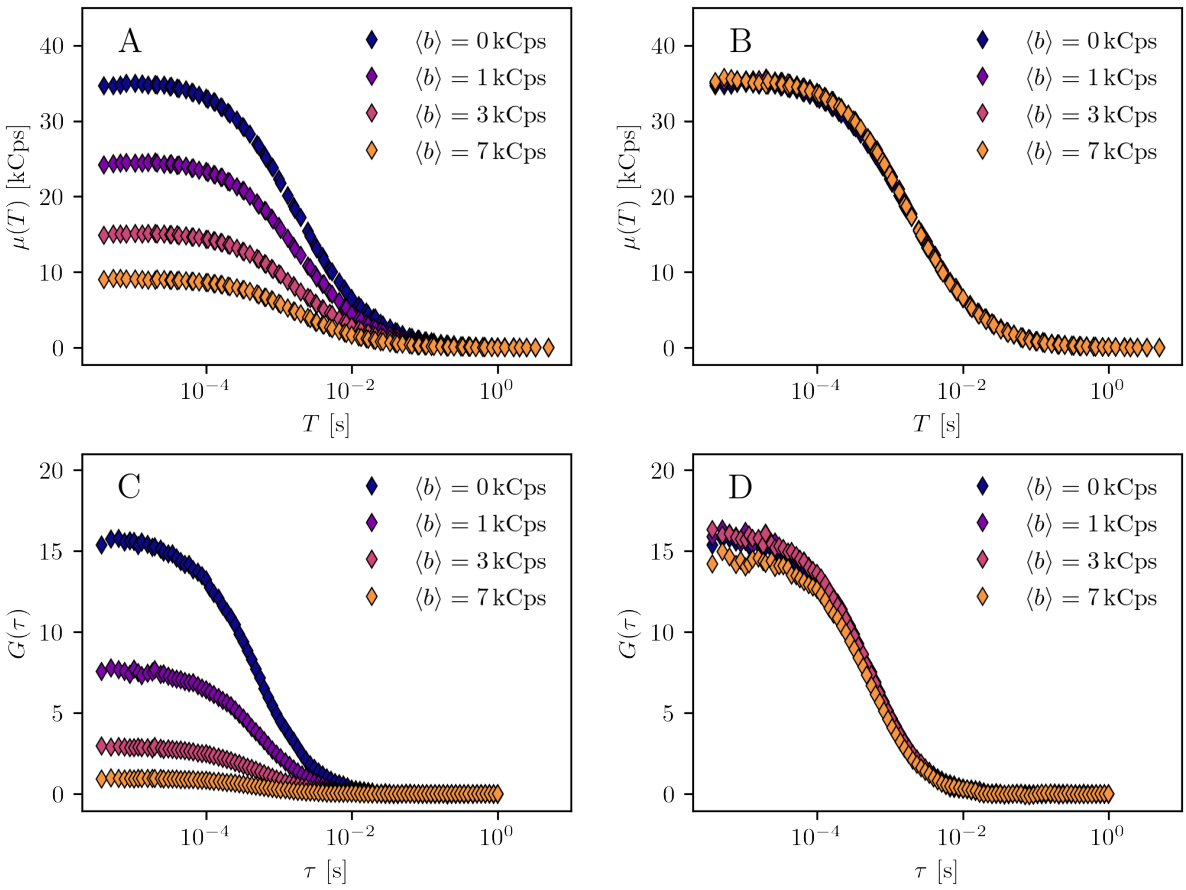

Figure 4.5: The influence of background noise on mSMR and FCS curves. The general parameters are: $r_0 = z_0 = 0.4\,\mu m$, simulation time $t = 10\,s$, single-molecule brightness rate $\mu_0 = 100\,kCps$, diffusion coefficient $D = 50\,\mu m^2/s$ and number of simulated particles $N = 20$. The fluorescence traces are overlayed by varying noise fractions of $\langle b \rangle = 0\,kCps$, $1\,kCps$, $3\,kCps$ and $7\,kCps$. **A** Averaged mSMR for varying noise fractions. **B** Noise corrected mSMR. **C** Averaged FCS for varying noise fractions. **D** Noise corrected FCS.

background noise is evident in subplot C. Again, the amplitude is reduced by increasing noise components. This leads to an overestimation of the actual number of particles in the observation volume. The correction here is analogous to the mSMR using equation 3.34. The corrected FCS data series in subplot D also show good agreement. However, once again, the FCS curves are significantly noisier than the mSMR curves.

The influence of background noise on the FFS analyses is evident. Without correction, we would significantly underestimate the single-molecule brightness rate in the mSMR and significantly overestimate the mean particle number in the FCS. After correction, comparable results are obtained. In real measurements, the background noise can be easily determined by a blank measurement and accordingly corrected.

4.5 Discussion

The Monte Carlo method is a powerful tool to analyze fluorescence fluctuations and related effects. We used the Monte Carlo method to subject the mSMR model to a systematic examination. Therefore, we first evaluated our implementation of the simulation using the established FCS method. For this, fluorescence traces with varying parameters were generated and evaluated systematically. The molecular properties (single-molecule brightness rate, diffusion coefficient) were changed stepwise, as well as the experimental parameters (particle concentration, geometric ratio of the detection volume). The initial input parameters of the simulation could be retrieved within the standard deviations. This observation is important to be able to derive reliable statements about the mSMR method. An important observation is that the FCS has only a low sensitivity to correctly resolve large axial to radial ratios of the detection volume (i.e., $r > 5$). However, if the correct geometric ratios are known, a reliable evaluation of the fluorescence fluctuations is still possible. This has a direct implication on later measurements with the confocal plate reader (see chapters 5 and 6), which uses a long-distance objective lens. With such an optical setup, we expect large axial to radial ratios of the detection volume. Therefore, to ensure a reliable evaluation, the confocal plate reader must be thoroughly calibrated to get the precise geometric proportions of the detection volume. Since it is not practical to fit real measurement data with freely adjustable r, the geometric ratio should be determined with a concise calibration routine. For this, fluorescent dyes with known concentration and well described diffusion coefficients (e.g. Alexa Fluor 488) are suitable. It is recommended to determine the device parameter r via the theoretical effective volume as described in section 5.2). Afterwards, this value should be fixed for the fitting routine. In addition to these practical hints, the reliability of the simulation engine can be councluded. Thus, we can use it to conduct further studies to verify the mSMR model. However, a healthy skepticism should always be maintained with the results of simulations since they are merely models of reality and can therefore only represent it to a limited extent.

After successfully verifying our implementation of the Monte Carlo method, the essential part of this chapter comes into focus, the evaluation of the mSMR model. The mSMR showed that it can derive the initial simulation parameters from the fluorescence fluctuations within the standard deviations, as FCS did. Thereby, it is shown that when varying the diffusion coefficients and geometric ratios, the resulting graphs of the FCS and mSMR analyses display comparable progressions. In contrast, the graphs for varying single-molecule brightness rates and particle numbers show significant differences. The FCS can resolve subtle concentration differences via the amplitudes, while mSMR reveals subtle differences in single-molecule brightness rates in the amplitudes. Since we expect this observation from theory (compare figures 2.12 and 2.14), we can conclude that the mSMR model reliably describes idealized fluorescence fluctuation data. By comparing the graphs of the two models more closely, the smoother mSMR curves compared to FCS become apparent. Especially for fluorescence traces with few photon events, as they occur at low concentrations or for particles with low single-molecule brightness rates, this aspect becomes clearly visible. In addition, the mSMR curves are slightly shifted along the time axis to longer time scales compared to FCS. Together with the smoother curves, this could be an important advantage of the mSMR model over the FCS in the analysis of fluorescence traces at small time scales. This becomes especially important in the study of photokinetic effects, as they take place at very short time scales. We

will therefore study this aspect in more detail in the following chapters 5 and 6 by examining the photokinetic effects of triplet state and isomerization in real FFS experiments.

In addition to these idealized fluorescence fluctuations, we addressed the influence of measurement artefacts. These experiments are an excellent example of the benefits of simulation since measurement artefacts are difficult to study systematically under real conditions. The simulation enables to examine this aspect in more detail.
Firstly, the effect of afterpulsing is discussed. When afterpulsing is activated, the mSMR analysis shows an additional exponential decay at very short sampling times, whereas the data at larger sampling times are not affected. In principle, the mSMR curves could still be evaluated by simply omitting the data at short sampling times before fitting. However, the data at short sampling times are essential for subsequent photokinetic analyses and a correction of afterpulsing is useful. Interestingly, no comparable effect is observed in the FCS analysis. Since the effect of afterpulsing is described in the literature for FCS (see among others [85, 86]), it can be assumed that FCS requires lower time resolutions to be affected by afterpulsing. The time resolution in the simulation is based on the diffusion properties of the simulated particles via equation 3.1 and not on the time scale of the afterpulsing. Therefore, the used time resolution in the simulation might be too large. In fact, by reducing the time intervals in the simulation to one tenth, the afterpulsing effect becomes also visible in the FCS analysis. Using equations 3.30 and 3.31, to correct the first and second cumulants in the mSMR model, the afterpulsing effect can be eliminated and the data can be fitted using the mSMR model. In FCS, however, afterpulsing correction requires a *time-correlated single photon counting* (TCSPC) setup that records photon lifetimes using a pulsed laser [85, 86]. When using a continues wave laser a direct correction of the autocorrelation curves is not available.
Secondly, the effect of detector dead time is subject to discussion. The number of photons at the detector is decisive for the strength of the effect. In principle, the count rate can be increased via the single molecule brightness rate or the number of simulated fluorophores. Since increasing the number of simulated fluorophores drastically increases the computational time of the simulation, the single molecule brightness rate is changed. Both the normalized mSMR curves and the FCS curves show are sensitive to dead time. But the effect on the mSMR curves is much more pronounced than on the FCS curves. Interestingly, a reduction not only on short-time scales but over the whole amplitude arises. This leads to an underestimation of the single-molecule brightness rates in mSMR analysis or an overestimation of the mean particle numbers in FCS analysis. Therefore, unlike afterpulsing, detector dead time cannot be bypassed by omitting the affected data points at short-time scales. Therefore, no meaningful evaluation is possible without a suitable correction. For the mSMR the effect of dead time can be corrected via equations 3.30 and 3.31. However, at the largest single molecule brightness, the correction was incomplete, and the theoretical amplitude could not be recovered. The correction is only valid for $\langle k \rangle \, \delta \ll 1$ (see section 3.3.3), which is no longer valid for high-count rates due to the high single-molecule brightness rate. Thus, strict compliance with the criterion is required, otherwise the correction itself is erroneous. This shows that already during the experimental design the expected count rates have to be kept low, e.g. by choosing low excitation powers and by a low number of fluorescent particles in the detection volume. To the best of our knowledge, there is no dead time correction for FCS to date, so the only reliable action against detector dead time in FCS measurements is to work with low excitation powers.

Thirdly, the influence of Poissonian background noise on the mSMR and FCS is examined. In both cases, increasing noise leads to a reduction of the amplitudes in the models. However, the effect of background noise can be completely corrected in both models. The only information needed for correction is the background noise that can be acquired in a separate blank measurement in real world applications.

In summary, the preceding experiments demonstrated some essential properties of the mSMR model. Most importantly, the mSMR can derive the input parameters of the simulation from the generated data sets. Thereby, the mSMR curves are smoother and slightly shifted to larger time scales compared to FCS. Especially at short-time scales the mSMR shows smaller variances in the data than the FCS. In addition, the ability to correct the detector artefacts of afterpulsing and dead time at the cumulant level is an advantage of the mSMR over the FCS and could facilitate the analysis of processes at short-time scales. When studying photokinetic effects, this could be a decisive advantage and make short-time processes more amenable to evaluation. Having shown that the mSMR model allows reliable evaluations of simulated fluorescence traces, we can proceed with measurements on real dye systems using the home-built confocal plate reader.

5 The mSMR in real measurements

Up to this point, idealized simulation data were analyzed. We now want to get a step further and consider genuine fluorescence fluctuation data. Two objectives are envisaged. First, our home-built confocal plate reader (see section 3.2) is to be evaluated and calibrated for the collection of FFS data. Second, the mSMR model is to be studied under real conditions and compared to the FCS model. Thereby, we aim to make FFS analyses available to a broader community to elucidate biological questions.
To initially establish well-defined conditions and keeping the complexity low, measurements on mere dye solutions are conducted. The fluorescent dye Alexa Fluor 488 is used, which is characterized by a large single-molecule brightness rate while showing a low tendency to switch to the long-lived triplet state. This property mitigates the effect of fluorescence saturation (compare figure 2.3), allowing measurements over a wider range of excitation powers while maintaining an approximately linear fluorescence increase. In addition, the diffusion coefficient of Alexa Fluor 488 is well determined [89]. Because of the aforementioned properties, Alexa Fluor 488 is well suited for the evaluation and calibration of the confocal plate reader using FCS analysis. We want to shed light on whether the confocal plate reader is capable of single-molecule detection and can automatically achieve highly reproducible measurement results.
To evaluate the mSMR model, the previous data set is re-used to obtain a high degree of comparability between the FCS and mSMR models. Althought, common measurement artefacts can be corrected in simulated data sets, the performance of the correction with real measurement data is not yet clear. Therefore, the correction of measurement artefacts and their successive correction is studied separately. Afterwards, the similarities and differences between the two models are compared and discussed. This will take place both at the level of the diffusive model and at the level of the triplet model. This allows us to compare the processes on both long- and short-time scales and drawing conclusions about the validity of the FCS and mSMR models to describe the photokinetic effect of triplet transition. After the visual comparison, a statistical analysis helps to compare of the models in greater thoroughness. It focusses on experimental conditions with low excitation powers and low molecular concentrations to study the results from the fit routines in more detail. Parts of this chapter were previously published in Sparrenberg et al. [24].

5.1 Experimental procedure

The measurements in this chapter are performed using a home-built confocal plate reader. The plate reader automates the measurement procedure by independently approaching the wells of a microtiter plate, finding the appropriate focal plane and performing five measurements at adjacent locations in the well. The measurements are carried out exclusively on Alexa Fluor 488 solutions. Table 5.1 summarizes the measurement parameters. Alexa Fluor 488 is diluted in ultra pure water to set up concentration steps from 0 pM to 500 pM. Then, 20 µL of each dilution step are loaded onto a 384 well microtiter plate. The filled wells are then covered with a foil to minimize evaporation. Data collection is

Table 5.1: Measurement parameters of Alexa Fluor 488 studies.

Sample preparation	
Microtiter plate	384 well (μclear, non-binding, Greiner BioOne, Germany)
Fluorescent dye	Alexa Fluor 488 (NHS ester, ThermoFisher Scientific, USA)
Solvent	Water (HPLC grade, Roth, Germany)
Concentration steps	0, 5, 10, 20, 25, 50, 100, 200, 300, 400, 500 pM
Sample volume	20 µL
Setup parameters	
Measurement time	10 s
Sampling time	1×10^{-6} s
Measurement repeats	5
Laser power	Varied
Excitation light	488 nm
Emission filter	535/50
Objective lens	63x/0.75 LD

performed for 10 s with a sampling time of 1 µs. The excitation intensities vary between 30 µW to 140 µW and are indicated in the results.
For the latter statistical analysis of the two models, 39 adjacent wells of the microtiter plate are prepared with 50 pM Alexa Fluor 488 solution in ultra pure water and measured at 10, 30 and 50 µW laser power. The remaining measurement parameters are the same as given in table 5.1.

5.2 Evaluation and calibration of the confocal plate reader

In the following section the confocal plate reader is introduced and evaluated as a tool for FFS analysis.

Evaluation

Since the home-built confocal plate reader is used for all measurements on real samples, we first need to address its suitability for collecting FFS data. For this, the plate reader conducts measurements on Alexa Fluor 488 dilution series. Special attention is given to the reproducibility as well as the ability to perform measurements on the single-molecule level.
Four different excitation powers (10 µW, 30 µW, 50 µW and 70 µW) are used for the measurements because of two reasons. First, this provides more measurement data for evaluation and thus better statistics. Second, because of fluorescence saturation (see section 2.2.4), suitable excitation powers must be ensured, where no deviations occur. For evaluation, the fluorescence count rates from the measurement are first considered. Then, the autocorrelation curves of FCS analysis are calculated according to section 3.3.1 to analyze the mean particle counts and diffusion times. Figure 5.1 shows the results of the measurements. In subplot A, the fluorescence count rates of the dilution series at different excitation powers can be seen. The fluorescence counts of each dilution series

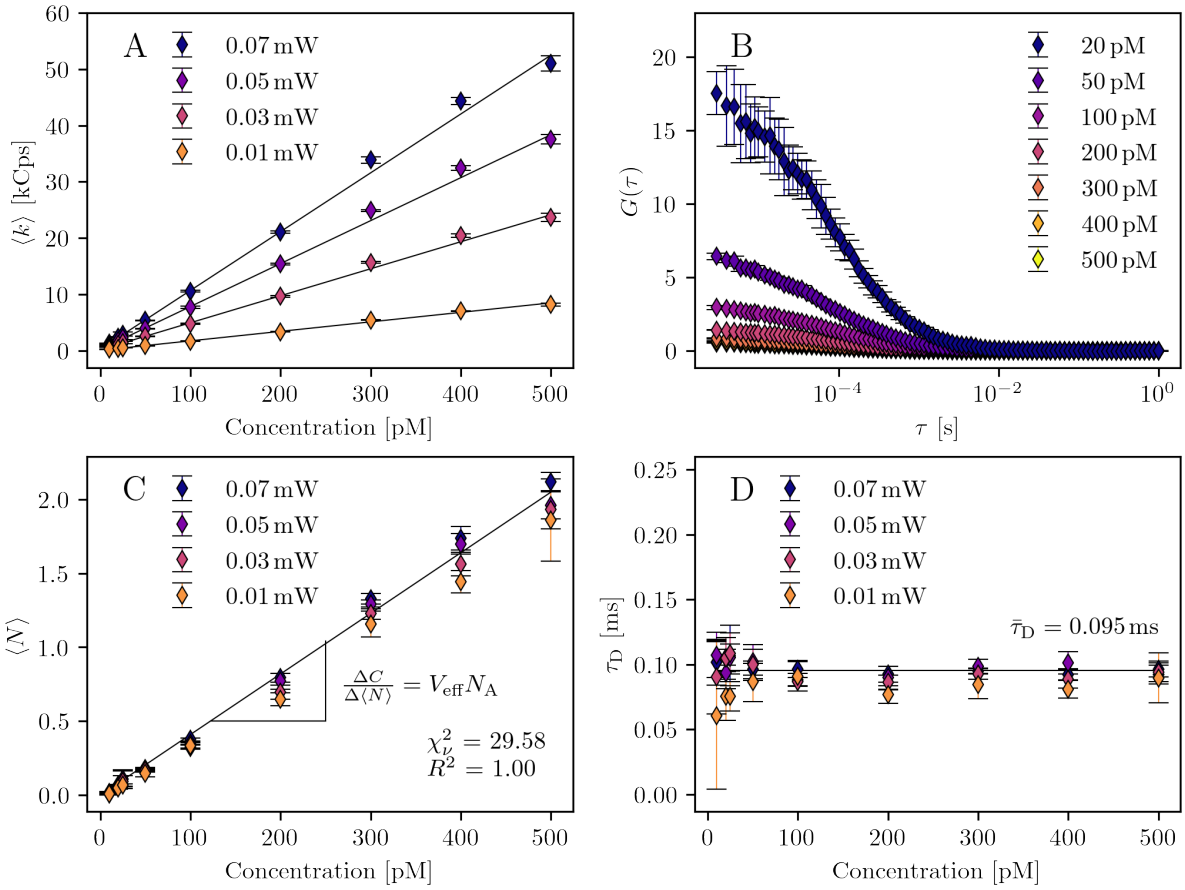

Figure 5.1: Evaluation and calibration of the confocal plate reader using measurements on Alexa Fluor 488 dilution series. The fluorescence fluctuations are retrieved at different excitation powers and analyzed using the FCS method. **A** Fluorescence counts of the measurement. The data are fitted with a straight line $f(x) = \beta_0 + \beta_1 x$. **B** Noise-corrected and averaged FCS curves at an excitation power of 70 µW. **C** The average number of particles in the detection volume. The data are fitted with a straight line through the origin $f(x) = \beta_1 x$. **D** Averaged mean diffusion times from the FCS analysis.

increase as a function of concentration and can be well described by a straight line. The slopes of the straight lines are almost proportional to the excitation power. The linear relationship in the count rates indicates that the dilution series were accurately prepared and that further analysis is promising. Additionally, the count rates have only small error bars, which shows the plate reader's ability to perform measurements automatically and reproducibly. The results of the FCS analysis of a dilution series can be seen in subplot B. It shows exemplary FCS curves of the dilution series recorded at 70 µW excitation power. The curves of the five-fold measurements of each concentration step are averaged and corrected for background noise according to equation 3.34. The decrease in the amplitudes for increasing concentrations can be clearly seen. At the lowest dye concentration of 20 pM, the correlation curve still shows sufficiently small error deviations and little noise, allowing a meaningful evaluation. The amplitude is about 17, which corresponds to a mean particle number of ≈ 0.06 in the effective detection volume. The confocal plate reader does indeed measure fluorescence fluctuation events caused by single molecules traversing the detection volume with high reproducibility. We now focus on the model fit using equation 2.52. Because the exact axial to radial ratio r of the optics is not known at this point, we must estimate it. Since, the FCS is insensitive

to large r (see section 4.2) and a divergence of r for unconstrainted fitting (see section 2.2.3) is expected, we can estimate a ratio of $r = 20$ without introducing large errors. Subplot C shows the mean particle number $\langle N \rangle$ of the dilution series recorded at different excitation powers. Only a slight increase in the mean particle numbers for increasing excitation powers is observable and the relationship between the weighted mean particle numbers of each dilution step and the concentration can be well described by a straight line. Subplot D shows the mean diffusion times from the FCS analysis. The diffusion times for all excitation powers are superimposed. Visually, no significant difference between the measurement series can be detected and the mean diffusion times remain nearly constant over the whole concentration range. Since the results in subplot C and D show only minor deviations in the results, the excitation powers used are adequate for the Alexa Fluor 488 measurements.

The confocal plate reader automatically performs FFS measurements and shows only small deviations between the measurements for the selected excitation powers, meanwhile exhibiting single-molecule precision. We therefore proceed with the calibration of the measurement optics.

Calibration

The calibration of the confocal plate reader aims to determine the geometric dimensions of the effective detection volume. This information is important for two reasons. First, the exact volume is needed for the concentration determination of the molecule under study. Second, the dimensions of the detection volume give a ratio r that is used in the FCS and mSMR models.
To determine the geometrical parameters of the measurement system, we start with the line fit in subplot C of figure 5.1. The slope provides the information required to determine the effective detection volume of the system, which is given by:

$$V_{\text{eff}} = \frac{\langle N \rangle}{N_{\text{A}}\, C}, \tag{5.1}$$

with N_{A} as Avogadro constant ($N_{\text{A}} = 6.022 \times 10^{23}\,\text{mol}^{-1}$) and C as sample concentration in molar units. We reshape equation 5.1 to express the effective detection volume as a function of the slope:

$$\langle N \rangle = (V_{\text{eff}} N_{\text{A}})\, C. \tag{5.2}$$

From equation 5.2, with $V_{\text{eff}} N_{\text{A}} = 4.1 \times 10^{-3}\,\text{l/pmol}$, we get $V_{\text{eff}} = 7\,\text{fl}$. This method is appropriate even the geometric dimensions of the effective detection volume are unknown, since they have no effect on the amplitude of the FCS curves. In the next step, the geometric ratio $r = \frac{z_0}{r_0}$ is determined. Since the FCS model cannot resolve r well and since r tends to diverge during the fitting routine, the mean diffusion time is used. For an estimated $r = 20$, the results in subplot D in figure 5.1 give $\tau_{\text{D}} = 9.7 \times 10^{-2}\,\text{ms}$. Alexa Fluor 488 has diffusion coefficient of $435\,\mu\text{m}^2/\text{s}$ [89, p. 1442]. With equation 2.48, a known lateral expension $r_0 = 0.4\,\mu\text{m}$ and the effective detection volume 2.47, an axial expension of $z_0 = 7.9\,\mu\text{m}$ is calculated, yielding $r = \frac{z_0}{r_0} = 19.8$. This is close to the originally estimated value. In case of significantly larger deviations, the above calibration procedure must be repeated with the new estimator for r. The final results of the calibration are summarized in table 5.2.

Table 5.2: Calibration results

Parameter	Value
V_{eff}	7 fl
r_0	0.4 µm
z_0	7.9 µm
r	19.8

The confocal plate reader reliably and reproducibly performs measurements at the single-molecule level. The system is calibrated and thus readily available for further studies.

5.3 The mSMR under real measurement conditions

It is time to apply the SMR method on real fluorescence fluctuation data. Section 4.3 already showed the models suitablility for the analysis of simulated data traces. However, only artificially generated measurement artefacts are considered so far. Hence, real measurement artefacts will be addressed in the following.

5.3.1 Detector artefacts

Using the Alexa Fluor 488 dilution series recorded at 30 µW in section 5.2 for the calibration, we begin studying the measurement artefacts. From the fluorescence traces, the mSMR is calculated according to section 3.3.2. The data points are successively corrected for detector dead time, afterpulsing and uncorrelated background noise, which can be viewed in figure 5.2. Subplot A displays the raw mSMR curves of the dilution series. The amplitudes of the mSMR curves differ. For lower concentrations, the amplitudes are significantly lower than for the higher concentrations. In addition, the curve progressions at small sampling times differ. In contrast to the simulated data, no clear plateau is formed for small T. We start with the correction of the detector dead time. The manufacturer of the detector specifies a value of 70 ns for the detector dead time. Equations 3.30 and 3.31 correct the first two moments of the photon counts for detector dead time with $t = 70\,\text{ns}$ and $P_A = 0$. Subplot B shows the results. The change in the curves is subtle, since moderate laser powers and moderate concentrations are used. Despite this, a slight exponential increase occurs in all data sets at small sampling times. The correction illustrates the reducing effect of detector dead time on Mandel's Q parameter and thus on the mSMR. This leads to an underestimation of the mSMR at high photon count rates. Both high laser powers and high concentrations worsen the effect. For very high count rates the dead time starts to dominate and prevents, a meaningful evaluation of the mSMR. In the next step, afterpulsing is additionally corrected. For our detector, we estimate an afterpulsing probability of 0.6 % which is a bit below the manufacturer's specification ($< 1\,\%$). Subplot C shows the correction results using equation 3.30 and 3.31 with $t = 70\,\text{ns}$ and $P_A = 0.006$. Now, both afterpulsing and dead time are corrected in the data set. A comparable increase for short sampling times is now visible for all data series. The part of the afterpulsing that leads to an apparent increase of the Q parameter is eliminated. The remaining exponential decay at short sampling times is caused by photokinetic effects, which were not modelled by the

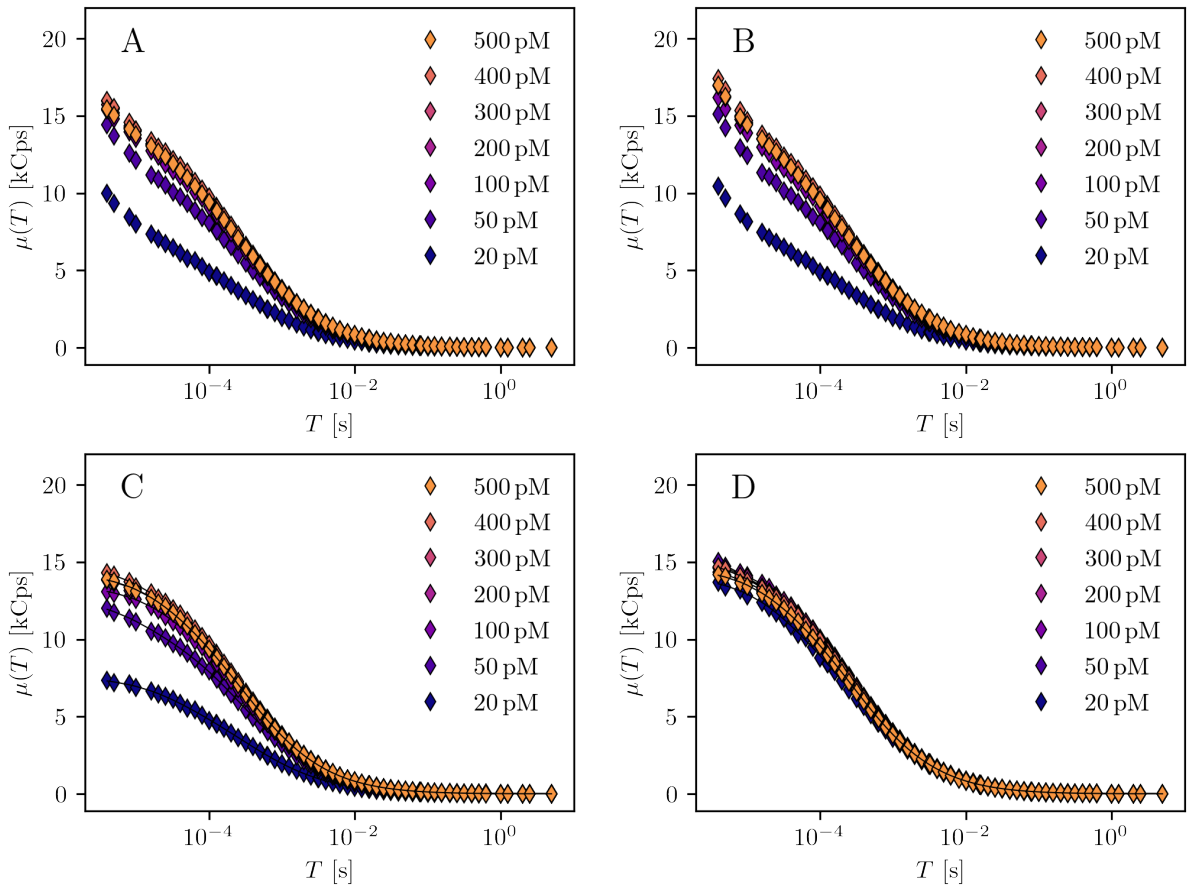

Figure 5.2: Stepwise correction of the mSMR data. Dilution series of Alexa Fluor 488 excited at 30 µW. **A** Uncorrected data from the evaluation. **B** Dead time corrected data. **C** Dead time and afterpulsing corrected data fitted with equation 2.78. **D** Dead time and afterpulsing corrected data with correction of background noise using equation 3.36. Data are fitted with equation 2.78.

simulation engine. The data points can be accurately fitted with equation 2.78, which also includes triplet state transitions. In the last step we correct the data series for background noise using equation 3.37. The background noise is determined by a blank measurement giving 0.5 kCps. Subplot D shows the fully corrected mSMR results. By correcting for detector dead time, afterpulsing, and background noise, the data points of all concentration steps are in nearly perfect alignment. The fit of the data points using equation 2.81 is also included. This result is consistent with the observations from the previous simulations. Since the mSMR only responds to the single-molecule brightness rate and not to the concentration.

After correction, the mSMR analysis of a Alexa Fluor 488 dilution series yields comparable results for all concentration steps. This shows the importance to correct the detector artefacts afterpulsing and detector dead time as well as background noise. In practice, it is not important whether the mSMR curves are corrected for background noise, or whether the fitting results are corrected for background noise. For better illustration, however, a direct correction of the mSMR curves is more meaningful.

5.3.2 Visual comparison of FCS and mSMR

The following section addresses the question of how the mSMR method performs in comparison to the FCS method. This is done on two levels, visually and statistically. First, the models are compared visually, while distinguishing between the diffusive part and the triplet part.

Diffusion model

To visually compare the diffusion models of mSMR to FCS, we use the same data set as in section 5.2 for evaluation and calibration. The mSMR is calculated according to section 3.3.2 on the fluorescence traces of the dilution series and the measurement artefacts are corrected. Figure 5.3, subplot A shows the single-molecule brightness rates μ_0 from the mSMR analysis. A clear relation between the single molecule brightness rate and the

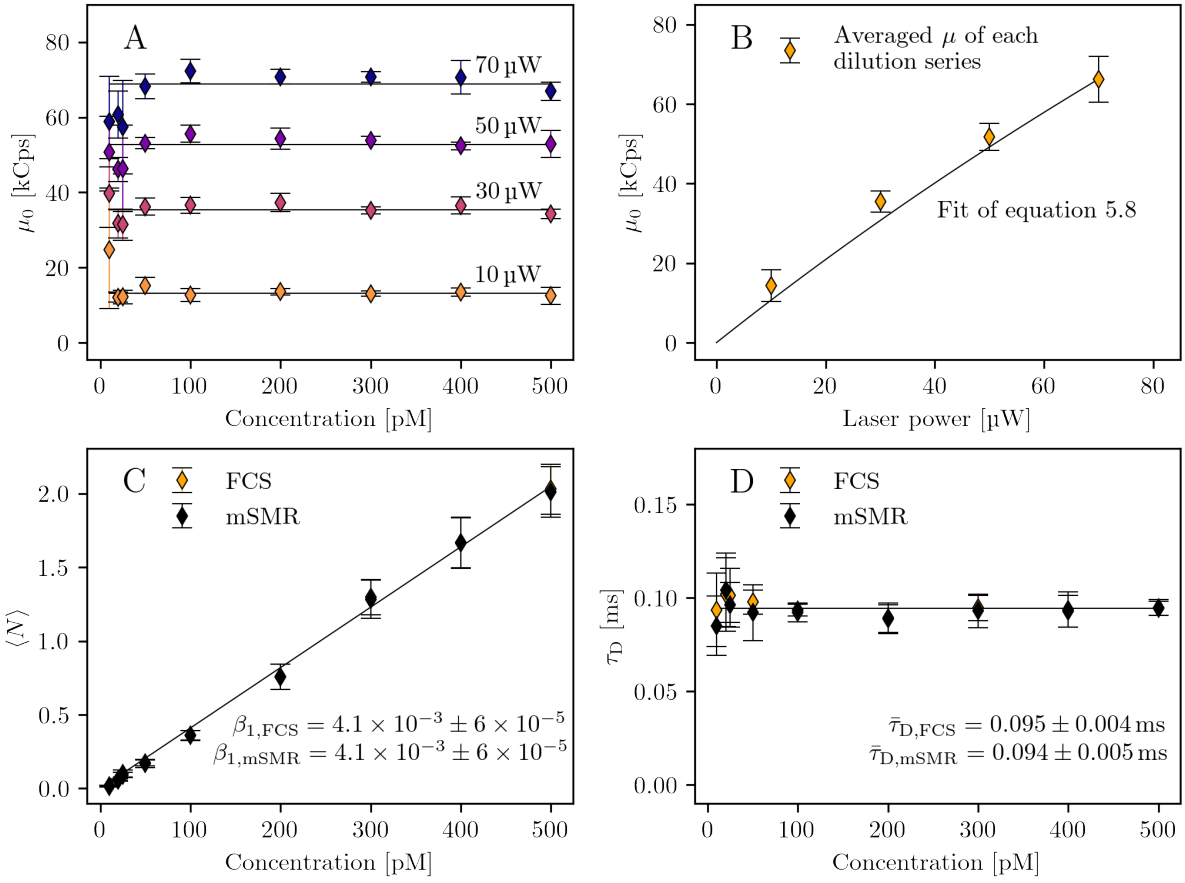

Figure 5.3: The mSMR on real measurement data. For better comparability, we use the data set from section 5.2 obtained from Alexa Fluor 488 dilution series. **A** The single-molecule brightness rate from the dilution series for varying excitation powers. **B** The averaged single-molecule brightness rate of each dilution series as a function of excitation power. The data are fitted with equation 5.8. **C** The averaged mean particle number in the detection volume of all excitation powers from FCS analysis compared to the mean particle number from mSMR analysis derived from single-molecule brightness rates. The straight line fit for both data series goes through the origin. **D** The averaged mean diffusion times τ_D from FCS analysis compared to results from mSMR analysis for all excitation powers.

excitation power is visible. For concentrations $> 50\,\mathrm{pM}$ almost constant single-molecule brightness rates are received for the respective excitation power. At lower concentrations,

however, the data are significantly noisier. To take a closer look at the relationship between single-molecule brightness rate and excitation power, the μ_0 of each dilution series are averaged (subplot B). μ_0 increases sublinearly as a function of excitation power. The fluorescence model 2.8 can be used to describe the data. To apply the model, the excitation intensity must be first converted to the excitation power. For this, we assume a Gaussian profile for the intensity distribution in polar coordinates.

$$I(r,z) = I_0 \left(\frac{r_0}{r(z)}\right)^2 e^{\left(\frac{-2r^2}{r(z)^2}\right)} \tag{5.3}$$

with I_0 being the amplitude of the internsity at the center of the beam and being z the propagation direction of the beam along the axis. $r(z)$ is the radius at which the intensity decrease to $\frac{1}{e^2}$ of their axial values. $r_0 = r(0)$ is the waist radius. $r(z)$ is given by

$$r(z) = r_0 \sqrt{1 + \left(\frac{z}{z_\mathrm{R}}\right)^2}. \tag{5.4}$$

$z_\mathrm{R} = \frac{\pi r_0^2 n}{\lambda}$ is the *Rayleigh range*, with the wavelength λ and the index of refraction n. The integral over the cross-sectional area traversed by the laser beam gives the excitation power. Thus, we consider the area passed through at $z = 0$, so that $r(0) = r_0$ applies.

$$P = \int_0^{+\infty} I(r,0)\,\mathrm{d}A = 2\pi \int_0^{+\infty} I(r,0)\, r\,\mathrm{d}r \tag{5.5}$$

The integral can be understood as a sum of infinitesimally thin tubes. The solution gives as an analytical expression for the relationship between the excitation power and the excitation intensity.

$$\begin{aligned} P &= \frac{I_\mathrm{exc}\pi r_0^2}{2} \\ \Leftrightarrow I_\mathrm{exc} &= \frac{2P}{\pi r_0^2}. \end{aligned} \tag{5.6}$$

Inserting the derived equation 5.6 into equation 2.8 from the theory section 2.1, gives:

$$F(P) = \frac{C\,k_\mathrm{fl}}{1+Q} \frac{\frac{2P}{\pi r_0^2 I_\mathrm{s}}}{1 + \frac{2P}{\pi r_0^2 I_\mathrm{s}}} \tag{5.7}$$

In this expression, with the photokinetic parameters of Alexa Fluor 488 from table 2.1 and with the calibration results in table 5.2, all quantities except the parameter C are known. Assuming the fluorescence rate and the single-molecule brightness rate to be proportional, yields the following expression:

$$\mu_0(P) = \frac{C'\,k_\mathrm{fl}}{1+Q} \frac{\frac{2P}{\pi r_0^2 I_\mathrm{s}}}{1 + \frac{2P}{\pi r_0^2 I_\mathrm{s}}}. \tag{5.8}$$

For $C' = 4.00 \times 10^{-6}\,\mathrm{kC}$, equation 5.8 gives a good description of our data and provides a link between theory and experiment. The results of the amplitudes of the two models are to be compared. Since the mSMR analysis provides the single-molecule brightness rate, it

must be converted to the average particle number in the effective detection volume. The relation is given by:

$$\langle N \rangle = \frac{\langle k \rangle}{\mu_0} \frac{1}{\gamma_2}. \tag{5.9}$$

The average count rates $\langle k \rangle$ are depicted in figure 5.1. Because of a different definition of the effective detection volume in the models, a scaling factor of $\gamma_2 = 2^{-3/2}$ is needed for comparison. Subplot C shows the mean particle numbers from FCS and mSMR analysis. Both models give essentially the same results for $\langle N \rangle$. By fitting the data with a straight line and calculating the standard error of the slope via

$$\sigma_{\beta_1} = \sqrt{\frac{\sum_i^n (\hat{y}_i - y_i)^2}{n-2}} \sqrt{\frac{1}{\sum_i^n (x_i - \bar{x})^2}}, \tag{5.10}$$

the flollowing slopes and standard errors are obtained for the two models:

$$\beta_{1,\mathrm{FCS}} = 410 \pm 6\,\mu\mathrm{M}^{-1},$$
$$\beta_{1,\mathrm{mSMR}} = 407 \pm 6\,\mu\mathrm{M}^{-1}.$$

There is no difference observable in the slopes, which initially does not allow any distinction between the models. Now the temporal changes are to be studied, i.e., the diffusion times. The data are directly comparable and displayed in subplot D. For concentrations $> 50\,\mathrm{pM}$, almost constant diffusion times can be seen. At small concentrations, fine differences appear and the standard deviations increase. Averaged over all concentration steps, the follwing mean diffusion time are retrieved:

$$\bar{\tau}_{\mathrm{D,FCS}} = 0.095 \pm 0.004\,\mu\mathrm{s},$$
$$\bar{\tau}_{\mathrm{D,mSMR}} = 0.094 \pm 0.005\,\mu\mathrm{s}.$$

Here too, no difference in the results of the mSMR and FCS analysis can be stated. The statistical comparison in section 5.3.3 will show if this holds for a larger data set. But before, triplet effects are visually considered.

Triplet model

To compare triplet state characteristics in the mSMR and FCS models, we take a power series of an Alexa Fluor 488 solution of 500 pM concentration. By gradually increasing the excitation power, the effects of the triplet state should become more apparent. The excitation powers are 50, 60, 70, 80, 90, 100, 110, 120 ,130 and 140 µW. We evaluate the fluorescence traces using the FCS and mSMR and perform the corrections as described in section 5.3.1. Figure 5.4 shows the results of the analysis. In subplot A displays mSMR curves at different excitation powers. The amplitudes of the curves increase for higher powers. To better visualize the triplet components of the curves, the mSMR curves are divided by the diffusive part.

$$\Gamma_{\mathrm{trip}}(T) = \frac{\mu(T)}{\Gamma_{\mathrm{diff}}(T)} \tag{5.11}$$

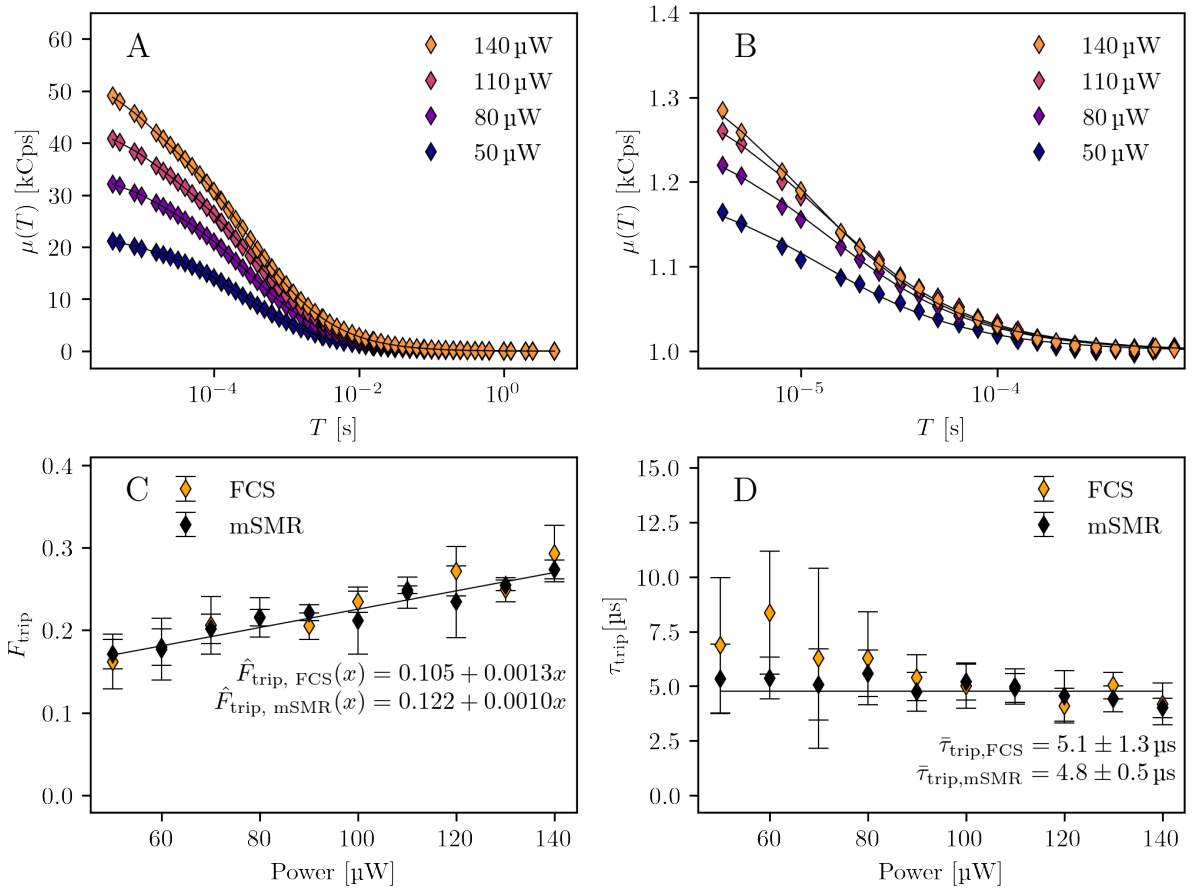

Figure 5.4: The triplet effect in real measurements. A power series is conducted on an Alexa Fluor 488 sample with 500 pM concentration. **A** mSMR curves for the laser powers 50 µW, 80 µW, 110 µW and 140 µW. **B** Division of the data series from subplot A by the diffusive term Γ_{diff} of the mSMR model to get the triplet term Γ_{trip} of the data. **C** Triplet part F_{trip} from the model fit of the FCS and mSMR analysis. The solid line represents a fit of the mSMR results with a straight line. **D** Triplet decay rate τ_{trip} from the model fit of the FCS and the mSMR analysis. The solid line indicates the weighted average of the relaxation times from the mSMR model over all studied excitation powers.

This step yields the triplet component of the original data series, shown in subplot B. In this representation, the increase of the triplet fractions F_{trip} as a function of excitation power is evident. At larger excitation powers, a fluorophore undergoes more excitation/relaxation cycles, which raises the electron's probability of transitioning from the short-lived S_1 state to the long-lived triplet state T_1 (compare figure 2.1). Subplot C illustrates this relationship. The dark triplet fraction F_{trip} and excitation power show an almost linear relationship. For comparison, the results of the FCS analysis are also included. Visually, there is no significant difference in the results of the two models, but the line fit shows slight distinctions:

$$\hat{F}_{\text{trip, FCS}}(x) = 0.105 + 0.0013x,$$
$$\hat{F}_{\text{trip, mSMR}}(x) = 0.122 + 0.0010x.$$

Subplot D shows the relaxation times τ_{trip} from the triplet models. Over the examined excitation powers, the relaxation times for the mSMR model are almost constant, whereas the FCS model provides somewhat larger relaxation times and stronger deviations at low

excitation powers. The weighted means and corresponding standard deviations are:

$$\bar{\tau}_{\text{trip,FCS}} = 5.1 \pm 1.3\,\mu\text{s},$$
$$\bar{\tau}_{\text{trip,mSMR}} = 4.8 \pm 0.5\,\mu\text{s}.$$

The results show that the mSMR model reproduces well the photokinetic effect of the triplet transition. Thereby, the mSMR visually exhibits good comparability to the FCS results. For the relaxation times, the mSMR method demonstrates consistent results over even a wider range of excitation powers.

5.3.3 Statistical comparison of FCS and mSMR

This section address the question of whether statistically robust differences can be found between the FCS and mSMR models. The previous results in section 5.3.2 showed visually no differences in the diffusion model Γ_{diff}. Whereas the triplet model Γ_{trip}in section 5.3.2 indicated some differences. We will now examine whether these observations stand up to statistical analysis.
The data basis for the comparison are measurements on 50 pM Alexa Fluor 488 solutions at excitation powers of 10, 30, 50 and 70 µW. All fluorescence traces are evaluated with the mSMR and the FCS method. The results of the five-fold measurements of each well are averaged to get a total set of 39 data points. To begin with, the parameters are tested for normal distribution. For this, the Z-scores are calculated using equation 3.52 and a *Kolmogorov-Smirnov* test for normal distribution is performed. The null hypothesis H_0 is that theobserved distributions correspond to a normal distribution ($\bar{\mu} = 0$, $\sigma = 1$). The statistical significance is in all cases $\alpha = 0.05$. To compare the mean particle numbers, the single-molecule brightness rates μ_0 of the mSMR are first converted to the mean particle numbers using equation 5.9. For the remaining parameters (τ_{D}, F_{trip}, τ_{trip}), no conversion is necessary and the Z-scores can be calculated directly. All test statistics can be found in tables 10.1 and 10.2 in the appendix. According to the *Kolmogorov-Smirnov* test, the assumption of normally distributed papameters is justified in all cases and the variances and means of the parameters can be further analyzed. The *Brown-Forsythe* test is suitable for studying variances [106]. It verifies whether the sample variances differ significantly. The null hypotheis is that there is no significant difference between the variances. To compare the mean values of the two models, *Welch's* t-test is used [107]. Unlike the standard t-test, *Welch's* t-test does not require homoscedasticity and seems to be more robust for the given issue. Again, the null hypothesis is that there is no significant difference between the means of the models. The summarized results of the comparison can be seen in figure 5.5. Starting with the results of the diffusive part of the FCS and mSMR analysis, subplot A shows the mean particle numbers for different excitation powers. There is practically no difference between the models, and for both the variance and the mean, no statistically significant differences are found. However, a slight increase in the mean particle number is pronounced with increasing excitation powers in both models. A similar picture emerges for the mean diffusion times in subplot B. The variances and the mean values do not differ significantly between the two models. Here too, a slight increase in the mean diffusion time is observed with increasing excitation powers. In the following, the results of the triplet part of the models will be addressed. Subplot C shows the triplet fractions F_{trip}. A distinct difference between the two models appears, with the results converging at larger excitation powers. The statistical analysis shows a significant difference in both the variances and the means of the triplet fractions,

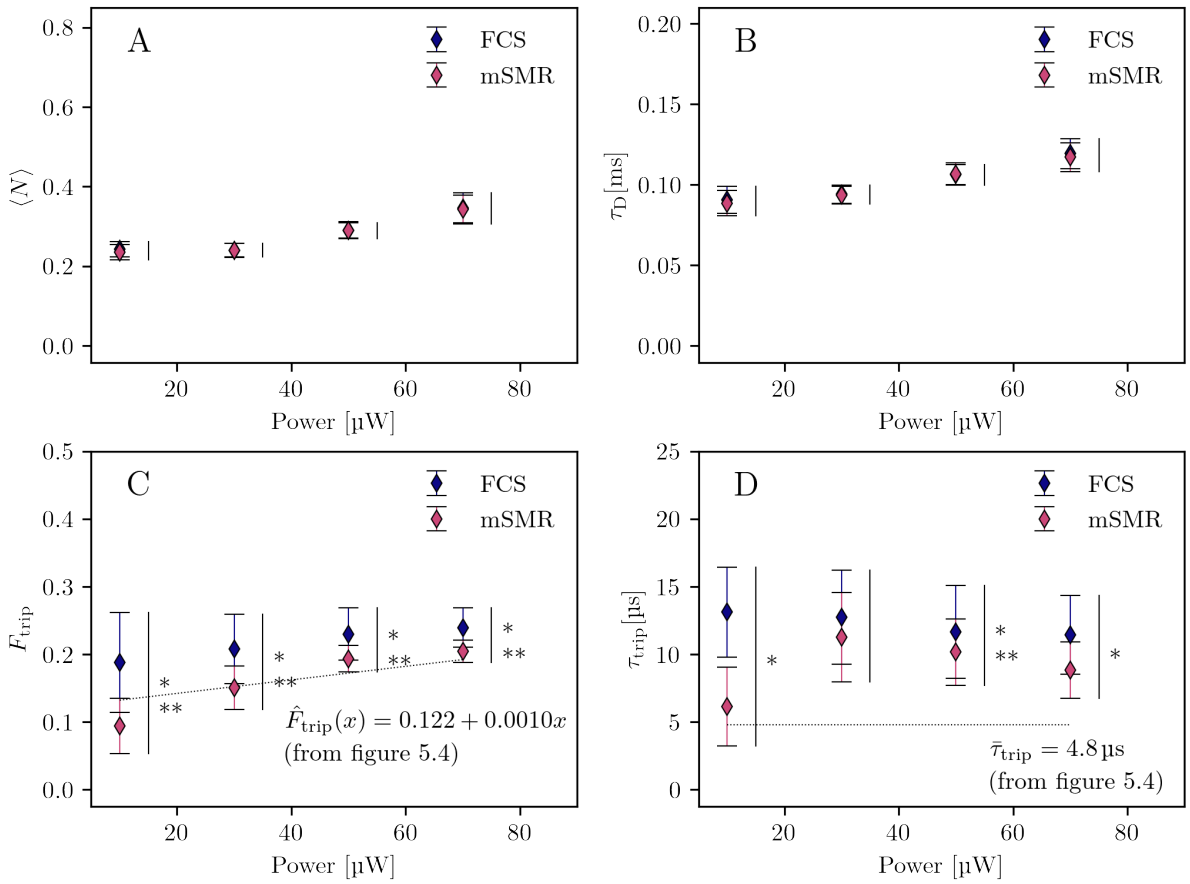

Figure 5.5: Statistical comparison of the FCS and mSMR models. Measurements are conducted on 50 pM Alexa Fluor 488 solutions at varying excitation powers. 39 wells are measured at 5 positions. The variances and means of each fitting paprameter are statistically analyzed ($\alpha = 0.05$). The asterix ($*$) indicates significant differences in the means and ($**$) shows significant differences in the variances between the models. **A** Mean particle numbers $\langle N \rangle$ of the diffusive part Γ_{diff}. **B** Mean diffusion times τ_D of the diffusive part Γ_{diff}. **C** Triplet fractions F_{trip} of the triplet part Γ_{trip}. The line fit from figure 5.4 subplot C is shown. **D** Relaxation times τ_{trip} of the triplet part Γ_{trip}. Also, the mean relaxation time from figure 5.4 subplot D is included.

which persists even at the highest excitation power studied. While the mSMR results show a good agreement with the results from section 5.3.2, the FCS results are clearly too high. Finally, in subplot D the relaxation times τ_{trip} from the fits are given. The relaxation times from the FCS analysis are significantly larger for 10, 50 and 70 µW compared to the mSMR analysis, whereas the variances only differ significantly in the 50 µW measurement. Interestingly, the relaxation times in this setting are significantly higher than the results found in section 5.3.2. However, it can be seen that the difference is less pronounced for the mSMR results than for the FCS results.

In addition to the accuracy of the analysis results, the performance of a method plays an important role in practice. When computing the mSMR and FCS analyses for statistical comparison, the calculation times were also recorded. Table 5.3 shows the summary of the computation times. In this work, the autocorrelation curves of FCS are calculated via multiplication in Fourier space as described in section 3.3.1. For mSMR analysis, a fluorescence trace is divided into increasing bins for which the moments are calculated as described in section 3.3.2. The measurements in table

Table 5.3: Computation times of the FCS and mSMR analyses.

Exc. power [µW]	Time FCS [ms]	Time mSMR [ms]
10	1371 ± 38	244 ± 14
30	1411 ± 84	258 ± 19
50	1379 ± 54	243 ± 15
70	1383 ± 26	242 ± 14

5.3 show a 5.6× speedup for our mSMR implementation compared to the FCS calculation.

In general, the two models show no significant difference in mean particle number and mean diffusion time. However, when looking at the events at short time scales, slight differences between the two models are noticeable. This leads to slightly higher triplet fractions and relaxation times being obtained for the FCS model than for the mSMR model. Another interesting aspect of the mSMR is that it is much faster to compute than the FCS.

5.4 Discussion

The results of this chapter are discussed in more detail with respect to the initial objectives: the evaluation and calibration of the confocal plate reader, and the application of the mSMR model on real measured fluctuation data.
The results of the evaluation and calibration of the home-built confocal plate reader reveal several important points. First, the results confirm the correct operation of the confocal plate reader. From the small error bars of the count rates, we can deduce the high repeatability of the system (see figure 5.1, subplot A). This is also confirmed by the FCS analyses. After correcting for background noise, concentrations of $< 200\,\text{pM}$ give mean particle counts of less than one in the detection volume (see figure 5.1, subplot B). At the same time, the autocorrelation curves show little noise under the given experimental parameters. We can thus conclude that we are indeed analyzing single-molecule events with the home-built confocal plate reader. Second, looking at the results from data fitting, a straight line is given for the mean particle number of the dilution series (see figure 5.1, subplot C). Meanwhile the mean diffusion times are nearly constant over the whole concentration range (see figure 5.1, subplot D), although larger deviations can be observed at small concentrations. These can be attributed to poorer statistics because of few photon events. The findings suggest that the excitation powers used are appropriate for the study of Alexa 488. If the excitation powers were too high, we would have expected significant deviations from the linear relationship in the mean number of particles or from the constant level of the mean diffusion times. Third, the calibration gives an effective detection volume of 7 fl and a geometric ratio of axial to radial extent of $r = 19.8$ for the used optics. These values are significantly larger than usual for FFS experiments, where a volume of approximately 1 fl [53, p. 10] and a geometric ratio of $1 < r < 10$ is expected. This elongation of the detection volume can be attributed to the long-distance objective lens (LD, 63x, NA = 0.75). For such an optic, we would expect a prolonged extension of the observation volume in z-direction . Fourth, the numerical apperture of the long-distance lens is lower than with commonly used immersion objectives. In the literature, numeric appertures of >0.9 are recommended for FFS experiments [53, p. 5]. However, the results from the calibration show that the

confocal plate reader delivers accurate results at the single-molecule level. At the same time, the use of the long-distance air objective offers great advantages in the automation of the confocal plate reader, enabling the reader to scan a standard microplate with little effort. This would not be feasible with an immersion objective. In summary, the calibration results show that the confocal plate reader reliably enables the collection of fluorescence fluctuation data while also allowing experiments at the single-molecule level. After calibration, the fluorescence traces were also evaluated using the mSMR. In the mSMR analysis, the influence of detector and measurement artefacts is evident (compare figure 5.2). At short sampling times, afterpulsing and detector dead time overlay the mSMR data. Detector dead time plays a minor role at the low excitation rates used in this experiment. Afterpulsing, on the other hand, should always be considered in the case of a single detection channel. For the practical application it is important to see that a complete correction of the measurement artefacts is possible. In the present case, the mSMR data could be brought into alignment for a wide concentration range. An extension of the mSMR model to two detection channels, which should completely supress the effect of afterpulsing [85, p. 3], is an interesting issue that should be addressed in follow-up work.

Now the comparison of the FCS and mSMR models in real experiments are discussed. First we focus on the diffusive part of the models. The results from the visual analysis and the statistical analysis give a consistent picture. Visually, the mean particle numbers $\langle N \rangle$ did not differ significantly between the models (compare figure 5.3, subplot C). This observation is consistent with the results of the statistical analysis in section 5.3.3, which also shows no difference in $\langle N \rangle$ between the models. The same observation applies for the mean diffusion time τ_{D} (see figure 5.3, subplot B). In the visual comparison of the models, we could only detect differences between the models at very low concentrations. The statistical comparison confirms this observation since no significant differences between in the diffusion times could be found. Figure 5.5 indicates that the mean particle numbers and the mean diffusion times in both models slightly increase for higher excitation powers. This effect has already been discussed in the literature and is most likely caused by fluorescence saturation [64, p. 47-49]. Due to fluorescence saturation, the emission intensity and excitation intensity are no longer proportional to each other, resulting in a deviation of the *molecular detection efficiency* (MDE) from a Gaussian ellipsoid (see section 2.2.4). The FCS and mSMR models assume an ideal Gaussian profile, which means that they can no longer reliably represent the case of fluorescence saturation, leading to the observed deviations in mean particle number and diffusion time.

Of particular interest is the comparison of the models for the description of photokinetic effects at short-time scales. For this, the results of the triplet models are compared. From figure 5.4 it is visually evident that for excitation powers $\geq 50\,\mu\mathrm{W}$ the triplet fractions F_{trip} are comparable for both models. This statement is not tenable at low excitation powers. The statistical analysis showed that the mSMR model differs significantly from the FCS both in terms of variance and mean value. At higher excitation powers, the results of the models converge, but the differences remain statistically significant. The results of the mSMR model in the statistical analysis can be described by the same regression line as the F_{trip} data from the visual analysis (see figure 5.5, subplot C). Moreover, the statistical analysis shows smaller variances for the mSMR model. These findings support the strength of mSMR model to describe photokinetic effects. Looking at the relaxation times τ_{trip}, we found a mean relaxation time for Alexa Fluor 488 of

$\tau_{\text{trip}} = 4.8 \pm 0.5\,\mu\text{s}$, which is in good agreement with literature ($\tau_{\text{trip}} = 4.2 \pm 0.8\,\mu\text{s}$) [108, p. 10187]. For FCS analysis, we got a higher relaxation time with larger standard deviation: $\tau_{\text{trip}} = 5.1 \pm 1.3\,\mu\text{s}$. Interestingly, the overall relaxation times are significantly larger in the statistical analysis than in the visual observation. Since very low concentrations and excitation powers were used in the statistical analysis, these seem to have a detrimental effect on the relaxation times. However, the relaxation times obtained from the mSMR model are still significantly lower and therefore more plausible than for the FCS model.
The results indicate an advantage of the mSMR model over the FCS model in the analysis of photokinetic effects. In further work, it would certainly be interesting to repeat the statistical analyses with additional dye systems. Here, studies on fluorescein, rhodamine 6G, Cy5 or the green fluorescent protein (GFP) are promising.

In summary, the following points can be stated. The home-built confocal plate reader performs automated and reliable FFS measurements at the single molecule level. It thus provides valuable support for the collection of FFS data. In addition, the FCS and mSMR models are in good agreement and no differences could be found in the results of the diffusive model. When comparing the results at short-time scales (i.e., the triplet model), significant differences can be observed. Here the mSMR model gives more plausible results, which is probably due to the correction of detector artefacts. Finally, the mSMR curves can be computed significantly faster than the autocorrelations of FCS (about 5.6× faster). This is a great advantage if data is analyzed over a longer period or if shorter samplings are considered to better represent photokinetic effects.

6 The characterization of nucleic acid mixtures using the mSMR

In the following, the mSMR analysis is applied to a more complex biological system. An interesting case is the characterization and quantification of DNA mixtures, since many applications rely on accurate information about the composition of the samples under study. For example, molecular methods such as cloning require accurate concentration information for high step efficiency [109]. Similarly, the analysis of cellular expression patterns or the examination of tissue samples rely on accurate concentration data [110, 111, 112, 113]. Of particular interest, however, is DNA sequencing using next generation sequencing (NGS) methods. In the most widely used method, a sample is processed over several steps to generate a NGS library, which includes fragmentizing the sample and ligating adaptors to the 5' and 3' ends of the fragments. The result is called a sequencing or NGS library. The library is loaded onto a flow chip, where each of the fragments forms its own cluster via bridge amplification. Subsequently, stepwise sequencing of the fragments takes place using fluorescent markers labeled in four colors. The light signal of each cluster is read out, providing parallel sequence information of the fragments. These overlapping sequences of the fragments are then assembled into the overall sequence during the step of sequence alignment [114, p. 4-5]. For accurate and cost-efficient sequencing results, precise quantification of the NGS library is necessary to prevent suboptimal loading of the flow chip [115, p. 6-7]. Usually, the mass concentration is determined via fluorometry and the fragment length distribution of the library via capillary electrophoresis. Then, the average fragment length of the sequencing library is calculated from the fragment length distribution. From the mass concentration and the average fragment length, the molarity of the sample can be estimated. So far, however, no gold standard exists for the quantification of NGS libraries, so various methods are used [115, p. 1][116, p. 1].
Fluorescence fluctuation spectroscopy provides a good approach for the characterization of unknown nucleic acid mixtures. There are several fluorescent dyes that intercalate with nucleic acids sequence-independently, enabling reliable labeling [117, p. 3015][118, p. 1196]. In addition, quality control should consume as little of the precious sample material as feasible [115, p. 5-7], so highly dilute solutions in smallest quantities are prefered. FFS experiments require exactly these conditions to address the characterization of nucleic acid mixtures. We will start with the analysis of DNA mixtures consisting of defined DNA fragments using the mSMR method. The relationship between single-molecule brightness rate and DNA fragment length is examined, as are diffusion properties. The results of the diffusion properties are compared with data from the literature as well as with a theoretical model. Since the FFS theory assumes point-like particles, but DNA is a multi-labeled filamentous polymer, the consequence on the average particle numbers for DNA mixtures will be analyzed in more detail and compared with the theoretically expected concentrations. Then, photokinetic effects are considered. The influence of isomerization as a function of fragment length is explored, as is the distinction from the

triplet state. Finally, the effect of photobleaching on the fluorescence intensities of the mixtures is studied. Based on these findings, we will analyze sequencing libraries and attempt to characterize these heterogeneous mixtures. Parts of this chapter were previously published in Sparrenberg et al. [54, 24].

6.1 Experimental procedure

The characterization measurements in section 6.2.1 of this chapter are performed on DNA solutions of defined composition using our home-built confocal plate reader. Table 6.1 summarizes the measurement parameter. Dilution series are prepared for the following DNA fragments: 50, 100, 200, 300, 500, 700 and 1000 bp (NoLimits, Thermofisher, USA). As a solvent, we use 25 % DMSO/75 % water (v/v) to break up any tertiary structures and prevent the formation of larger DNA aggregates. As staining solution, a mixture of 997 µL TE buffer and 3 µL RiboGreen (Quant-iT RiboGreen, Thermofisher, USA) is prepared. The fluorescent dye RiboGreen intercalates with all types of nucleic acids and convinced in preliminary experiments by featuring an excellent brightness. Prior to measurement, DNA mixtures and staining solution are added in equal volume fractions and allowed to equilibrate for 2 h. The final concentrations after staining are 0, 8, 20, 40, 80, 120 and 160 pg/µL. 20 µL of each concentration step are loaded onto the microtiter

Table 6.1: Measurement parameters of DNA mixure studies.

Sample preparation	
Microtiter plate	384 well (μclear, non-binding, Greiner BioOne, Germany)
Staining dye	RiboGreen (Quant-iT RiboGreen, Thermofisher, USA)
DNA solvent	25 %DMSO/75 % water (v/v)
DNA fragments	50, 100, 200, 300, 500, 700, 1000 bp (NoLimits, Thermofisher, USA)
Concentration steps	0, 8, 20, 40, 80, 120, 160 pM
Sample volume	20 µL
Setup parameters	
Measurement time	10 s
Equilibration time	10 s
Sampling time	1×10^{-6} s
Measurement repeats	5
Laser power	Varied
Excitation light	488 nm
Emission filter	535/50
Objective lens	63x/0.75 LD

plate, which is then sealed with a foil to prevent evaporation. To reduce bleaching effects, the plate reader approaches the focal plane and waits with switched-on laser for 10 s before each measurement to reach an equilibrium of unbleached to bleached particles in the observation volume. For each run, the measurement time is 10 s with a sampling time of 1×10^{-6} s. Each measurement is conducted at five locations in the well. The excitation powers used are specified separately in the results.

For the evaluation measurements in section 6.2.4, the same protocol as above is used. Four externally characterized libraries (Exo, Gen, Lex1, Lex2) are analyzed using the home-built plate reader and the mSMR method. Two libraries (Gen, Lex2) are diluted in four steps using 25 % DMSO/75 % water (v/v). After adding an equal volume of the RiboGreen staining solution, final dilutions steps of 1 : 25, 1 : 50, 1 : 100 are obtained. The other two libraries (Lex1, Exo) are diluted and stained with the same buffers to get a final dilution of 1:20. All samples are incubated for two hours to equilibrate. Before each measurement, the sample is irradiated in the focal plane with switched-on laser for 10 s to ensure an equilibrium of bleached and unbleached particles. Data acquisition is for 10 s with a sampling time of 1×10^{-6} s. Each measurement is repeated 5 times at an excitation power of 2.5 µW.

6.2 mSMR in the analysis of nucleic acid mixtures

Fluorescence fluctuations of DNA mixtures of defined composition are analyzed considering both the comparatively long-lived diffusive parts of the mSMR model and the short-lived photokinetic effects. Then, the findings are applied on DNA sequencing libraries to characterize them.

6.2.1 Characterization of defined DNA mixtures

To begin with, we conduct measurements on DNA dilution series of defined fragment length composition. To reduce photobleaching to a minimum, the fluorescence fluctuations are recorded at an excitation power of 2.5 µW. The derived mSMR curves are corrected for detector artefacts as described in section 5.3.1. Figure 6.1 shows the results of the analysis. Subplot A shows the averaged mSMR curves of the DNA dilution series of defined composition. The curves increase in the amplitudes for larger fragment lengths and a shift towards larger sampling times. In general, the mSMR curves look very smooth and show little variation even for large sampling times. The data are fitted with equation 2.81 including a simple on/off isomerization term. Subplot B shows the averaged single-molecule brightness rates μ_0 from the model fit. As already seen in subplot A, μ_0 increases as a function of the fragment length, which can be well described by a 2nd order polynomial. Looking at the averaged diffusion times of the measurements in subplot C, τ_D increases for growing fragment lengths. To allow a comparison to literature, we convert the diffusion times of the DNA mixtures into diffusion coefficients using equation 2.48. Subplot D depicts the diffusion coefficients in a double-logarithmic representation. In a first approach, the diffusion coefficients are described by a power law.

$$y(x) = \beta_0 \times x^{\beta_1} \tag{6.1}$$

By taking the logarithm transforms this equation into a straight line:

$$\log(y(x)) = \log(\beta_0 \times x^{\beta_1}) = \log(\beta_0) + \beta_1 \log(x). \tag{6.2}$$

The fit yields $\log(\beta_0) = 2.88 \Leftrightarrow \beta_0 = 765$ and $\beta_1 = -0.79$. Using equation 5.10 to calculate the standard error of the slope, we get $\beta_1 = -0.79 \pm 0.02$. A theoretical approach to describe diffusion of DNA molecules is the semiflexible model for diffusing polymers (see section 2.2.6). We estimate the viscosity of the solvent via Alexa Fluor 488 measurements. As for the DNA mixtures, a dye solution of one part 25 % DMSO/75 % water (v/v) and

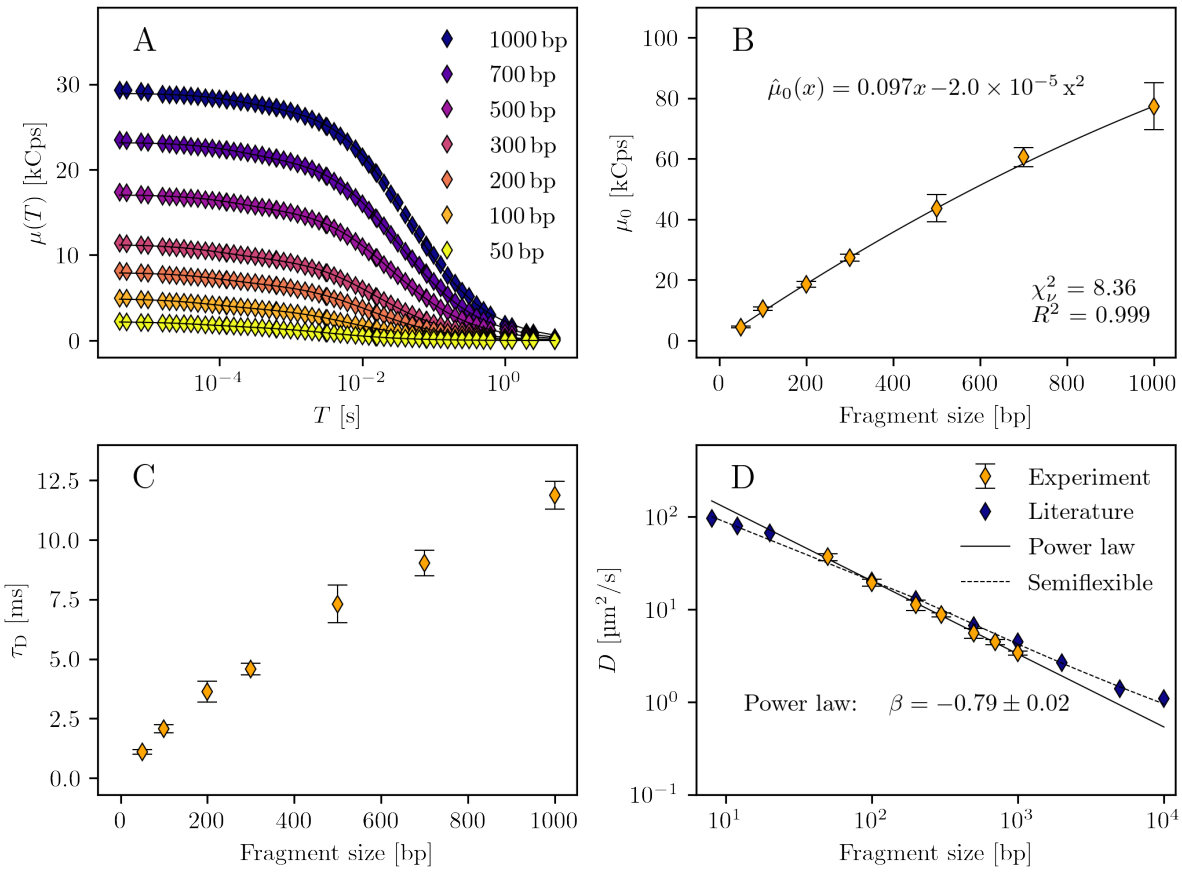

Figure 6.1: mSMR analyses on DNA solutions of defined fragment length. The used laser power is 2.5 µW. **A** Averaged mSMR for DNA dilution series of defined composition. **B** Averaged corrected μ_0 of the DNA dilution series. The data points of 100 to 1000 bp DNA fragment solutions are fitted with a line ($f(x) = \beta_0 + \beta_1 x + \beta_2 x^2$, with $\beta_0 = 0.0$, $\beta_1 = 0.097$ and $\beta_2 = -2.0 \times 10^{-5}$). **C** Averaged diffusion times τ of the DNA dilution series. **D** Averaged diffusion coefficients D of the DNA dilution series in double-logarithmic representation. The data are fitted with a power law ($f(x) = \beta_0 \times x^{\beta_1}$, with $\beta_0 = 765$ and $\beta_1 = -0.79$). In addition, the course of the semiflexible diffusion model is shown (parameters for dsDNA: $l_\mathrm{p} = 51\,\mathrm{nm}$, $d = 2.5\,\mathrm{nm}$, $l_\mathrm{s} = 0.34\,\mathrm{nm/bp}$ and $\Lambda_\mathrm{D} \approx 0.9$ [65, p. 3]). For comparison, data from literature are added ($8 - 20\,\mathrm{bp}$ [119, p. 2327] and $100 - 10\,000\,\mathrm{bp}$ [65, p. 3]). The diffusion coefficients from the literature are corrected to 25 °C and adjusted to the viscosity of the solvent used.

one part TE buffer is prepared. By comparing the diffusion times to measurements in pure water, a 1.8× increase in the diffusion time is observed. From the Stokes-Einstein equation 2.33 and equation 2.48, the proportionality of viscosity and diffusion time can be seen.

$$\eta \propto \tau_\mathrm{D} \tag{6.3}$$

Therefore, the viscosity of the solvent at 25 °C can be estimated as $\eta = 1.8 \times 0.891\,\mathrm{mPas} = 1.60\,\mathrm{mPas}$. This enables us to calculate the semiflexible diffusion model using the parameters in table 6.2. To convert between basepairs and length of the DNA molecule, the inter-base-pair distance l_s is used. For better results, a correction term Λ_D is introduced as a pre-factor of equation 2.35 in the literature [65, p. 3]. The graph of the semiflexible model is added to subplot D and supplemented with diffusion coefficients for oligomers $8 - 20\,\mathrm{bp}$ [119, p. 2327] and larger fragments $100 - 10\,000\,\mathrm{bp}$ [65, p. 3] from literature. The diffusion coefficients are adjusted to 298 K and corrected for viscosity. The theoretical diffusion model for semiflexible chains describes the diffusion coefficients of our diffusion

Table 6.2: Input parameters for the semiflexible diffusion model of dsDNA

Parameter	Value
k_B	$1.380\,648\,52 \times 10^{-23}\,m^2kg\,s^{-2}K^{-1}$
T	298 K
η	1.60 mPas (estimated from Alexa Fluor 488 measurements)
l_p	51 nm [65, p. 3]
d	2.5 nm [65, p. 3]
l_s	0.34 nm/bp [65, p. 3]
Λ_D	0.9 [65, p. 3]

coefficients and of the data from literature. However, it is noticeable that the slope of our diffusion coefficients is somewhat steeper than predicted by the model and the data from literature.

An intriguing question is whether the mSMR model can represent the number of DNA molecules in the effective detection volume. Therefore, the brightness rates are converted to the mean particle numbers for each concentration step of a dilution series via equation 5.9. Figure 6.2 shows the results. In subplot A shows linear increases of the

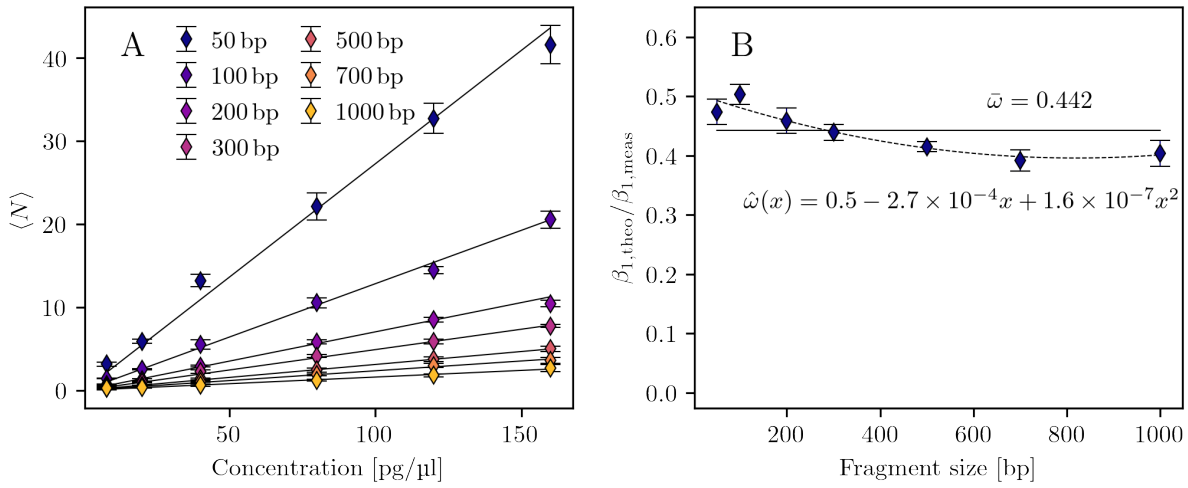

Figure 6.2: The relation of measured particle number to theoretical particle number in DNA solutions. **A** The mean particle number retrieved from mSMR analyses of DNA dilution series. $\langle N \rangle$ was calculated via equation 5.9 from the single-molecule brightness rates μ_0 of the mSMR model. The data are fitted with a line $f(x) = \beta_0 + \beta_1 x$. **B** Ratio ω of theoretical slope $\beta_{1,\mathrm{theo}}$ and measured slope $\beta_{1,\mathrm{meas}}$ of the DNA dilution series. The average weighted ratio of the slopes is $\bar{\omega} = 0.442$. In addition, the data can be empirically described by a second order polynomial.

mean particle number for each DNA dilution series. The data are fitted using a straight lines through the origin. The slopes of the lines increase for shorter fragment lengths, which is expected since the molarity changes antiproportionally to the DNA fragment length for a given mass concentration. To compare the measured particle numbers to the theoretically expected particle numbers, the corresponding molecular weights are estimated from the DNA fragment lenghts using the following relationship [120]:

$$MW \approx 650\,\mathrm{g/mol} \times n, \tag{6.4}$$

with n being the number of base pairs of the DNA molecule. Using the Avogadro constant and the effective detection volume, the theoretical particle number is obtained.

$$\langle N \rangle_{\text{theo}} = \frac{c}{MW} N_{\text{A}} V_{\text{eff}} \tag{6.5}$$

This relation gives the theoretical particle numbers in the effective detection volume for each concentration step of the dilution series. Dividing the theoretical slopes $\beta_{1,\text{theo}}$ by the measured slopes $\beta_{1,\text{meas}}$ of each dilution series gives the ratio ω. Subplot B displays ω as a function of the fragment legth. On average, the ratio is $\bar{\omega} = 0.442$ and thus deviates significantly from the expected ratio of $\omega = 1$. To describe the data more accurately, an empirical second order polynomial is used. Although, it has no physical meaning, it reflects well the discrepancy between measurement and theory.

In summary, DNA solutions of defined composition can be analyzed by means of the mSMR method. Thereby, the fragment length dependent single-molecule brightness rates and diffusion coefficients can be described via theoretical and empirical models. When considering the DNA particle numbers in the detection volume, significant deviations from theoretical appear. But these can be compensated for by an empirical model for the given experimental parameters.

6.2.2 Photokinetic effects in the analysis of DNA mixtures

In the following section, short-lived photokinetic effects in DNA measurements are considered.

Isomerization

DNA fragments are labeled with numerous dye molecules along the chain. Since the dye exhibits blinking behavior, isomerization effects occur. To study isomerization in DNA measurements, we use the data set from the previous section. Because the measurements were taken at only 2.5 µW, triplet state effects are neglected to focus entirely on isomerization. Figure 6.3 shows the results of the analysis. In subplot A displays the isomerization part Γ_{iso} from the averaged mSMR curves in figure 6.1. The mSMR curves are divided by the diffusive part Γ_{diff} of the fitted model 2.79 to get Γ_{iso}. The time axis is scaled to cover the region of interest. The amplitudes of the isomerization fractions decrease significantly with increasing fragment length. Even though the model generally describes the data well, slight variations can be seen. We will address this issue in the next section by additionally considering triplet effects. The isomerization components F_{iso} from the model fit are shown in subplot B with their respective standard deviations. The decrease in F_{iso} as a function of fragment length reminds of an exponential decay approaching a threshold. The isomerization times τ_{iso} can also be derived from the same model fit. By averaging over all fragment lengths, we find a mean isomerization time of $\bar{\tau}_{\text{iso}} = 48 \pm 11$ µs. F_{iso} refers to the fraction of molecules in a dark state in the isomerization model. This means that the molecules in the dark state cannot emit fluorescence photons. For larger DNA fragments, the fraction of dark molecules decreases, since more blinking dyes bind to larger fragments, and thus lower the molecule's probability of being completely dark. Although a simplified on/off isomerization model is employed, it provides a good description of the mSMR curves at short sampling times.

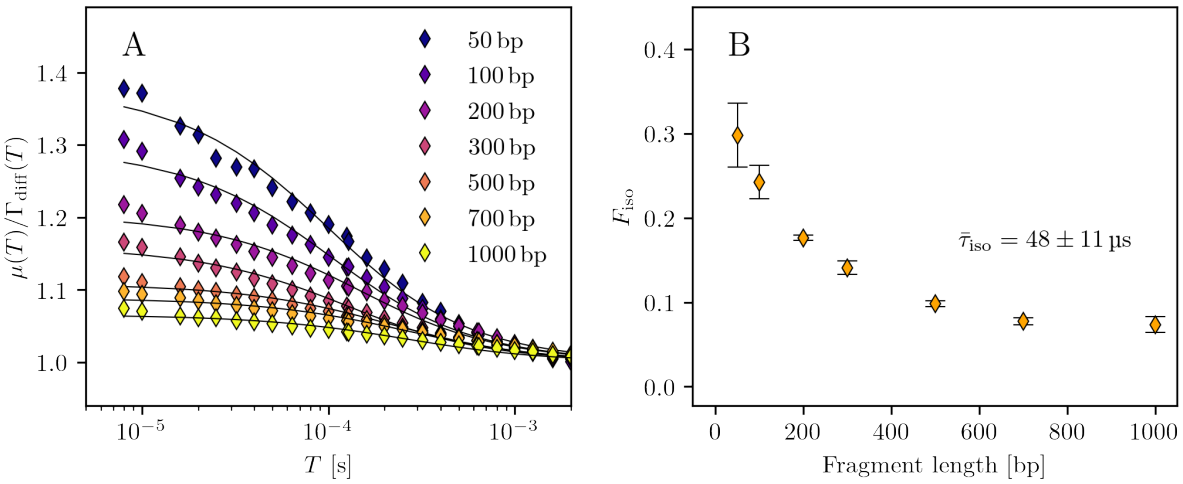

Figure 6.3: The isomerization effect in the mSMR analysis of DNA measurements. All measurements are performed at 2.5 µW excitation power and analyzed using the mSMR method. **A** The averaged isomerization part Γ_{iso} of the DNA dilution series. Γ_{iso} is obtained by dividing $\mu(T)$ by the diffusive part Γ_{diff}. **B** The fraction F_{iso} of the isomerization model, obtained by averaging the fitting results of each dilution series. The total averaged isomerization time $\bar{\tau}_{\mathrm{iso}}$ from the model fit is also included.

Triplet effects

So far, triplet states transitions were neglected in the analysis. To study the influence of the triplet state on DNA measurements in more detail, we perform an excitation power series on a 50 bp DNA mixture of 200 pg/µL concentration. Each measurement is conducted five-fold and analyzed with the mSMR method. From literature, increasing triplet fractions are expected for higher excitation powers, while the isomerization fraction should be unaffected [74, p. 290-293]. The following adapted mSMR model is used:

$$\mu(T) = \gamma_2\, \mu_0\, \Gamma_{\mathrm{diff}}(T)\, \Gamma_{\mathrm{iso}}(T)\, \Gamma_{\mathrm{trip}}(T). \tag{6.6}$$

Thus, the model accounts for isomerization and triplet states as well as diffusion. Because of the numerous parameters, such a model is difficult to fit. To reduce the degrees of freedom, the relaxation times of the triplet model and the isomerization model in the fitting routine are fixed. For the triplet part, $\tau_{\mathrm{trip}} = 4.5\,\mu s$ is set, which is comparable to the relaxation time of Alexa Fluor 488 derived in section 5.3.2. For the isomerization part, $\tau_{\mathrm{iso}} = 48\,\mu s$ is set, derived from the isomerization analysis in figure 6.3, subplot B. The results of the evaluation can be seen in figure 6.4. Subplot A shows the increasing averaged mSMR curves for the following excitation powers: 2.5, 3.0, 6.0 and 14.0 µW. The data are fitted with the extended mSMR model 6.6. By dividing through the diffusive part Γ_{diff}, the short-time fractions of the mSMR curves are obtained, shown in subplot B. The increase in the amplitudes for growing excitation powers stands out. The data are well described by the combined triplet and isomerization model. Subplot C shows the increasing triplet fractions F_{trip} as a function of excitation power, fitted by a straight line. Even though the F_{trip} data points are noisy and have large standard deviations, the upward trend is clear. For an excitation power of 2.5 µW, a triplet fraction of $F_{\mathrm{trip}} \approx 0.15$ is found. This proportion is substantial, so the triplet effect should be considered in the model for DNA analyses. In subplot D, the fractions F_{trip} from the model fit are given. Except for low excitation powers ($< 4.0\,\mu W$), no trend is observable and the data can be described by a constant line at $F_{\mathrm{iso}} = 0.35$, which is

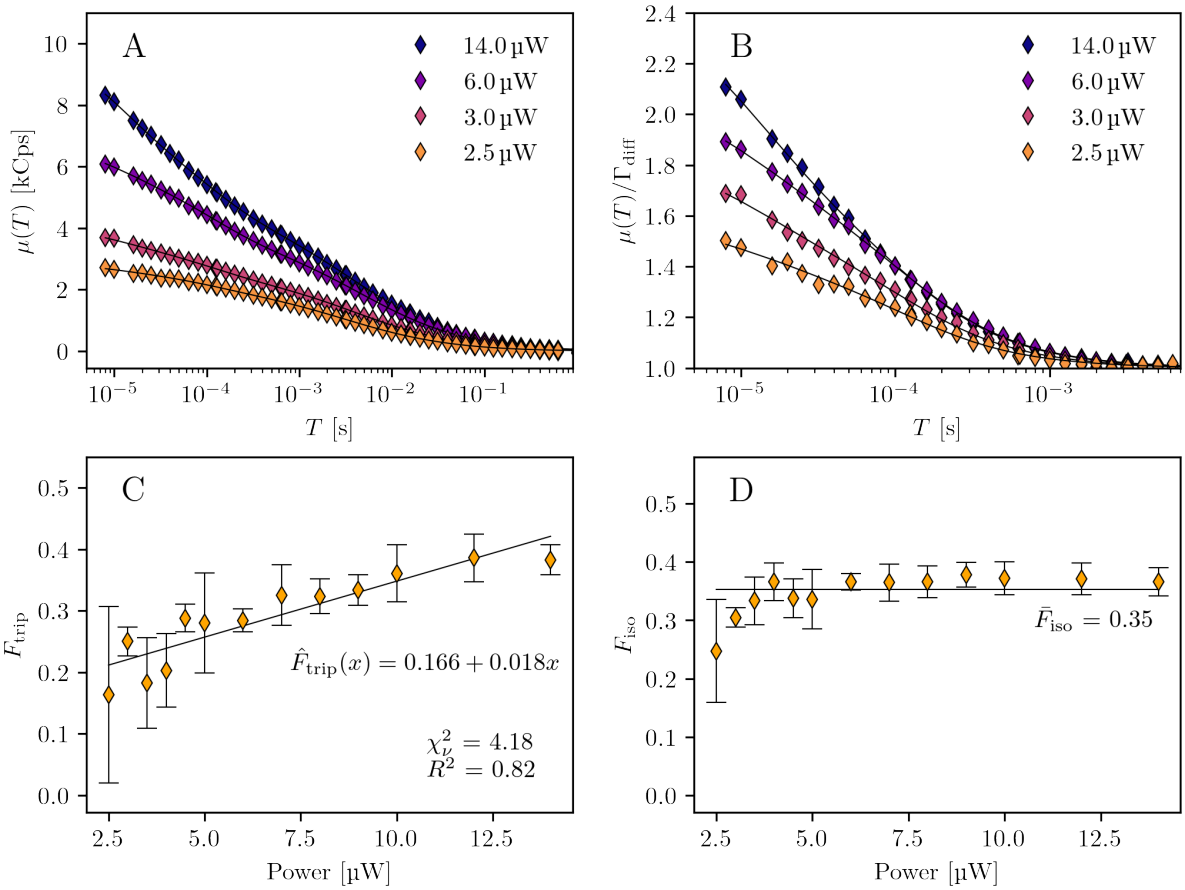

Figure 6.4: Triplet and isomerisation effects in the mSMR analysis of DNA measurements. Fluorescence fluctuationens of 50 bp DNA with a concentration of 200 pg/µL, recorded for increasing excitation powers from 2.5 to 14.0 µW. **A** Averaged mSMR curves with corresponding model fit. **B** Division of $\mu(T)$ by the diffusive part Γ_{diff}, leaving the isomerization and triplet fractions of the data series. **C** The isolated triplet fractions F_{trip} from the model fit. The data are fitted with a straight line. **D** The isolated isomerization fractions F_{iso} from the model fit. The weighted average over all excitation powers is included as a solid line.

similar to $F_{\mathrm{iso}} = 0.3$ from the 50 bp measurement in figure 6.3 subplot B. It must be noted, however, that even small changes in the fixed τ_{trip} and τ_{iso} in the model lead to significant changes in the results. We must therefore be careful in the discussion and interpretation of these results.

In summary, the mSMR model reliably describes the photokinetic effects of isomerization in DNA measurements at low excitation powers. At higher excitation powers, an extended model can can be used to represent triplet states, too. But the results are noisy and measurements at low excitation powers are recommended.

6.2.3 Photobleaching in the analysis of DNA mixtures

The results of the previous sections tell us that fluorescence fluctuation measurements on DNA solutions should be performed at low excitation powers. In addition to increasing triplet effects, which make model fitting difficult, fluorescence bleaching occurs in DNA analyses at higher excitation powers. An experiment to illustrate this effect is to measure DNA dilution series of defined fragment length composition at low and high excitation

powers (2.5 µW and 140 µW) with and without an anti-fading agent. As antifading agent we use 2.5 % (w/v) 1,4-diazabicyclo[2,2,2]octane (DABCO), whose efficacy as an antifade has been demonstrated in various studies [121, 122, 123, 124]. Figure 6.5 shows the results of this experiment. In subplot A, the count rates of the dilution series without antifading

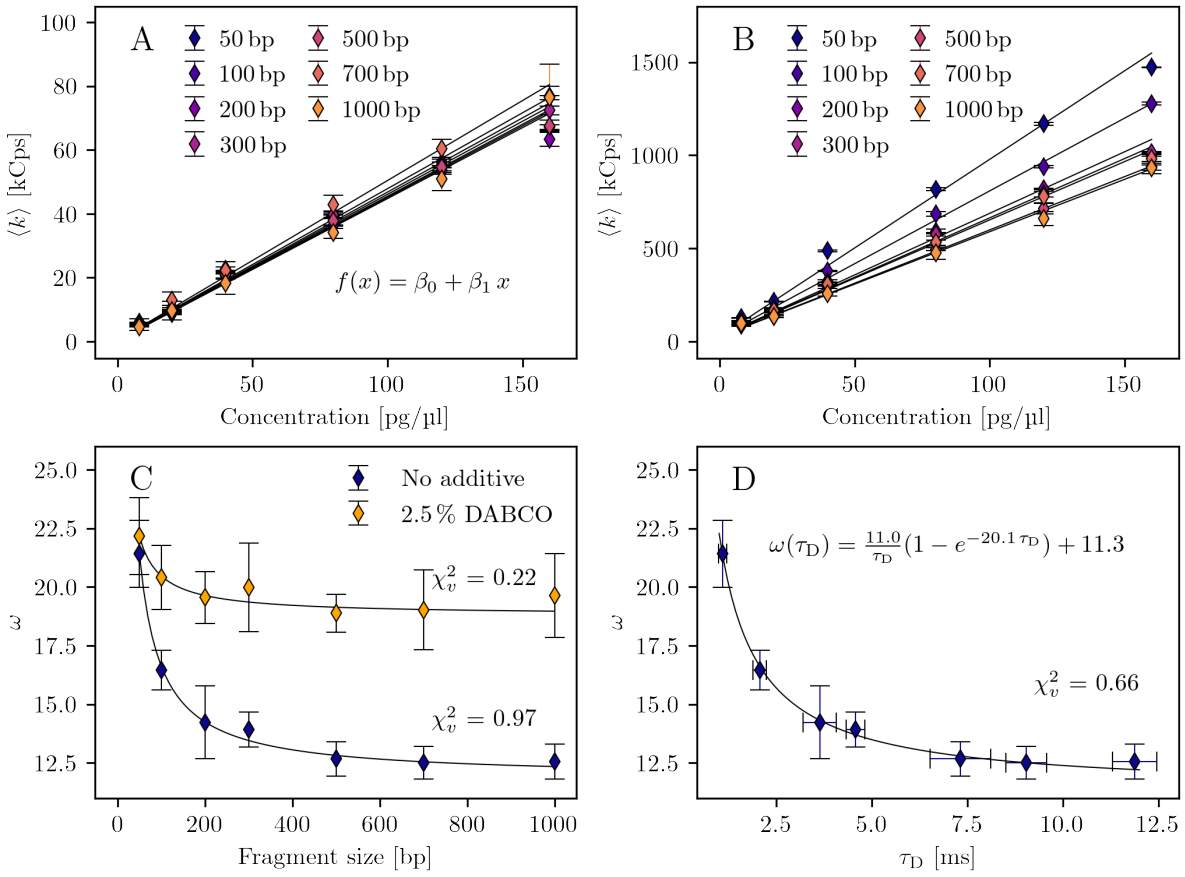

Figure 6.5: Photobleaching in DNA dilution series. **A** Dilution series of defined fragment length composition recorded at 2.5 µW. The data series are fitted with a straight line through a common y-axis interception at concentration = 0 is 0.36 ± 0.02. **B** Dilution series of the same concentration recorded with 140 µW laser power. The common y-axis intercept concentration = 0 is 27.18 ± 2.43. **C** Plot of the ratio $\omega = \beta_{1,\mathrm{high}}/\beta_{1,\mathrm{low}}$ of the slopes of DNA dilution series of varying fragment length recorded at high laser powers 140 µW and low laser powers 2.5 µW. Data from measurements on dilution series with additional 2.5 % (w/v) of the anti fading agent DABCO are also shown. **D** Plot of the ratio $\omega = \beta_{1,\mathrm{high}}/\beta_{1,\mathrm{low}}$ against the mean diffusion times τ_D of the DNA dilution series of defined fragment length.

agent recorded at 2.5 µW are given. The dilution series overlap within the experimental accuracy and that there are no systematic deviations between the measurement series. Subplot B shows the fluorescence rates of the same samples recorded at soaring laser powers of 140 µW. For increasing fragment sizes, the slopes of the dilution series decrease, although the same concentrations are studied in each case. The effect becomes more pronounced by comparing the slopes of the dilution series at low and high laser powers. To do this, the data are fitted with a straight line and the ratio ω of the slopes at high and low excitation powers is formed.

$$\omega_i = \frac{\beta_{1,\mathrm{high},i}}{\beta_{1,\mathrm{low},i}} \qquad \text{for } i = 50, 100, 200, 300, 500, 700, 1000\,\mathrm{bp}. \tag{6.7}$$

Subplot C shows the ratio ω as a function of fragment length. Starting at $\omega = 22$ for 50 bp DNA, the ratio decreases significantly following an exponential decay and approaches a

limit of $\omega_\infty = 11.3$. The same analysis with 2.5 % DABCO added shows a less pronounced exponential decay and a significantly higher equilibrium level of$\omega_\infty = 19.5$. Thus, the addition of the antifading agent DABCO almost completely eliminates the difference between the measured count rates at low and high excitation powers.
Following a more general approach to describe the data, the fragment lengths of the solutions are replaced by the corresponding measured diffusion times τ_D from the mSMR analysis (see section 6.2.1). This step can be seen in subplot D. As before, the ratio of the slopes of the fluorescence rates of the dilution series decreases with increasing diffusion times. We use a probability-based approach to model the photobleaching as a function of τ_D [47, p. 25]:

$$N_\mathrm{f}(\tau_\mathrm{D}) = \frac{k_\mathrm{f}}{k_\mathrm{bl}}(1 - e^{-k_\mathrm{bl}\,\tau_\mathrm{D}}) \tag{6.8}$$

Where N_f is the average number of fluorescence photons. The parameters k_f and k_bl are the fluorescence rate and the bleaching rate. Setting $k_\mathrm{int} = \frac{k_\mathrm{f}}{k_\mathrm{bl}}$ and dividing the expression by τ_D gives the photon rate as a function of the diffusion time [54, p. 11]. To model the asymptotic approximation to a non-zero limit value, a constant *const* is introduced, which turns equation 6.8 into [54, p. 11]:

$$f(\tau_\mathrm{D}) = \frac{k_\mathrm{int}}{\tau_\mathrm{D}}(1 - e^{-k_\mathrm{bl}\,\tau_\mathrm{D}}) + const \tag{6.9}$$

Fitting the data with equation 6.9 yields a satisfactory result ($\chi^2_\nu = 0.17$). This functional relation can be used to correct fluorescence count rates recorded at soaring excitation powers, allowing more precise fluorescence spectroscopic measurements [54].

The measurement results prove that high excitation powers lead to an underestimation of the slopes of the fluorescence count rates in the DNA dilution series. This effect increases with larger DNA experiments. By adding the antifading agent DABCO, this effect can be almost completely suppressed suggesting that the effect is caused by photobleaching.

6.2.4 Characterization of natural DNA mixtures

Up to this point, all experiments were performed with DNA solutions of defined composition, where each solution consisted of DNA fragments of a defined length. We now examine whether the derived models in the previous section are suitable for characterizing DNA mixtures of unknown composition. An interesting application is a quality control of DNA libraries for sequencing. For this, four sequencing libraries (Lex1, Gen, Lex2, Exo) were externally characterized in the following steps:

1. The mass concentration was determined using the Qubit fluorometer (ThermoFisher Scientific, USA)

2. The mean fragment length of the libraries was measured using the Tapestation (Agilent, USA).

3. The average molecular weight MW of the DNA molecules in the library was approximated using equation 6.4.

4. From the average molecular weight of the DNA molecules in the library MW and the mass concentration c, the molarity M was calculated.

$$M = \frac{c}{MW} \tag{6.10}$$

Each sequencing library was prepared and characterized five times (Gen) or eight times (Lex1, Lex2, Exo).

In the following, we want to collect the same information in just one measurement. For characterization, the four libraries are first diluted in several steps, then labeled with an intercalating agent, and finally measured in our home-built confocal plate reader. The fluorescence traces are analyzed via the mSMR method. We use the findings from section 6.2.1 to derive the required information to extract a total of three parameters: the average fragment length of the DNA molecules, the DNA mass concentration, and the molarity of the DNA in the mixture. The parameters are calculated as follows:

1. Mass concentration

The mass concentration of a DNA mixture of unknown composition is determined with two methods.
Method 1: Using the fluorescence count rate to get the mass concentration via a calibration line. The calibration line is obtained from the DNA dilution series of defined composition (see figure 6.5, subplot A). The count rates for each concentration step i are averaged to obtain a common calibration curve.

$$\langle k \rangle_i = \frac{1}{N} \sum_{j=1}^{N} \langle k \rangle_{i,j}, \qquad \text{for } j = 50, 100, 200, 300, 500, 700, 1000\,\text{bp}. \tag{6.11}$$

Since the calibration curve shows a slight curvature, a 2nd order polynomial fit is performed.

$$\langle \hat{k} \rangle(c) = \beta_0 + \beta_1 c + \beta_2 c^2 = 0.37 + 0.51c - 4.2 \times 10^{-4} c^2. \tag{6.12}$$

Equation 6.12 can be used to derive the mass concentration c from the measured fluorescence count rate for unknown samples. The prerequisite is that the experimental parameters are the same as for the calibration measurement. The physically plausible solution for the concentration is given by

$$c(\langle k \rangle) = -\frac{\beta_1}{2\beta_2} - \sqrt{\left(\frac{\beta_1}{2\beta_2}\right)^2 - \frac{\beta_0 - \langle k \rangle}{\beta_2}}, \qquad \text{for } \langle k \rangle \leq \beta_0 - \frac{\beta_1^2}{4\beta_2}. \tag{6.13}$$

Method 2: Determining the mass concentration using the molarity and mean fragment length of the DNA mixture.

$$c = MW \times M \overset{6.4}{\approx} 650\,\text{g/mol} \times n \times M \tag{6.14}$$

To get the mass concentration, the average fragment length n and the molarity M of the solution are needed. These are derived in the folowing sections using equation 6.18 (method 2) for the average fragment length, and using equation 6.19 (method 2) for the molarity.

2. Fragment length

Both the mean single-molecule brightness rate μ_0 and the mean diffusion coefficient τ_D can be used to estimate the mean fragment length of a DNA solution.
Method 1: Taking the single-molecule brightness rates to get the fragment length via a calibration. Figure 6.1 subplot B shows the empirical relationship between μ_0 and the mean fragment length, given by

$$\mu_0(n) = \beta_0\, n + \beta_1\, n^2 = 0.097n - 2.0 \times 10^{-5}\, n^2, \tag{6.15}$$

which directly results in the following physically plausible solution:

$$n(\mu_0) = -\frac{\beta_0}{2\beta_1} - \sqrt{\left(\frac{\beta_0}{2\beta_1}\right)^2 + \frac{\mu_0}{\beta_1}}, \qquad \text{for } \mu_0 \leq \frac{-\beta_0^2}{4\beta_1}. \tag{6.16}$$

Method 2: Using the diffusion coefficient to get the fragment length via a calibration. Figure 6.1 subplot C shows the empirical relationship between D and average fragment length, described by the following equation:

$$D(n) = \beta_0 \times n^{\beta_1} = 965 \times n^{-0.82}. \tag{6.17}$$

The expression is solved for the average fragment length as follows:

$$n(D) = \left(\frac{D}{\beta_1}\right)^{\frac{1}{\beta_0}}. \tag{6.18}$$

3. Molarity

The molarity of the DNA mixture is determined by the mean particle number from the mSMR analysis. Since the mean particle numbers from FCS and mSMR analysis deviate significantly from the theoretically expected particle number (see section 6.2.1), it must be corrected accordingly. The mean particle number is determined via the single-molecule brightness rate of the mSMR using equation 5.9. The obtained mean particle numbers are corrected using the findings illustrated in figure 6.2 subplot B.

$$\langle N \rangle_{\text{corr}} = \langle N \rangle \times \omega(n) \tag{6.19}$$

Two methods are available to estimate the ratio ω in equation 6.19.
Method 1: Taking the averaged ratio of $\omega = 0.442$ to correct the measured mean particle number.
Method 2: Employing the fragment length dependent empirical model for correction ($\omega(n) = 0.5 - 2.8 \times 10^{-4} n + 1.6 \times 10^{-7} n^2$).

Having seen the methods to determine the parameters for characterization using the calibration measurements from section 6.2.1, we will take a comparative look at the results of this characterization

Characterization results

The results of the one-measurement characterization of four DNA sequencing libraries are shown in figure 6.6. In each case, the results of the external characterization are presented in comparison to the results of the two mSMR-based evaluation methods. In

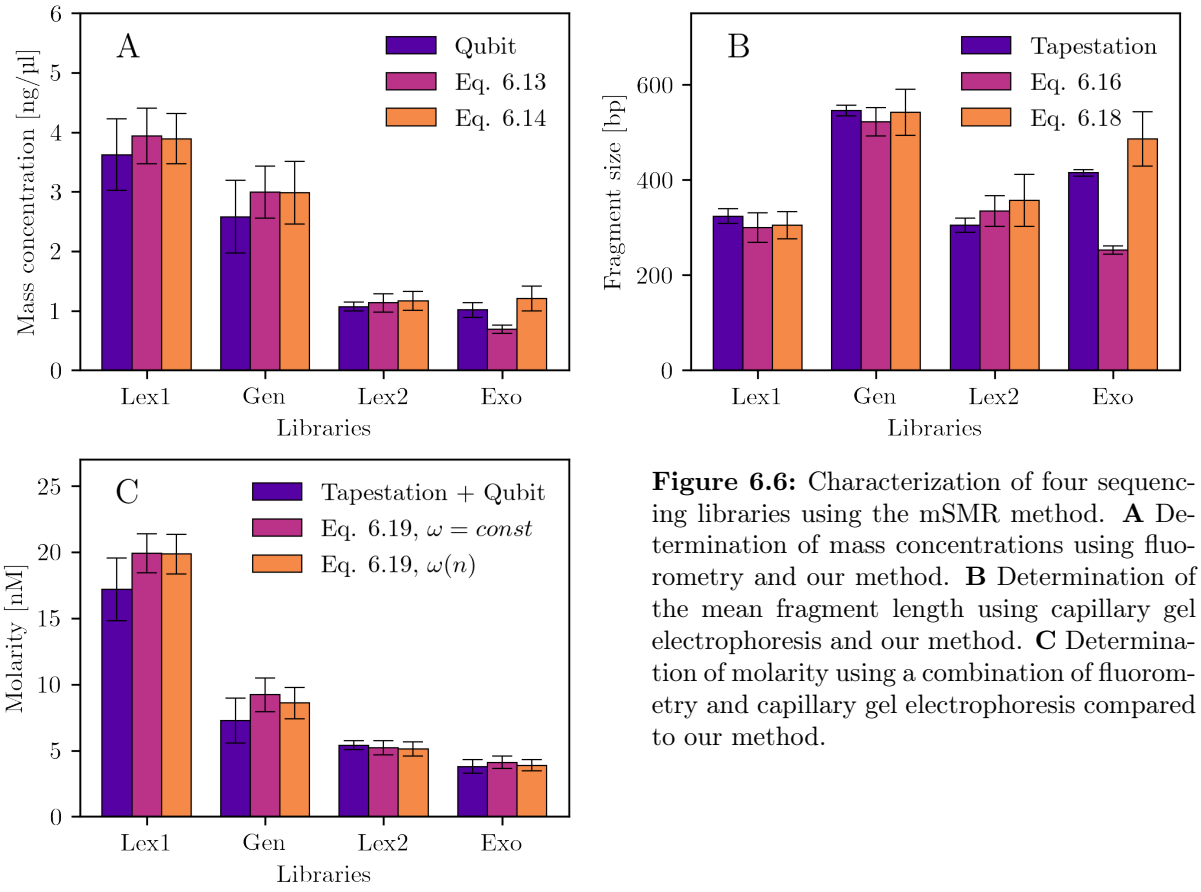

Figure 6.6: Characterization of four sequencing libraries using the mSMR method. **A** Determination of mass concentrations using fluorometry and our method. **B** Determination of the mean fragment length using capillary gel electrophoresis and our method. **C** Determination of molarity using a combination of fluorometry and capillary gel electrophoresis compared to our method.

subplot A, the determined mass concentrations of the four studied sequencing libraries is shown. For the Lex1, Gen, and Lex 2 libraries, the mass concentrations are the same within standard deviations for all three methods. For the Exo library, however, the mass concentration via equation 6.13 (method 1) is clearly too low, while the results via equation 6.14 (method 2) show a good agreement. The results of the fragment lengths in subplot B show a comparable picture. For the three libraries Lex1, Gen and Lex2, the methods show good agreement within standard deviations. But the determined fragment length of Exo library according to equation 6.16 (method 1) clearly deviates, whereas the results according to equation 6.18 (method 2) show good agreement with the results of the external characterization. The determined molarities of all libraries in subplot C agree for all methods within standard deviations.

In summary, the characterization of sequencing libraries using our home-built confocal plate reader and the mSMR method shows a good agreement with the externally conducted characterization using fluorometry and capillary gel electrophoresis. Thus, the four sequencing libraries can be characterized by a one-step measurement.

6.3 Discussion

In this chapter, the mSMR method was used to analyze fluorescence fluctuations of a more complex biological system. To begin with, measurements were performed on DNA mixtures of defined composition, revealing some important aspects that we discuss in the following.

First, the single-molecule brightness rate increases sublinearly for larger DNA fragment lengths (see figure 6.1). Intuitively, we would expect a linear relationship between fragment length and single-molecule brightness, since the fluorescent dye should stain all fragment lengths with equal density as related dyes do [117, p. 3017-3018][118, p. 1197-1198]. This sublinear relationship therefore has probably two causes: photobleaching and fringe effects. Photobleaching is caused by longer dwelling times of large DNA molecules in the detection volume. This leads to an increasing number of absorption-emission cycles and thus a higher probability to bleach. Fringe effects occure because of the increasing spatial extent of large diffusing DNA molecules. Unlike the assumed point-like fluorophore in the mSMR model, parts of the labeled DNA polymer may be outside the detection volume, reducing the number of bound fluorophores that contribute to the total single-molecule brightness.

Second, the calculated diffusion coefficients of the DNA mixtures in figure 6.1, subplot D agree with literature. A simple power law is suitable to describe our DNA diffusion coefficients in the studied range, giving an exponent of $\beta_1 = -0.79 \pm 0.02$ which is somewhat larger than a reported value of $\beta_1 = -0.72$ [125, p. 1626-1627]. Using a semiflexible chain model that takes into account the persistence length of DNA, we get comparable results. Generally, the semiflexible model describes the data accurate. However, the experimental findings show a somewhat steeper curve than the values from the literature and the model predictions. This is possibly due to the addition of DMSO to the samples. DMSO weakens hydrogenbonds, thus influencing the intramolecular interactions in the DNA molecule. This may affect the persistence length or the hydrodynamic radius of the DNA polymers. A repetition of the measurements in a buffer environment without DMSO would provide clarity here but is hard to implement. Without the addition of DMSO, large peaks occur in the fluorescence traces of the measurements, which are presumably caused by aggregated DNA molecules, making a reliable evaluation of the fluorescence traces difficult.

Third, we observe a discrepancy in the mean particle number between experiment and theory (see figure 6.2). The difference is probably due to the polymeric nature of DNA. The FFS theory assumes point-like particle. This does not hold for polymeric DNA molecules, which are labeled with multiple fluorophores along the chain. In fact, we observe larger deviations for larger DNA molecules. In addition, the particle number is strongly dependent on the excitation power (data not shown). The average number of particles is overestimated more strongly at high excitation powers than at low powers. The dependence of the effect on excitation power and fragment size makes photobleaching a likely cause and is discussed below. The result emphasizes the need to perform FFS experiments on DNA mixtures at low excitation levels. For quantitative evaluations, the experimental conditions must be kept the same to allow a correction of the particle numbers.

Fourth, isomerization effects occur when measuring DNA mixtures. The cause of isomerization is the staining dye RiboGreen, which is an asymmetric cyanine dye. Cyanine dyes show a cis/trans isomerization in their molecule structure, which leads to

a blinking of the dyes [74, p. 290-293]. We used a simple on/off isomerization model that does not reflect nature and ignores the underlying finite birth death process but can be specified analytically. However, the description of the data is incomplete (see figure 6.3), which can be observed in slight variations and is probably caused by the simplified isomerization model or triplet effects. Nevertheless, we see decreasing proportions of dark molecules given by F_{iso} for increasing fragment lengths. This makes sense, since large DNA fragments can bind more intercalator molecules, thus reducing the probability for a complete dark state.

Fifth, we attempted to separate the photokinetic effects of isomerization and triplet states (see figure 6.4). We performed FFS measurements on 50 bp DNA at increasing excitation powers. As with the Alexa Fluor 488 measurements in section 5.3.2, increasing excitation power should increase the triplet fraction, while the fraction of molecules in the dark state due to cis-trans isomerization should remain constant [74, p. 290-293]. To keep the degrees of freedom in the model fit low, we preset the relaxation times of the triplet and isomerization models using estimated values from the previous sections. Although the data are noisy, an increase in the triplet fractions and a constant trend in the isomerization fractions can be observed for increasing excitation powers. It is noticeable that the model fit to the photokinetic components of the mSMR is very good and there are fewer deviations than with the isomerization model alone. The isomerization fractions F_{iso} of the 50 bp measurements in figure 6.3 and 6.4 at 2.5 µW are comparable (0.3 to 0.35). But the picture is different for triplet effects. While in the first case triplet states were neglected, the other case gives $F_{\text{trip}} \approx 0.15$. Together with the observation that fitting the photokinetic parts of the mSMR curves with the simple on/off isomerization model gives an incompletely description, we can infer the importance of triplet states in DNA measurements. However, weighing the benefits of the extended model against the disadvantages due to the higher degrees of freedom seems to justify the use of the simple isomerization model for describing the mSMR curves at low excitation powers.

Sixth, an important effect in the analysis of DNA samples via FFS experiments is photobleaching. In FFS experiments, very high excitation intensities can occur locally [53, p. 9], which can lead to significant bleaching and thus cause measurement deviations (increasing $\langle N \rangle$, decreasing μ_0 and τ_{D}). During our FFS experiments on DNA mixtures, we probably encountered photobleaching at several points. Before each measurement, the detection spot must be irradiated for 10 s. Without this step, a significant drop in the fluorescence count rate occurs in the first seconds, thus violating the requirement of stationarity in FFS analysis. Then, the fluorescence measurements at low and high excitation powers shows a fragment size dependent influence on the count rates (see figure 6.5). The photobleaching probability is directly related to the number of excitation cycles [45, p. 2655-2657] and therefore to the duration of irradiation by the excitation light. Larger molecules diffuse slower and remain longer in the excitation volume, thus having a higher probability to bleach. Since this effect disappears when adding the anti-fading agent DABCO, this is a strong indication that photobleaching is indeed the cause.

To sum up, high excitation powers are problematic for DNA measurements in many respects. The increasing triplet fraction makes the evaluation of the mSMR curves with the simple isomerization model difficult, stronger bleaching effects lead to deviations in the single molecule parameters, and fluorescence saturation may also occur. For a reliable characterization of DNA mixtures labeled with RiboGreen, it is important to

work with minimal excitation power. An excitation power of 2.5 µW seems appropriate. In the final section of this chapter, the previous findings were brought together to characterize DNA mixtures of unknown composition for sequencing. Since conventional characterization requires a multistep procedure, we want to simplify this by a one-step FFS analysis. By using the retrieved calibration curves from DNA mixtures of defined composition, the mass concentration, mean fragment length, and molarity of the DNA libraries were determined. In general, the results showed good agreement with the external characterization within the measurement uncertainties. However, for the Exo library, too low mass concentrations and fragment lengths were observed using equations 6.13 (method 1) and 6.16 (method 1). Since both methods rely on the single-molecule brightness rate, the discrepancy might be due to insufficient staining of the DNA fragments. The alternative methods using equations 6.14 (method 2) and 6.18 (method 2), showed a good agreement with the results of the standard method, and thus seem to be less susceptible to differences in staining. For the establishment of an assay, this circumstance could be used as a quality check to ensure complete staining of the sample solution. Alternatively, bypassing the brightness-based methods could significantly speed up the measurement procedure by eliminating a long lasting incubation step after adding the dye. This would shorten the processing time to characterize an unknown DNA sample from over 2 h to a few minutes.

In summary, the combination of our home-built confocal plate reader and the mSMR model is suitable for the characterization of DNA mixtures. However, some aspects have to be considered. The addition of DMSO is needed to prevents the formation of DNA aggregates and enables reliable measurements. Also, an excitation rate of 2.5 µW minimizes photobleaching and triplet effects and allows evaluation of the mSMR curves with a simple isomerization model. If the measurement parameters are kept constant, calibration measurements on DNA mixtures of defined composition can be used to characterize DNA sequencing libraries. The derived one-measurement results for mass concentration, mean fragment length as well as molarity of the DNA libraries are comparable to the results of an external multistep characterization.

7 Conclusion

Fluorescence fluctuation spectroscopy (FFS) is a powerful technique for the analysis of molecular biological systems. However, the correct conduction and evaluation of these measurements requires a lot of experience, which is a hurdle. The present work was intended to reduce these obstacles and therefore pursued two objectives: first, the validation of the newly developed method the *mean single-molecule rate* (mSMR) for the analysis of fluorescence fluctuations, and second, the evaluation of a home-built confocal plate reader for automatic fluorescence measurements at the single-molecule level. A detailed theoretical description of fluorescence fluctuation and related phenomena provided a profound understanding and enabled to interpret and discuss the gathered results. In addition, the methods and instruments used for the experimental realization were introduced, featuring a simulation engine and a home-built confocal plate reader to retrieve fluorescence fluctuation data.

We subjected the mSMR model to a three-step review and started with analyses on fluorescence fluctuations generated by the simulation engine. This guaranteed completely controllable conditions. The mSMR model could recover the initial simulation parameters from the fluorescence fluctuations, illustrating the principle functionality of the mSMR method. An essential aspect of the simulation was the controllable superposition of afterpulsing and detector dead time as well as background noise to the data. With suitable correction procedures, we could eliminate the artefacts, thus allowing to evaluate the mSMR curves even at small time scales.

For the following FFS measurements, we used the home-built confocal plate reader. Measurements on Alexa Fluor 488 dilution series demonstrated the plate reader's suitability to perform automated fluorescence fluctuation measurements in 384 well microtiter plates. The subsequent analysis of the data using the established fluorescence fluctuation spectroscopy (FCS) proved the system's single-molecule sensitivity. Although an unfavorable long-distance objective lens was used, the system provided reliable results over a wide concentration range, recommending the system for further FFS measurements. To continue the review, we analyzed these fluorescence fluctuation traces with the mSMR method, too. The interesting question was how the established FCS and our mSMR method compare. Both visually and statistically, no difference in the long-time diffusive part of the models could be identified. The derived parameters (τ_D, μ_0 and $\langle N \rangle$) did not deviate significantly. However, when considering the photokinetic effects on short time scales, differences were found between the models. The mSMR model appears to yield more plausible results for the description of triplet state transitions (τ_T and F_trip), indicating an advantage over the FCS method. The difference is probably due to the correction of detector artefacts, which can be done on the cumulants of the mSMR but cannot be directly applied to the autocorrelation curves of FCS.

The final step of our review were measurements on a more complex biological system, for which we chose DNA mixtures. Dilution series of defined fragment length composition were systematically studied and compared to theoretical predictions. The derived diffusion coefficients could be described by a semiflexible chain model and matched the

theoretical expectations. On the other side, the fragment length specific single molecule brightness rate showed an initially unexpected sublinear relationship, and the measured mean particle number of the DNA mixtures differed significantly from the theoretical prediction, too. These observations are probably caused by the polymeric structure of DNA and photobleaching. Empirical calibration curves could be found to describe both relations. The analysis of photokinetic effects in DNA measurements included isomerization, triplet state transitions, and photobleaching. Isomerization effects caused by the blinking of bound dye molecules can be described by a simple on/off model at low excitation powers but are dominated by triplet effects at higher excitation powers. Since large excitation powers lead to photobleaching, thus preventing a meaningful analysis, low excitation powers of 2.5 µW are recommended.
The findings from the measurements on defined DNA solutions were used to characterize four DNA sequencing libraries. We could determine the mass concentration, the average fragment length of the library and the molarity. The results were in good agreement with an externally perfomed characterization using a multistep process. Thus, the mSMR seems to be a suitable one-step method to characterize DNA sequencing libraries.

To conclude, the objectives of this thesis could be achieved. First, the mSMR could be established as a trustworthy analysis tool for fluorscence fluctuations, showing the following advantages:

- an interpretation of the curves analogous to FCS,
- the incoperation of photokinetic effects such as triplet state transitions and isomerization,
- a correction of the mSMR curves for common detector artefacts and background noise,
- visually and statistically more precise results than FCS analysis at short-time scales,
- and the analysis of data retrieved from setups with single-excitation and single detection channel.

Second, our developed plate reader delivered a high degree of automation and reproducibility at the single-molecule level, which facilitates the execution of FFS measurements. The results of this work will make future FFS experiments more feasible and therefore available to a broader community.

7.1 Outlook

After showing the mSMR's comparability to the established FCS method and even pointing out advantages at short-time scales, the focus should be on practical applications. An interesting issue is the sequence-specific detection of DNA in a sample. Based on single-labeled probes, the mSMR method could use *in-situ* hybridizations to specifically detect sequences. This could be done using multiple probes that bind to different complementary sequence segments of the target DNA. Another interesting research question could be the study of antibody-antigen interactions or molecule-molecule interactions in general using the mSMR method. Since the introduced confocal plate reader can screen large parameter spaces effortlessly, exciting applications are sure to follow.

8 Abbreviations

Abbreviation	Meaning
CEF	Collection efficiency function
cPCH	Correlated photon-counting histogram
DMSO	Dimethyl sulfoxide
DNA	Desoxyribonucleic acid
dsDNA	double-stranded desoxyribonucleic acid
FCA	Fluorescence cumulant analysis
FCCS	Fluorescence cross-correlation spectroscopy
FCS	Fluorescence correlation spectroscopy
FFS	Fluorescence fluctuation spectroscopy
FIDA	Fluorescnece intensity distribution analysis
FIMDA	Fluorescence intensity multi distribution analysis
FITC	Fluorescein isothiocyanate
FLCS	Fluorescence life time spectroscopy
FRAP	Fluorescence recovery after photobleaching
GFP	Green fluorescent protein
HOFCS	High order fluorescence correaltion spectroscopy
HPLC	High performance liquid chromatography
LD	Long-distance
MCS	Monte Carlo simulation
MDE	Molecular detection efficiency
MSD	Mean squared displacement
mSMR	Mean single molecule rate
MTP	Microtiterplate
NA	Numerical aperture
NGS	Next generation sequencing
NHS	N-hydroxysuccinimid
PCH	Photon-counting histogram
Poi	Poisson distribution
PSF	Point spread function
RNA	Ribonucleic acid
SMD	Single-molecule detection
SPAD	Single-photon avalanche diode
STED	Stimulated emission depletion
TIFCA	Time integrated fluorescence cumulant analysis

9 Bibliography

[1] William E. Moerner. Single-Molecule Spectroscopy, Imaging, and Photocontrol: Foundations for Super-Resolution Microscopy (Nobel Lecture). *Angewandte Chemie - International Edition*, 54(28):8067–8093, 2015. doi: 10.1002/anie.201501949.

[2] Joseph R. Lakowicz. *Principles of fluorescence spectroscopy.* Springer Science+Business Media, LLC, New York, 3rd edition, 2006. ISBN 0387312781. doi: 10.1007/978-0-387-46312-4.

[3] W. E. Moerner and L. Kador. Optical detection and spectroscopy of single molecules in a solid. *Physical Review Letters*, 62(21):2535–2538, 1989. doi: 10.1103/PhysRevLett.62.2535.

[4] J. C. Bergquist, Randall G. Hulet, Wayne M. Itano, and D. J. Wineland. Observation of quantum jumps in a single atom. *Physical Review Letters*, 57(14):1699–1702, 1986. doi: 10.1103/PhysRevLett.57.1699.

[5] Frank Dietrich and Herbert Walther. Physical Review Letters: Comments. *Physical Review Letters*, 58(3):203–207, 1987. doi: 10.1103/PhysRevLett.18.301.

[6] Boris Rotman. Measurement of activity of single molecules of β-D-galactosidase. *PNAS*, 47(12):1981–1991, 1961. doi: 10.1073/pnas.47.12.1981.

[7] T. Hirschfeld. Optical microscopic observation of single small molecules. 15(12): 2965–2966, 1976. doi: 10.1364/AO.15.002965.

[8] T. Hirschfeld. Quantum efficiency independence of the time integrated emission from a fluorescent molecule. 15(12):3135–3139, 1976. doi: 10.1364/AO.15.003135.

[9] Norman J. Dovichi, John C. Martin, James H. Jett, and Richard A. Keller. Attogram Detection Limit for Aqueous Dye Samples by Laser-Induced Fluorescence. *Science*, 219(February):845–847, 1982. doi: 10.1126/science.6823553.

[10] Norman J. Dovichi, John C. Martin, James H. Jett, Mitchell Trkula, and Richard A. Keller. Laser-Induced Fluorescence of Flowing Samples Approach to Single-Molecule Detection in Liquids. *Analytical Chemistry*, 56(3):348–354, 1984. doi: 10.1117/12.936239.

[11] E. Brooks Shera, Newton K. Seitzinger, Lloyd M. Davis, Richard A. Keller, and Steven A. Soper. Detection of single fluorescent molecules. *Chemical Physics Letters*, 174(6):553–557, 1990. doi: 10.1016/0009-2614(90)85485-U.

[12] Jagadish Sankaran, Harikrushnan Balasubramanian, Wai Hoh Tang, Xue Wen Ng, Adrian Röllin, and Thorsten Wohland. Simultaneous spatiotemporal super-resolution and multi-parametric fluorescence microscopy. *Nature Communications*, 12(1):1–14, 2021. doi: 10.1038/s41467-021-22002-9.

[13] Jessica Balksjö Nannini and Måns Ehrenberg. The Nobel Prize in Chemistry 2014. The Royal Swedish Academy of Science, October 2014. online: `https://www.nobelprize.org/uploads/2018/06/press-26.pdf`, visited on 2022-06-13.

[14] Stefan W. Hell and Jan Wichmann. Breaking the diffraction resolution limit by stimulated emission: stimulated-emission-depletion fluorescence microscopy. *Optics Letters*, 19(11):780–782, 1994. ISSN 0146-9592. doi: 10.1364/ol.19.000780.

[15] Thomas A. Klar and Stefan W. Hell. Subdiffraction resolution in far-field fluorescence microscopy. *Optics Letters*, 24(14):954–956, 1999. doi: 10.1364/ol.24.000954.

[16] Ismail M. Khater, Ivan Robert Nabi, and Ghassan Hamarneh. A Review of Super-Resolution Single-Molecule Localization Microscopy Cluster Analysis and Quantification Methods. *Patterns*, 1(3):1–23, 2020. doi: 10.1016/j.patter.2020.100038.

[17] Eric Betzig, George H. Patterson, Rachid Sougrat, O. Wolf Lindwasser, Scott Olenych, Juan S. Bonifacino, Michael W. Davidson, Jennifer Lippincott-Schwartz, and Harald F. Hess. Imaging intracellular fluorescent proteins at nanometer resolution. *Science*, 313:1642–1645, 2006. doi: 10.1126/science.1127344.

[18] Samuel T. Hess, Thanu P.K. Girirajan, and Michael D. Mason. Ultra-high resolution imaging by fluorescence photoactivation localization microscopy. *Biophysical Journal*, 91(11):4258–4272, 2006. ISSN 00063495. doi: 10.1529/biophysj.106.091116.

[19] Jonas Fölling, Mariano Bossi, Hannes Bock, Rebecca Medda, Christian A. Wurm, Birka Hein, Stefan Jakobs, Christian Eggeling, and Stefan W. Hell. Fluorescence nanoscopy by ground-state depletion and single-molecule return. *Nature Methods*, 5(11):943–945, 2008. doi: 10.1038/nmeth.1257.

[20] Michael J. Rust, Mark Bates, and Xiaowei Zhuang. Sub-diffraction-limit imaging by stochastic optical reconstruction microscopy (STORM). *Nature Methods*, 3(10): 793–795, 2006. doi: 10.1038/nmeth929.

[21] Mike Heilemann, Sebastian Van De Linde, Mark Schüttpelz, Robert Kasper, Britta Seefeldt, Anindita Mukherjee, Philip Tinnefeld, and Markus Sauer. Subdiffraction-resolution fluorescence imaging with conventional fluorescent probes. *Angewandte Chemie - International Edition*, 47:6172–6176, 2008. doi: 10.1002/anie.200802376.

[22] Francisco Balzarotti, Yvan Eilers, Klaus C. Gwosch, Arvid H. Gynnå, Volker Westphal, Fernando D. Stefani, Johan Elf, and Stefan W. Hell. Nanometer resolution imaging and tracking of fluorescent molecules with minimal photon fluxes. *Science*, 355(February):606–612, 2017. doi: 10.1126/science.aak9913.

[23] Joerg Schnitzbauer, Maximilian T. Strauss, Thomas Schlichthaerle, Florian Schueder, and Ralf Jungmann. Super-resolution microscopy with DNA-PAINT. *Nature Protocols*, 12(6):1198–1228, 2017. doi: 10.1038/nprot.2017.024.

[24] Lorenz T. Sparrenberg, Benjamin Greiner, and Harald P. Mathis. The Mean Single Molecule Rate (mSMR) in the Analysis of Fluorescence Fluctuations: Measurements on DNA Mixtures of Defined Composition. *Journal of Fluorescence*, 31(6):1883–1894, 2021. doi: 10.1007/s10895-021-02803-3.

[25] Douglas Magde, Elliot Elson, and W. W. Webb. Thermodynamic fluctuations in a reacting system measurement by fluorescence correlation spectroscopy. *Physical Review Letters*, 29(11):705–708, 1972. doi: 10.1103/PhysRevLett.29.705.

[26] Douglas Magde, Elliot L. Elson, and Watt W. Webb. Fluorescence correlation spectroscopy. II. An experimental realization. *Biopolymers*, 13(1):29–61, 1974. doi: 10.1002/bip.1974.360130103.

[27] Rudolf Rigler and Ülo Mets. Diffusion of single molecules through a Gaussian laser beam. *Proceedings of SPIE*, 1921:239–248, 1992. doi: 10.1117/12.146154.

[28] R. Rigler, Ü . Mets, J. Widengren, and P. Kask. Fluorescence correlation spectroscopy with high count rate and low background: analysis of translational diffusion. *European Biophysics Journal*, 22(3):169–175, 1993. doi: 10.1007/BF00185777.

[29] A. G. Palmer and N. L. Thompson. Molecular aggregation characterized by high order autocorrelation in fluorescence correlation spectroscopy. *Biophysical Journal*, 52(2):257–270, 1987. doi: 10.1016/S0006-3495(87)83213-7.

[30] Arthur G. Palmer and Nancy L. Thompson. High-order fluorescence fluctuation analysis of model protein clusters. *Proceedings of the National Academy of Sciences of the United States of America*, 86(August):6148–6152, 1989. doi: 10.1073/pnas.86.16.6148.

[31] Arthur G. Palmer and Nancy L. Thompson. Intensity dependence of high-order autocorrelation functions in fluorescence correlation spectroscopy. *Review of Scientific Instruments*, 60(4):624–633, 1989. doi: 10.1063/1.1140374.

[32] Manfred Eigen and Rudolf Rigler. Sorting single molecules: Application to diagnostics and evolutionary biotechnology. *Proceedings of the National Academy of Sciences of the United States of America*, 91(13):5740–5747, 1994. doi: 10.1073/pnas.91.13.5740.

[33] Petra Schwille, Franz-Josef Meyer-Almes, and Rudolf Rigler. Dual-Color Fluorescence Cross-Correlation Spectroscopy for Multicomponent Diffusional Analysis in Solution. *Biophysical Journal*, 72:1878–1886, 1997. doi: 10.1016/S0006-3495(97)78833-7.

[34] Martin Böhmer, Michael Wahl, Hans-Jürgen Rahn, Rainer Erdmann, and Jörg Enderlein. Time-resolved fluorescence correlation spectroscopy. *Chemical Physics Letters*, 353:439–445, 2002. doi: 10.1016/S0009-2614(02)00044-1.

[35] Peter Kapusta, Radek Machá, Aleš Benda, and Martin Hof. Fluorescence Lifetime Correlation Spectroscopy (FLCS): Concepts, Applications and Outlook. *International Journal of Molecular Sciences*, 13:12890–12910, 2012. doi: 10.3390/ijms131012890.

[36] Yan Chen, Joachim D. Müller, Peter T.C. C So, and Enrico Gratton. The photon counting histogram in fluorescence fluctuation spectroscopy. *Biophysical Journal*, 77(1):553–567, 1999. doi: 10.1016/S0006-3495(99)76912-2.

[37] Peet Kask, Kaupo Palo, Dirk Ullmann, and Karsten Gall. Fluorescence-intensity distribution analysis and its application in biomolecular detection technology. *Proceedings of the National Academy of Sciences of the United States of America*, 96 (24):13756–13761, 1999. doi: 10.1073/pnas.96.24.13756.

[38] Joachim D. Müller. Cumulant analysis in fluorescence fluctuation spectroscopy. *Biophysical Journal*, 86(6):3981–3992, 2004. doi: 10.1529/biophysj.103.037887.

[39] Kaupo Palo, Ülo Mets, Stefan Jäger, Peet Kask, and Karsten Gall. Fluorescence intensity multiple distributions analysis: Concurrent determination of diffusion times and molecular brightness. *Biophysical Journal*, 79(6):2858–2866, 2000. doi: 10.1016/S0006-3495(00)76523-4.

[40] Bin Wu and Joachim D. Müller. Time-integrated fluorescence cumulant analysis in fluorescence fluctuation spectroscopy. *Biophysical Journal*, 89(4):2721–2735, 2005. doi: 10.1529/biophysj.105.063685.

[41] Nathan Scales and Peter S. Swain. Resolving fluorescent species by their brightness and diffusion using correlated photon-counting histograms. *PLoS ONE*, 14(12):1–31, 2019. doi: 10.1371/journal.pone.0226063.

[42] L. Song, E. J. Hennink, I. T. Young, and H. J. Tanke. Photobleaching kinetics of fluorescein in quantitative fluorescence microscopy. *Biophysical Journal*, 68(6): 2588–2600, 1995. doi: 10.1016/S0006-3495(95)80442-X.

[43] P. S. Dittrich and P. Schwille. Photobleaching and stabilization of fluorophores used for single-molecule analysis with one- and two-photon excitation. *Applied Physics B: Lasers and Optics*, 73(8):829–837, 2001. doi: 10.1007/s003400100737.

[44] Jörg Enderlein, David L. Robbins, W. Patrick Ambrose, Peter M. Goodwin, and Richard A. Keller. The statistics of single molecule detection: An overview. *Bioimaging*, 5(3):88–98, 1997. doi: 10.1002/1361-6374(199709)5:3<88::AID-BIO2>3.0.CO;2-2.

[45] C. Eggeling, J. Widengren, R. Rigler, and C. A.M. Seidel. Photobleaching of Fluorescent Dyes under Conditions Used for Single-Molecule Detection: Evidence of Two-Step Photolysis. *Analytical Chemistry*, 70(13):2651–2659, 1998. doi: 10.1021/ac980027p.

[46] Lloyd M. Davis and Guoqing Shen. Accounting for Triplet and Saturation Effects in FCS Measurements. *Current Pharmaceutical Biotechnology*, 7(4):287–301, 2006. doi: 10.2174/138920106777950843.

[47] Christoph Zander, Jörg Enderlein, and Richard A. Keller. *Single Molecule Detection in Solution: Methods and Applications*. Wiley-VCH, Weinheim, 1st edition, 2002. ISBN 978-3527403103. doi: 10.1002/3527600809.

[48] Iain D. Johnson. *The Molecular Probes Handbook: A Guide to Fluorescent Probes and Labeling Technologies*. Life Technologies Corporation, 11th edition, 2010. ISBN 9781626239777.

[49] Christian Ringemann, Andreas Schönle, Arnold Giske, Claas Von Middendorff, Stefan W. Hell, and Christian Eggeling. Enhancing fluorescence brightness: Effect of reverse intersystem crossing studied by fluorescence fluctuation spectroscopy. *ChemPhysChem*, 9(4):612–624, 2008. doi: 10.1002/cphc.200700596.

[50] Maria Ott. *Konformationsänderung und enzymatische Aktivität am einzelnen Molekül*. Dissertation, Technisch-Naturwissenschaftlichen Fakultät, Universität zu Lübeck, 2008. urn: urn:nbn:de:gbv:841-20091119349.

[51] Thorsten Pieper. *Diffusion of fluorescent molecules in micro- and nanostructured environments*. Dissertation, Fachbereich Physik, Universität Dortmund, 2007. doi: 10.17877/DE290R-8828.

[52] S. Chandrasekhar. Stochastic Problems in Physics and Astronomy. *Reviews of Modern Physics*, 15(1):1, 1943. doi: 10.1103/RevModPhys.15.1.

[53] Petra Schwille and Elke Haustein. Fluorescence correlation spectroscopy. An introduction to its concepts and applications. *Fluorescence Correlation Spectroscopy*, pages 1–33, 2009. doi: 10.1002/lpor.200910041.

[54] Lorenz Tim Sparrenberg, Benjamin Greiner, and Harald Peter Mathis. Bleaching correction for DNA measurements in highly diluted solutions using confocal microscopy. *PLoS ONE*, 15(7):1–17, 2020. doi: 10.1371/journal.pone.0231918.

[55] Benjamin Greiner. *Die Einzelmolekülverteilung in Fluoreszenz-Fluktuations-Experimenten*. Dissertation, Fachbereich Physik, Universität Dortmund, 2007. doi: 10.17877/DE290R-8411.

[56] D. E. Koppel, D. Axelrod, J. Schlessinger, E. L. Elson, and W. W. Webb. Dynamics of fluorescence marker concentration as a probe of mobility. *Biophysical Journal*, 16(11):1315–1329, 1976. doi: 10.1016/S0006-3495(76)85776-1.

[57] Hong Qian and Elliot L. Elson. Analysis of confocal laser-microscope optics for 3-D fluorescence correlation spectroscopy. *Applied Optics*, 30(10):1185–1195, 1991. doi: 10.1364/ao.30.001185.

[58] Samuel T. Hess and Watt W. Webb. Focal volume optics and experimental artifacts in confocal fluorescence correlation spectroscopy. *Biophysical Journal*, 83(4):2300–2317, 2002. ISSN 00063495. doi: 10.1016/S0006-3495(02)73990-8.

[59] Attila Nagy, Jianrong Wu, and Keith M. Berland. Characterizing observation volumes and the role of excitation saturation in one-photon fluorescence fluctuation spectroscopy. *Journal of Biomedical Optics*, 10(4):044015, 2005. doi: 10.1117/1.1991860.

[60] Brian J. Ford. Brownian movement in clarkia pollen: A reprise of the first observations. *The Microscope*, 40(4):235–241, 1992.

[61] Klaus Schulten and Ioan Kosztin. *Lectures in Theoretical Biophysics*. University of Illinois, 2000. online: `http://www.ks.uiuc.edu/Services/Class/NSM.pdf`, visited on 2022-06-13.

[62] M. Mercedes Tirado, Carmen López Martínez, and José García De La Torre. Comparison of theories for the translational and rotational diffusion coefficients of rod-like macromolecules. Application to short DNA fragments. *The Journal of Chemical Physics*, 81(4):2047–2052, 1984. doi: 10.1063/1.447827.

[63] Bruno H. Zimm. Dynamics of polymer molecules in dilute solution: Viscoelasticity, flow birefringence and dielectric loss. *The Journal of Chemical Physics*, 24(2):269–278, 1956. doi: 10.1063/1.1742462.

[64] Simon Keller. *Fluoreszenz-Korrelations-Spektroskopie in Polymerlösungen.* Dissertation, Department für Physik, LMU München, 2004. doi: 10.5282/edoc.2713.

[65] E. P. Petrov, T. Ohrt, R. G. Winkler, and P. Schwille. Diffusion and segmental dynamics of double-stranded DNA. *Physical Review Letters*, 97(25):1–4, 2006. doi: 10.1103/PhysRevLett.97.258101.

[66] Ludger Harnau, Roland G. Winkler, and Peter Reineker. Dynamic structure factor of semiflexible macromolecules in dilute solution. *Journal of Chemical Physics*, 104 (16):6355–6368, 1996. doi: 10.1063/1.471297.

[67] Christoph G. Baumann, Steven B. Smith, Victor A. Bloomfield, and Carlos Bustamante. Ionic effects on the elasticity of single DNA molecules. *Proceedings of the National Academy of Sciences of the United States of America*, 94(12):6185–6190, 1997. doi: 10.1073/pnas.94.12.6185.

[68] Gerald S. Manning. The persistence length of DNA is reached from the persistence length of its null isomer through an internal electrostatic stretching force. *Biophysical Journal*, 91(10):3607–3616, 2006. doi: 10.1529/biophysj.106.089029.

[69] Jerker Widengren, Ülo Mets, and Rudolf Rigler. Photodynamic properties of green fluorescent proteins investigated by fluorescence correlation spectroscopy. *Chemical Physics*, 250(2):171–186, 1999. doi: 10.1016/S0301-0104(99)00255-4.

[70] Jerker Widengren, Ülo Mets, and Rudolf Rigler. Fluorescence Correlation Spectroscopy of Triplet States in Solution: A Theoretical and Experimental Study. *Journal of Physical Chemistry*, 99(36):13368–13379, 1995. doi: 10.1021/j100036a009.

[71] Petra Schwille, Susanne Kummer, Ahmed A. Heikal, W. E. Moerner, and Watt W. Webb. Fluorescence correlation spectroscopy reveals fast optical excitation-driven intramolecular dynamics of yellow fluorescent proteins. *Proceedings of the National Academy of Sciences of the United States of America*, 97(1):151–156, 2000. doi: 10.1073/pnas.97.1.151.

[72] Laurie J. Jones, Stephen T. Yue, Ching Ying Cheung, and Victoria L. Singer. RNA quantitation by fluorescence-based solution assay: RiboGreen reagent characterization. *Analytical Biochemistry*, 265(2):368–374, 1998. doi: 10.1006/abio.1998.2914.

[73] Victoria L. Singer, Laurie J. Jones, Stephen T. Yue, and Richard P. Haugland. Characterization of PicoGreen reagent and development of a fluorescence- based solution assay for double-stranded DNA quantitation. *Analytical Biochemistry*, 249 (2):228–238, 1997. doi: 10.1006/abio.1997.2177.

[74] Jerker Widengren. Photophysical Aspects of FCS Measurments. In Rudolf Rigler and S. Elson Elliot, editors, *Fluorescence Correlation Spectroscopy - Theory and Applications*, chapter 13, pages 276–301. Springer-Verlag Berlin Heidelberg, Heidelberg, 1st edition, 2001. ISBN 3-540-67433-0. doi: 10.1007/978-3-642-59542-4.

[75] Jerker Widengren and Petra Schwillle. Characterization of photoinduced isomerization and back-isomerization of the cyanine dye cy5 by fluorescence correlation spectroscopy. *Journal of Physical Chemistry A*, 104(27):6416–6428, 2000. doi: 10.1021/jp000059s.

[76] Dennis E. Koppel. Statistical accuracy in fluorescence correlation spectroscopy. *Physical Review A*, 10(6):1938–1945, 1974. doi: 10.1103/PhysRevA.10.1938.

[77] Thorsten Wohland, Rudolf Rigler, and Horst Vogel. The standard deviation in fluorescence correlation spectroscopy. *Biophysical Journal*, 80(6):2987–2999, 2001. doi: 10.1016/S0006-3495(01)76264-9.

[78] L. Mandel. Sub-Poissonian photon statistics in resonance fluorescence. *Optics Letters*, 4(7):205–207, 1979. doi: 10.1364/ol.4.000205.

[79] Malvin C. Teich and Bahaa E. A. Saleh. Photon bunching and antibunching. *Progress in Optics*, 26:1–104, 1988. doi: 10.1016/S0079-6638(08)70174-4.

[80] L Mandel, E.C.G. Sudarshan, and E. Wolf. Theory of photoelectric detection of light fluctuations. *Proceedings of the Physical Society (1958-1967)*, 84(3):435–444, 1964. doi: 10.1088/0370-1328/84/3/313.

[81] Lindsey N. Hillesheim and Joachim D. Müller. The photon counting histogram in fluorescence fluctuation spectroscopy with non-ideal photodetectors. *Biophysical Journal*, 85(3):1948–1958, 2003. ISSN 00063495. doi: 10.1016/S0006-3495(03)74622-0.

[82] Alvaro Sanchez-Andres, Yan Chen, and Joachim D. Müller. Molecular brightness determined from a generalized form of Mandel's Q-parameter. *Biophysical Journal*, 89(5):3531–3547, 2005. doi: 10.1529/biophysj.105.067082.

[83] Hong Qian and Elliot L. Elson. Distribution of molecular aggregation by analysis of fluctuation moments. *Proceedings of the National Academy of Sciences of the United States of America*, 87(14):5479–5483, 1990. doi: 10.1073/pnas.87.14.5479.

[84] Hong Qian and Elliot L. Elson. On the analysis of high order moments of fluorescence fluctuations. *Biophysical Journal*, 57(2):375–380, 1990. doi: 10.1016/S0006-3495(90)82539-X.

[85] Jörg Enderlein and Ingo Gregor. Using fluorescence lifetime for discriminating detector afterpulsing in fluorescence-correlation spectroscopy. *Review of Scientific Instruments*, 76(3), 2005. doi: 10.1063/1.1863399.

[86] Kunihiko Ishii and Tahei Tahara. Correction of the afterpulsing effect in fluorescence correlation spectroscopy using time symmetry analysis. *Optics Express*, 23(25), 2015. doi: 10.1364/OE.23.032387.

[87] M. A. Finn, G. W. Greenlees, T. W. Hodapp, and D. A. Lewis. Real-time elimination of dead time and afterpulsing in counting systems. *Review of Scientific Instruments*, 59(11):2457–2459, 1988. doi: 10.1063/1.1139926.

[88] Peter Atkins and Julio De Paula. *Atkins' Physical Chemistry*. Oxford University Press, Oxford, 9th edition, 2010. ISBN 978-0-19-954337-3.

[89] Zdeněk Petrášek and Petra Schwille. Precise Measurement of Diffusion Coefficients using Scanning Fluorescence Correlation Spectroscopy. *Biophysical Journal*, 94(4): 1437–1448, 2008. doi: 10.1529/biophysj.107.108811.

[90] Petre Stoica and Randolph Moses. *Spectral Analysis of Signals*. Prentice Hall, Inc., Upper Saddle Riverm New Jersey, 1st edition, 2005. doi: 10.1109/msp.2007.273066.

[91] James W. Cooley, Peter A.W. Lewis, and Peter D. Welch. The Fast Fourier Transform and its Applications. *IEEE Transactions on Education*, 12(1):27–34, 1969. doi: 10.1109/TE.1969.4320436.

[92] K. A. O'Donnell. Correction of dead-time effects in photoelectric-counting distributions. *Journal of the Optical Society of America A*, 3(1):113, 1986. doi: 10.1364/josaa.3.000113.

[93] L. Campbell. Afterpulse measurement and correction. *Review of Scientific Instruments*, 63(12):5794–5798, 1992. doi: 10.1063/1.1143365.

[94] Joseph E. Reiner, Andreas Jahn, Laurie E. Locascio, Michael Gaitan, and John J. Kasianowicz. Liposome characterization with fluorescence cumulant analysis. *Proceedings of SPIE Noise and Fluctuations in Biological, Biophysical, and Biomedical Systems*, 6602:1 – 11, 2007. doi: 10.1117/12.726803.

[95] Frank Beichelt and Douglas Montgomery. *Teubner-Taschenbuch der Stochastik*. B. G.Teubner Verlag, Wiesbaden, 1st edition, 2003. ISBN 978-3-322-80068-8. doi: 10.1007/978-3-322-80067-1.

[96] Michael A. Poole and Patrick N. O'Farrell. The Assumptions of the Linear Regression Model. *Transactions of the Institute of British Geographers*, (52):145–158, 1971. doi: 10.2307/621706.

[97] John B. Willett and Judith D. Singer. Another cautionary note about r2: Its use in weighted least-squares regression analysis. *American Statistician*, 42(3):236–238, 1988. doi: 10.1080/00031305.1988.10475573.

[98] Kenneth Levenberg. A Method for the Solution of Certain Non-Linear Problems in Least Squares. *Quarterly of Applied Mathematics*, 2(2):164–168, 1944. doi: 10.1090/qam/10666.

[99] Donald W. Marquardt. An algorithm for least-squares estimation of nonlinear parameters. *Journal of the Society for Industrial and Applied Mathematics*, 11(2): 431–441, 1963. doi: 10.1137/0111030.

[100] Mary Ann Branch, Thomas F. Coleman, and Yuying Li. A Subspace, interior, and conjugate gradient method for large-scale bound-constrained minimization problems. *SIAM Journal of Scientific Computing*, 21(1):1–23, 1999. doi: 10.1137/S1064827595289108.

[101] Rene Andrae, Tim Schulze-Hartung, and Peter Melchior. Dos and don'ts of reduced chi-squared. *arXiv*, pages 1–12, 2010. doi: 10.48550/arXiv.1012.3754.

[102] Joachim D. Müller, Yan Chen, and Enrico Gratton. Fluorescence correlation spectroscopy. *Methods in Enzymology*, 361:69–92, 2003. doi: 10.1016/S0076-6879(03)61006-2.

[103] Lloyd M. Davis, Guoqing Shen, and David A. Ball. Saturation effects in fluorescence correlation spectroscopy. *Proceedings of SPIE, Multiphoton Microscopy in the Biomedical Sciences V*, 5700(March 2005):128–137, 2005. doi: 10.1117/12.591099.

[104] Goro Nishimura and Masataka Kinjo. Dead-time distortion in fluorescence correlation measurements. *Applied Optics*, 44(17):3458–3467, 2005. doi: 10.1364/AO.44.003458.

[105] Sina Jazani, Ioannis Sgouralis, Omer M. Shafraz, Marcia Levitus, Sanjeevi Sivasankar, and Steve Pressé. An alternative framework for fluorescence correlation spectroscopy. *Nature Communications*, 10:1–10, 2019. doi: 10.1038/s41467-019-11574-2.

[106] Morton B. Brown and Alan B. Forsythe. Robust tests for the equality of variances. *Journal of the American Statistical Association*, 69(346):364–367, 1974. doi: 10.1080/01621459.1974.10482955.

[107] Bernard L. Welch. The generalisation of student's problem when several different population variances are involved. *Biometrika*, 34(1-2):28–35, 1947. doi: 10.1093/biomet/34.1-2.28.

[108] Hima Nagamanasa Kandula, Ah Young Jee, and Steve Granick. Robustness of FCS (Fluorescence Correlation Spectroscopy) with Quenchers Present. *Journal of Physical Chemistry A*, 123(46):10184–10189, 2019. doi: 10.1021/acs.jpca.9b08273.

[109] Sayed Shahabuddin Hoseini and Martin G. Sauer. Molecular cloning using polymerase chain reaction, an educational guide for cellular engineering. *Journal of Biological Engineering*, 9(1):1–12, 2015. doi: 10.1186/1754-1611-9-2.

[110] Martina Doleshal, Amber A. Magotra, Bhavna Choudhury, Brian D. Cannon, Emmanuel Labourier, and Anna E. Szafranska. Evaluation and Validation of Total RNA Extraction Methods for MicroRNA Expression Analyses in Parafin-embedded Tissues. *Journal of Molecular Diagnostics*, 10(3):203–211, 2008. doi: 10.2353/jmoldx.2008.070153.

[111] Shan-rong Rong Shi, Richard J. Cote, Lin Wu, Cheng Liu, Ram Datar, Yan Shi, Dongxin Liu, Hyoeun Lim, and Clive R. Taylor. DNA extraction from archival formalin-fixed, paraffin-embedded tissue sections based on the antigen retrieval principle: Heating under the influence of pH. *Journal of Histochemistry and Cytochemistry*, 50(8):1005–1011, 2002. doi: 10.1177/002215540205000802.

[112] Changsoo Lee, Jaai Kim, Seung Gu Shin, and Seokhwan Hwang. Absolute and relative QPCR quantification of plasmid copy number in Escherichia coli. *Journal of Biotechnology*, 123:273–280, 2006. doi: 10.1016/j.jbiotec.2005.11.014.

[113] Thomas D. Schmittgen and Kenneth J. Livak. Analyzing real-time PCR data by the comparative CT method. *Nature Protocols*, 3(6):1101–1108, 2008. doi: 10.1038/nprot.2008.73.

[114] Illumina. An introduction to Next-Generation Sequencing Technology. Illumina Inc., San Diego, 2017. online: `https://www.illumina.com/content/dam/illumina-marketing/documents/products/illumina_sequencing_introduction.pdf`, visited on 2022-06-13.

[115] Jérôme D. Robin, Andrew T. Ludlow, Ryan LaRanger, Woodring E. Wright, and Jerry W. Shay. Comparison of DNA Quantification Methods for Next Generation Sequencing. *Scientific Reports*, 6(24067):1–10, 2016. doi: 10.1038/srep24067.

[116] Christian Hussing, Marie Louise Kampmann, Helle Smidt Mogensen, Claus Børsting, and Niels Morling. Quantification of massively parallel sequencing libraries - A comparative study of eight methods. *Scientific Reports*, 8(1):1–9, 2018. doi: 10.1038/s41598-018-19574-w.

[117] A. I. Dragan, J. R. Casas-Finet, E. S. Bishop, R. J. Strouse, M. A. Schenerman, and C. D. Geddes. Characterization of PicoGreen interaction with dsDNA and the origin of its fluorescence enhancement upon binding. *Biophysical Journal*, 99(9): 3010–3019, 2010. doi: 10.1016/j.bpj.2010.09.012.

[118] A. I. Dragan, R. Pavlovic, J. B. McGivney, J. R. Casas-Finet, E. S. Bishop, R. J. Strouse, M. A. Schenerman, and C. D. Geddes. SYBR Green I: Fluorescence properties and interaction with DNA. *Journal of Fluorescence*, 22(4):1189–1199, 2012. doi: 10.1007/s10895-012-1059-8.

[119] Wolfgang Eimer and R. Pecora. Rotational and translational diffusion of short rodlike molecules in solution: Oligonucleotides. *The Journal of Chemical Physics*, 94(3):2324–2329, 1991. doi: 10.1063/1.459904.

[120] Karen O'Hanlon Cohrt. How to calculate the number of molecules in any piece of DNA. Science Squared Ltd/Bitesize Bio, May 2021. online: `https://bitesizebio.com/20669/how-to-calculate-the-number-of-molecules-in-any-piece-of-dna/`, visited on 2022-06-13.

[121] Arlette Longin, Catherine Souchier, Martine Ffrench, and Paul-André Bryon. Comparison of anti-fading agents used in fluorescence microscopy: image analysis and laser confocal microscopy study. *Journal of Histochemistry and Cytochemistry*, 41 (12):1833–1840, 1992. doi: 10.1016/0248-4900(92)90310-W.

[122] R. J. Florijn, J. Slats, H. J. Tanke, and A. K. Raap. Analysis of antifading reagents for fluorescence microscopy. *Cytometry*, 19(2):177–182, 1995. doi: 10.1002/cyto.990190213.

[123] M. Ono, T. Murakami, A. Kudo, M. Isshiki, H. Sawada, and A. Segawa. Quantitative comparison of anti-fading mounting media for confocal laser scanning microscopy. *Journal of Histochemistry and Cytochemistry*, 49(3):305–311, 2001. doi: 10.1177/002215540104900304.

[124] Thorben Cordes, Andreas Maiser, Christian Steinhauer, Lothar Schermelleh, and Philip Tinnefeld. Mechanisms and advancement of antifading agents for fluorescence microscopy and single-molecule spectroscopy. *Physical Chemistry Chemical Physics*, 13(14):6699–6709, 2011. doi: 10.1039/c0cp01919d.

[125] Gergely L. Lukacs, Peter Haggie, Olivier Seksek, D. Lechardeur, Neal Freedman, and A. S. Verkman. Size-dependent DNA mobility in cytoplasm and nucleus. *Journal of Biological Chemistry*, 275(3):1625–1629, 2000. doi: 10.1074/jbc.275.3.1625.

[126] Artem V. Melnykov and Kathleen B. Hall. Revival of high order fluorescence correlation analysis: generalized theory and biochemical applications. *Journal of Physical Chemistry B*, 113(47):15629–15638, 2010. doi: 10.1021/jp906539k.Revival.

10 Appendix

10.1 Generalization of the FCS calculation to higher orders

The model of the fluorescence correlation spectroscopy (FCS) presented in section 2.3 can be extended to the general case of arbitrary higher orders. This concept of high order fluorescence fcorrelation spectroscopy (HOFCS) was developed in a series of publications by Palmer and Thompson [29, 30, 31]. The HOFCS was primarily developed for the analysis of aggregation states of macromolecules. However, it could be shown that the HOFCS is suitable for the examination of non-equilibrium states in biochemistry and by means of simulations that the HOFCS provides a better resolution for macromolecules at different brightness levels than the classical FCS [126]. The principle formular for HOFCS is given by [29, p. 257-258]:

$$G_{m,n}(\tau) = \frac{\langle \delta I^m(t)\delta I^n(t+\tau)\rangle_t - \langle \delta I^m(t)\rangle_t \langle \delta I^n(t)\rangle_t}{\langle I(t)\rangle_t^{m+n}}. \tag{10.1}$$

The indices m and n account for the order of the HOFCS. For an efficient calculation of the HOFCS, we can, as for the efficient calculation of the FCS in section 3.3.1, employ the Wiener-Khinchin theorem. First, we identify $\langle \delta I^m(t)\delta I^n(t+\tau)\rangle_t$ as the actual correlation. In this case, it can be treated as a cross-correlation $r_{xy}(\tau)$ as $x^m \neq x^n$ for $m \neq n$. The remaining terms are scalar constants. Thus, we get:

$$G_{m,n}(\tau) = \frac{r_{xy}(\tau) - \langle \delta I^m(t)\rangle_t \langle \delta I^n(t)\rangle_t}{\langle I(t)\rangle_t^{m+n}} \tag{10.2}$$

Analogous to the calculation of the autocorrelation $r_{xx}(\tau)$, we can use the so-called *cross spectral density* (CSD) for the calculation of the cross-correlation $r_{xy}(\tau)$. Starting with equation 3.10, it can be reshaped as follows

$$S_{xx}(\omega) = |\hat{x}(\omega)|^2 = \hat{x}^*(\omega)\hat{x}(\omega) \tag{10.3}$$

The asterisk * denotes the complex conjugate of x (it is $x = a + bi$ and for the complex conjugate $x^* = a - bi$) and is important for processing Fourier transformed time series as used in this case . The PSD can be regarded as a special case of the CSD, which is given by

$$S_{xy}(\omega) = \hat{x}^*(\omega)\hat{y}(\omega) = \mathcal{F}^*\{x(t)\}\mathcal{F}\{y(t)\}. \tag{10.4}$$

Now, the Wiener-Khinchin theorem can be applied, and we get for the correlation term

$$r_{xy}(\tau) = \frac{1}{2\pi}\int_{-\infty}^{\infty} S_{xy} e^{i\omega\tau}\,\mathrm{d}\omega = \mathcal{F}^{-1}\big\{\mathcal{F}^*\{x(t)\}\mathcal{F}\{y(t)\}\big\}. \tag{10.5}$$

Finally, for our HOFCS case, we simply put $x = x^m$ and $y = x^n$ and we get our final expression.

$$r_{x^m x^n} = \mathcal{F}^{-1}\big\{\mathcal{F}^*\{x^m(t)\}\mathcal{F}\{x^n(t)\}\big\} \tag{10.6}$$

And for our application on fluorescence traces, we set $x(t) = \delta I(t)$ as the fluorescence intensity fluctuations.

$$r_{x^m x^n} = \mathcal{F}^{-1}\big\{\mathcal{F}^*\{\delta I^m(t)\}\mathcal{F}\{\delta I^n(t)\}\big\} \tag{10.7}$$

To check the plausibility of the expression for the HOFCS, consider the case for the first order. By setting $m = n = 1$, equation 10.1 reduces as follows:

$$G_{1,1}(\tau) = \frac{r_{x^1x^1}(\tau) - \overbrace{\langle \delta I^1(t)\rangle_t \langle \delta I^1(t)\rangle_t}^{=0}}{\langle I(t)\rangle_t^{1+1}} \tag{10.8}$$

$$= \frac{r_{xx}(\tau)}{\langle I(t)\rangle_t^2} \tag{10.9}$$

$$= \frac{\mathcal{F}^{-1}\big\{\mathcal{F}^*\{\delta I(\tau)\}\mathcal{F}\{\delta I(\tau)\}\big\}}{\langle I(t)\rangle_t^2} \tag{10.10}$$

$$= \frac{\mathcal{F}^{-1}\big\{\mathcal{F}^*\{I(\tau)\}\mathcal{F}\{I(\tau)\}\big\}}{\langle I(t)\rangle_t^2} - 1 \tag{10.11}$$

$$= \frac{\mathcal{F}^{-1}\big\{|\mathcal{F}\{x(t)\}|^2\big\}}{\langle I(t)\rangle_t^2} - 1 \tag{10.12}$$

The last expression corresponds exactly to equation 3.14.

10.2 Additional information to the mSMR model

When calculating the diffusion term of the mSMR model using a Gaussian profile, three terms emerge in the calculation whose equivalence is not directly obvious.

$$\begin{aligned}\Gamma_{\text{diff,3DG}}(T) = \frac{2r\tau_\text{D}}{T^2\sqrt{r^2-1}}\Bigg(&2r\sqrt{r^2-1}\tau_\text{D} - 2\sqrt{(r^2-1)\tau_\text{D}(T+r^2\tau_\text{D})} \\ &+ \tau_\text{D}\ln\left[\frac{(r+\sqrt{r^2-1})(\sqrt{\frac{T+r^2\tau_\text{D}}{(r^2-1)\tau_\text{D}}}-1)}{(r-\sqrt{r^2-1})(\sqrt{\frac{T+r^2\tau_\text{D}}{(r^2-1)\tau_\text{D}}}+1)}\right] \\ &- T\ln\left[\frac{(r-\sqrt{r^2-1})(\sqrt{\frac{T+r^2\tau_\text{D}}{(r^2-1)\tau_\text{D}}}+1)}{(r+\sqrt{r^2-1})(\sqrt{\frac{T+r^2\tau_\text{D}}{(r^2-1)\tau_\text{D}}}-1)}\right]\Bigg) \qquad (10.13)\end{aligned}$$

$$\begin{aligned}= \frac{4r\tau_\text{D}}{T^2\sqrt{r^2-1}}\Bigg(&r\sqrt{r^2-1}\tau_\text{D} - \sqrt{(r^2-1)\tau_\text{D}(T+r^2\tau_\text{D})} \\ &+ (T+\tau_\text{D})\left[\operatorname{artanh}\left(\frac{r}{\sqrt{r^2-1}}\right) - \operatorname{artanh}\left(\frac{\sqrt{T+r^2\tau_\text{D}}}{\sqrt{(r^2-1)\tau_\text{D}}}\right)\right]\Bigg) \qquad (10.14)\end{aligned}$$

$$\begin{aligned}= \frac{4}{\alpha^2\beta}\Bigg(&1-\sqrt{1+\alpha\,\beta} \\ &+ \frac{\beta(1+\alpha)}{\sqrt{1-\beta}}\operatorname{artanh}\left[\sqrt{1-\beta}\frac{(\sqrt{1+\alpha\,\beta}-1)}{(\beta+\sqrt{1+\alpha\,\beta}-1)}\right]\Bigg) \qquad (10.15)\end{aligned}$$

with $\alpha = T/\tau_\text{D}$ and $\beta = r^{-2}$. It is easiest to compare mathematical terms graphically (see figure 10.1). The data agree within floating number precision.

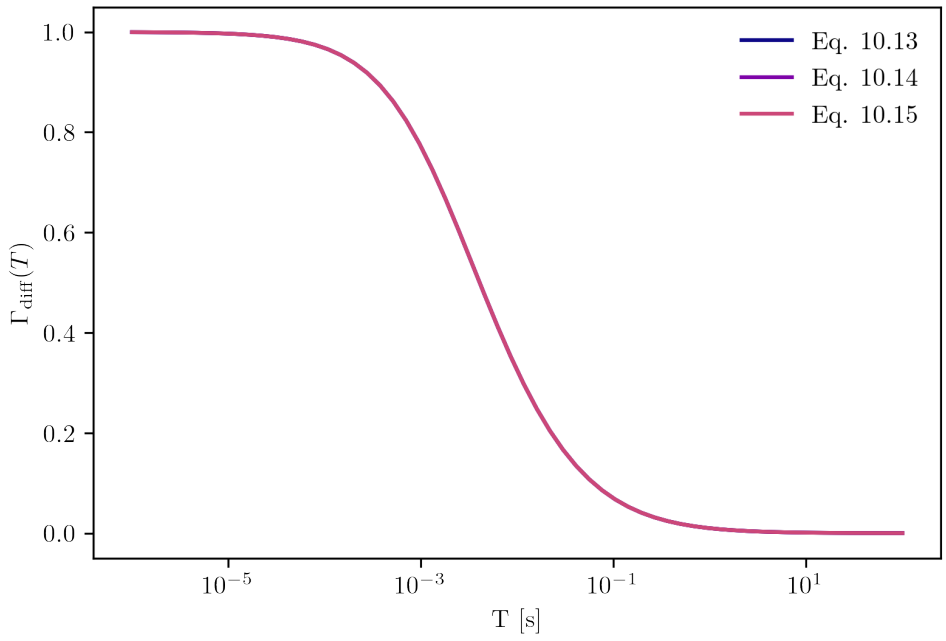

Figure 10.1: Visual comparison of equation 10.13, 10.14 and 10.15 in the mSMR model.

10.3 Supplementary information on afterpulsing in Monte Carlo simulations

To verify whether afterpulsing effects also occur in FCS analyses of simulated fluorescence traces, the simulation run from section 4.4.1 was repeated with a higher temporal resolution of 1×10^{-7} s. Figure 10.2 shows the results of this run.

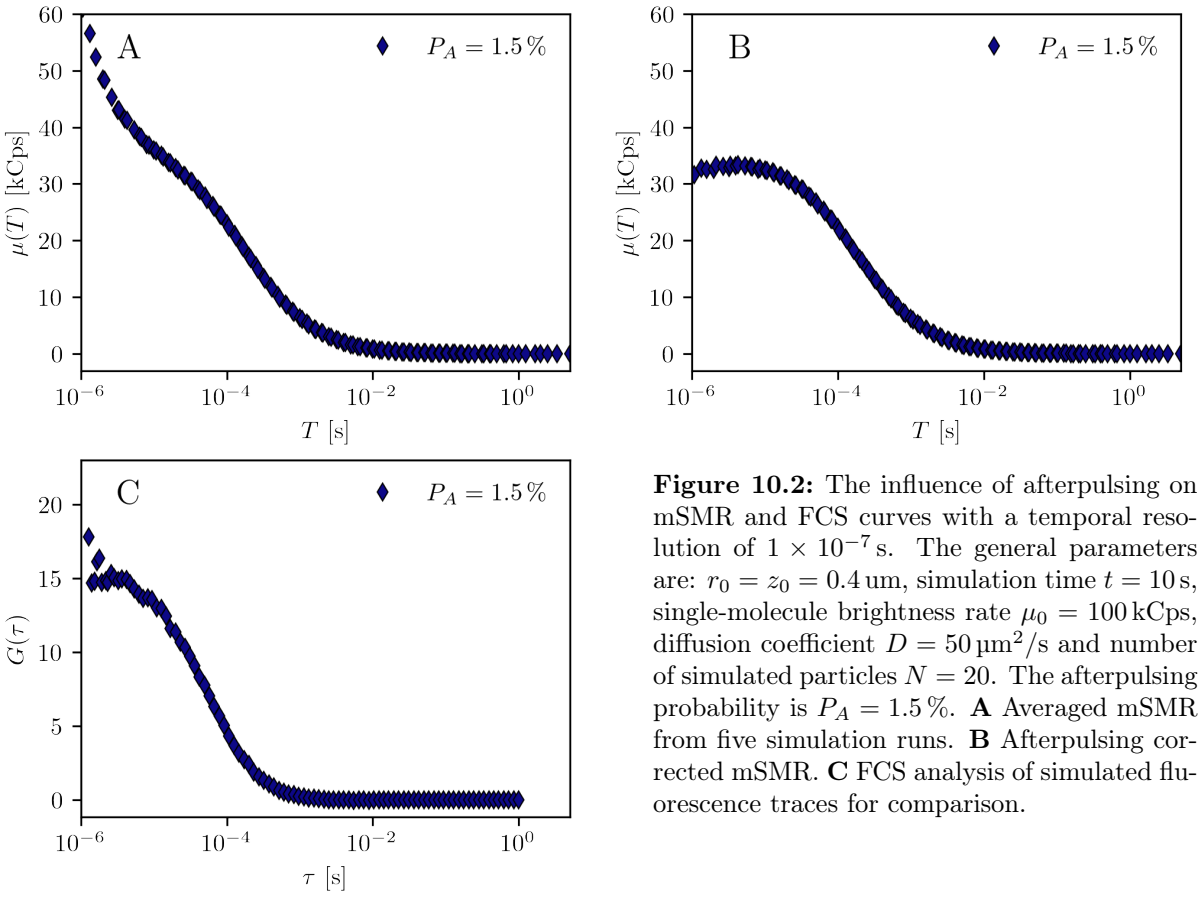

Figure 10.2: The influence of afterpulsing on mSMR and FCS curves with a temporal resolution of 1×10^{-7} s. The general parameters are: $r_0 = z_0 = 0.4$ um, simulation time $t = 10$ s, single-molecule brightness rate $\mu_0 = 100$ kCps, diffusion coefficient $D = 50\,\mu m^2/s$ and number of simulated particles $N = 20$. The afterpulsing probability is $P_A = 1.5\,\%$. **A** Averaged mSMR from five simulation runs. **B** Afterpulsing corrected mSMR. **C** FCS analysis of simulated fluorescence traces for comparison.

Subplot A shows the results of the mSMR analysis. The influence of afterpulsing at short time scales is evident. The effect is compensated by the correction of the cumulants, so that in subplot B no afterpulsing appears. In the FCS evaluations in subplot C, afterpulsing effects are noticeable at short time intervals for the given time resolution, which cannot be corrected.

10.4 Statistical measures from the comparison of FCS and mSMR

Table 10.1: Measures of the statistical comparison of FCS and mSMR, part 1. The statistical significance in all cases is $\alpha = 0.05$

$10\,\mu W$

Parameter	Test	P_{value}	Significance	Conclusion
$\langle N \rangle$ (FCS)	Kolmogorow-Smirnow test	0.891	No	Normally distributed
τ_D (FCS)	Kolmogorow-Smirnow test	0.882	No	Normally distributed
F_{trip} (FCS)	Kolmogorow-Smirnow test	0.941	No	Normally distributed
τ_{trip} (FCS)	Kolmogorow-Smirnow test	0.689	No	Normally distributed
$\langle N \rangle$ (mSMR)	Kolmogorow-Smirnow test	0.948	No	Normally distributed
τ_D (mSMR)	Kolmogorow-Smirnow test	0.999	No	Normally distributed
F_{trip} (mSMR)	Kolmogorow-Smirnow test	0.689	No	Normally distributed
τ_{trip} (mSMR)	Kolmogorow-Smirnow test	0.963	No	Normally distributed
$\langle N \rangle$	Brown-Forsythe test	0.766	No	Variance the same
τ_D	Brown-Forsythe test	0.890	No	Variance the same
F_{trip}	Brown-Forsythe test	0.005	Yes	Variance differs
τ_{trip}	Brown-Forsythe test	0.432	No	Variance the same
$\langle N \rangle$	Welch's t-test	0.137	No	Mean the same
τ_D	Welch's t-test	0.271	No	Mean the same
F_{trip}	Welch's t-test	0.000	Yes	Mean differs
τ_{trip}	Welch's t-test	0.000	Yes	Mean differs

$30\,\mu W$

Parameter	Test	P_{value}	Significance	Conclusion
$\langle N \rangle$ (FCS)	Kolmogorow-Smirnow test	0.223	No	Normally distributed
τ_D (FCS)	Kolmogorow-Smirnow test	0.820	No	Normally distributed
F_{trip} (FCS)	Kolmogorow-Smirnow test	0.793	No	Normally distributed
τ_{trip} (FCS)	Kolmogorow-Smirnow test	0.680	No	Normally distributed
$\langle N \rangle$ (mSMR)	Kolmogorow-Smirnow test	0.397	No	Normally distributed
τ_D (mSMR)	Kolmogorow-Smirnow test	0.931	No	Normally distributed
F_{trip} (mSMR)	Kolmogorow-Smirnow test	0.772	No	Normally distributed
τ_{trip} (mSMR)	Kolmogorow-Smirnow test	0.890	No	Normally distributed
$\langle N \rangle$	Brown-Forsythe test	0.980	No	Variance the same
τ_D	Brown-Forsythe test	0.708	No	Variance the same
F_{trip}	Brown-Forsythe test	0.003	Yes	Variance differs
τ_{trip}	Brown-Forsythe test	0.424	No	Variance the same
$\langle N \rangle$	Welch's t-test	0.987	No	Mean the same
τ_D	Welch's t-test	0.707	No	Mean the same
F_{trip}	Welch's t-test	0.000	Yes	Mean differs
τ_{trip}	Welch's t-test	0.059	No	Mean the same

Table 10.2: Measures of the statistical comparison of FCS and mSMR, part 2. The statistical significance in all cases is $\alpha = 0.05$

50 µW

Parameter	Test	P_{value}	Significance	Conclusion
$\langle N \rangle$ (FCS)	Kolmogorow-Smirnow test	0.569	No	Normally distributed
τ_{D} (FCS)	Kolmogorow-Smirnow test	0.610	No	Normally distributed
F_{trip} (FCS)	Kolmogorow-Smirnow test	0.857	No	Normally distributed
τ_{trip} (FCS)	Kolmogorow-Smirnow test	0.740	No	Normally distributed
$\langle N \rangle$ (mSMR)	Kolmogorow-Smirnow test	0.203	No	Normally distributed
τ_{D} (mSMR)	Kolmogorow-Smirnow test	0.928	No	Normally distributed
F_{trip} (mSMR)	Kolmogorow-Smirnow test	0.977	No	Normally distributed
τ_{trip} (mSMR)	Kolmogorow-Smirnow test	0.792	No	Normally distributed
$\langle N \rangle$	Brown-Forsythe test	0.759	No	Variance the same
τ_{D}	Brown-Forsythe test	0.863	No	Variance the same
F_{trip}	Brown-Forsythe test	0.000	Yes	Variance differs
τ_{trip}	Brown-Forsythe test	0.009	Yes	Variance differs
$\langle N \rangle$	Welch's t-test	0.910	No	Mean the same
τ_D	Welch's t-test	0.791	No	Mean the same
F_{trip}	Welch's t-test	0.000	Yes	Mean differs
τ_{trip}	Welch's t-test	0.031	Yes	Mean differs

70 µW

Parameter	Test	P_{value}	Significance	Conclusion
$\langle N \rangle$ (FCS)	Kolmogorow-Smirnow test	0.449	No	Normally distributed
τ_{D} (FCS)	Kolmogorow-Smirnow test	0.326	No	Normally distributed
F_{trip} (FCS)	Kolmogorow-Smirnow test	0.478	No	Normally distributed
τ_{trip} (FCS)	Kolmogorow-Smirnow test	0.746	No	Normally distributed
$\langle N \rangle$ (mSMR)	Kolmogorow-Smirnow test	0.222	No	Normally distributed
τ_{D} (mSMR)	Kolmogorow-Smirnow test	0.949	No	Normally distributed
F_{trip} (mSMR)	Kolmogorow-Smirnow test	0.817	No	Normally distributed
τ_{trip} (mSMR)	Kolmogorow-Smirnow test	0.775	No	Normally distributed
$\langle N \rangle$	Brown-Forsythe test	0.846	No	Variance the same
τ_{D}	Brown-Forsythe test	0.777	No	Variance the same
F_{trip}	Brown-Forsythe test	0.015	Yes	Variance differs
τ_{trip}	Brown-Forsythe test	0.118	No	Variance the same
$\langle N \rangle$	Welch's t-test	0.673	No	Mean the same
τ_{D}	Welch's t-test	0.306	No	Mean the same
F_{trip}	Welch's t-test	0.000	Yes	Mean differs
τ_{trip}	Welch's t-test	0.000	Yes	Mean differs

Acknowledgement

A dissertation does not come into being in a vacuum, but is based on preceding research work and constant exchange. Many people therefore have their share in the successful completion of such work. I will try to express my sincere thanks to the most important people and apologize in advance to all those whom I have not highlighted separately. First and foremost, my special thanks go to Dr. Benjamin Greiner for his manifold support. This includes discussing the results, cross-checking the mathematical models, and his constant motivation. In addition, Benny programmed significant parts of the Monte Carlo simulation that was used for this thesis. Furthermore, I would like to thank Steffen Krüger. Without him, the confocal plate reader would not exist in its current form. Steffen made the construction drawings and led the assembly of the system. He also held countless meetings and discussions with suppliers until the necessary tolerances and specifications were finally met. Christian Müller assisted the process with the ordering of the device components and the preparation of quotations. The programming of the hardware drivers was carried out by Moritz Balg and Alexander Schuster. Errors in the circuit board design almost brought the two to the brink of despair. Great that you guys stuck it out! The orchestration of the hardware components in meaningful program sequences was programmed by Michael Fuchs. He also provided a graphical user interface to operate the system comfortably. We spent countless hours together in the lab and debugged the system until it ran stable. Thanks again for that! I would also like to emphasize Kristian Berwanger. Kris not only helped a lot with the application for project funding, but also always kept an eye on exploitation options and thus emphasized the relevance of the research topic. He was also a reliable companion at conferences. Furthermore, my thanks go to Prof. Dr. Harald Mathis for his support of the work as head of the BioMOS group. Especially in the second half of the thesis I received important feedback, which allowed me to focus the topic of my thesis. In addition, I would like to express my gratitude to all employees of Fraunhofer FIT who have accompanied me over the past years of my journey. Great acknowledgement goes to my first thesis advisor Prof. Dr. Ulrich Schwaneberg head of the Department of Biotechnology at RWTH Aachen University and my second thesis advisor Prof. Dr. Thomas Berlage head of the Department of Digital Health at Fraunhofer FIT. Finally and perhaps most importantly, I want to point out the invaluable support from my wife and my family that allowed me to pursue my dreams and tackle this challenge.